2019

BIOMASS-DERIVED ACTIVATED CARBONS FOR ELECTRICAL DOUBLE LAYER SUPERCAPACITORS: PERFORMANCE AND STRESS EFFECT

Wenxin Cao

University of Kentucky, elaine_0725@uky.edu

Author ORCID Identifier:

https://orcid.org/0000-0003-0953-8686

Digital Object Identifier: https://doi.org/10.13023/etd.2019.045

STUDENT AGREEMENT:

I represent that my thesis or dissertation and abstract are my original work. Proper attribution has been given to all outside sources. I understand that I am solely responsible for obtaining any needed copyright permissions. I have obtained needed written permission statement(s) from the owner(s) of each third-party copyrighted matter to be included in my work, allowing electronic distribution (if such use is not permitted by the fair use doctrine) which will be submitted to UKnowledge as Additional File.

I hereby grant to The University of Kentucky and its agents the irrevocable, non-exclusive, and royalty-free license to archive and make accessible my work in whole or in part in all forms of media, now or hereafter known. I agree that the document mentioned above may be made available immediately for worldwide access unless an embargo applies.

I retain all other ownership rights to the copyright of my work. I also retain the right to use in future works (such as articles or books) all or part of my work. I understand that I am free to register the copyright to my work.

REVIEW, APPROVAL AND ACCEPTANCE

The document mentioned above has been reviewed and accepted by the student's advisor, on behalf of the advisory committee, and by the Director of Graduate Studies (DGS), on behalf of the program; we verify that this is the final, approved version of the student's thesis including all changes required by the advisory committee. The undersigned agree to abide by the statements above.

Wenxin Cao, Student

Dr. Fuqian Yang, Major Professor

Dr. Matthew Beck, Director of Graduate Studies

BIOMASS-DERIVED ACTIVATED CARBONS FOR
ELECTRICAL DOUBLE LAYER SUPERCAPACITORS:
PERFORMANCE AND STRESS EFFECT

_____

DISSERTATION
_____

A dissertation submitted in partial fulfillment of the
requirements for the degree of Doctor of Philosophy in the
College of Engineering at the University of Kentucky

By
Wenxin Cao
Lexington, Kentucky
Director: Dr. Fuqian Yang, Professor of Materials Science and Engineering
Lexington, Kentucky
2018

ABSTRACT OF DISSERTATION

BIOMASS-DERIVED ACTIVATED CARBONS FOR
ELECTRICAL DOUBLE LAYER SUPERCAPACITORS:
PERFORMANCE AND STRESS EFFECT

The vigorous development of human civilization has significantly increased the energy consumption in recent years. There is a great need to use renewable energy sources to substitute the depleting traditional fossil fuels, such as crude oil, natural gas and coal. The development of low-cost and high-performance energy storage devices (ESDs) and systems have drawn great attention due to their feasibility as backup power supply and their applications in portable electronics and electric vehicles. Supercapacitors are among the most important ESDs because of their long charging-discharging cycle life, high power capability and a large operating temperature range. In this thesis, high-performance activated carbons (ACs)-based SCs have been synthesized from two biomass materials in both "bottom-up" and "top-down" patterns, including high fructose corn syrup and soybean residues, which are economic and environmental friendly.

Firstly, a hydrothermal carbonization (HTC) - physical activation method is presented to synthesize activated carbons from high fructose corn syrup (HFCS). The effect of the activation time on the geometrical and porous characteristics of the ACs is investigated. The electrochemical performance of the supercapacitor cells made from AC treated at 850ºC for 4 hours are found as the best with a specific capacitance of 168 F/g at 0.2 A/g in 6 M KOH aqueous system. Secondly, a two-step HTC process followed by a physical activation to prepare activated carbons from soybean residue is presented. The effect of activation temperature on geometrical and porous characteristics of the ACs is studied. The ACs activated at 850ºC are found partly crystallized and exhibit a specific capacitance of 227 F/g at 2 mV/s.

To understand the effect of mechanical deformation of the electrode materials on the electrochemical performance of electrical double-layer supercapacitors, a series of compression tests of HFCS-based ACs are further conducted in both dry and wet

conditions. The nominal stiffness of the compressed ACs is calculated from the unloading curves. For both dry and wet disks the stiffness get increased with increased compression load, where the wet ones get higher stiffness than that of the dry ones. A simple model of porous materials is used to explain the increase in the stiffness of a compressed disk with the increase of pressure.

Lastly, the effect of mechanical deformation on the electrochemical impedance of HFCS-based ACs is studied. When increasing the mechanical pressure from 4 to 81.5 KPa, the system resistance shows a relatively stable trend around 1 ohm, while the charge transfer resistance shows a dramatic dependence on mechanical pressure decreasing from 420 ohms to 1.5 ohms.

Wenxin Cao

(Name of Student)

01/07/2019

Date

BIOMASS-DERIVED ACTIVATED CARBONS FOR
ELECTRICAL DOUBLE LAYER SUPERCAPACITORS:
PERFORMANCE AND STRESS EFFECT

By
Wenxin Cao

Fuqian Yang	
Director of Dissertation	

Matthew Beck	
Director of Graduate Studies	

11/12/2018	
Date	

ACKNOWLEDGMENTS

I would like to thank Dr. Fuqian Yang for offering me this valued opportunity to study in UK, join in his research projects and pursue my PhD study. His help during the past three years enlightens me and leads me to the completion of my PhD study. I also want to thank my committee members, Dr. Rankin, Dr. Chen, Dr. Liao and Dr. Yin, for their time and energy spent on reviewing my dissertation and their priceless suggestions. Additionally, I would like to acknowledge all members in Dr. Yang's research group, the faculties and staffs in the department of Chemical and Materials Engineering. It is their support that makes my completion of this work possible.

Last but not least, I would like to express my gratitude towards my family and friends who encouraged me along the way.

TABLE OF CONTENTS

vi

LIST OF TABLES

LIST OF FIGURES

LIST OF ABBREVIATIONS AND SYMBOLS

ESD(s) ....Energy Storage Device(s)

LIBs ....Lithium-ion Batteries

SC(s) ....Supercapacitor(s)

EDLC(s) ....Electric Double-layer Capacitor(s)

C_{dl} ....The Capacitance of the EDL

AC(s) ....Activated Carbon(s)

CNT(s) ....Carbon Nanotube(s)

TPC(s)..Templated Porous Carbon(s)

ILs...Ionic Liquids

CNP ....Carbon Nanoparticle

PANI ....Polyaniline

SEM ....Scanning Electron Microscope

TEM   ....Transmission   Electron
Microscopy

CV ....Cyclic Voltammetry

CCD ....Cyclic Charge-Discharge

EIS...Electrochemical   Impedance
Spectroscopy

PPy ....Polypyrrole

PVA...Poly (vinyl alcohol)

XRD ....X-ray Diffractometer

ESR ....Equivalent Series Resistance (Ω)

KOH...Potassium Hydroxide

K_2O..Potassium Oxide

CO_2..Carbon Dioxide

$ZnCl_2$..Zinc Chloride

H_2SO_4 ....Sulfuric Acid

H_3PO_4 ....Phosphoric Acid

Hz ....Hertz

C_s ....Specific Capacitance (F/g)

°C...Celsius Degree

CHAPTER 1.   INTRODUCTION

1.1   Background

The history of human development has always been accompanied with the revolution of the energy use. The history of human energy utilization has roughly gone through three periods: firewood, coal and oil. By using firewood, human began to use heat energy. By using livestock, watermill and wind mills, human learnt to take advantage of new energy sources to provide power for their development. With the discovery of coal and the combination of the development of machinery manufacturing, the first industrial revolution was born in the 18th century. As the main source of the steam engine, coal provides orders of magnitude of energy larger than that provided by previous energy sources, a new era of using fossil fuels for power was opened up. With the development of petroleum, internal combustion engine and electricity, the Second Industrial Revolution was energized and changed the human energy structure again by bringing oil onto the main stage. The high efficient and light internal combustion engine makes the automobile and aircraft possible while the easily transportation of electricity provides a worldwide power energy for residences, manufacturing industries and electronic devices.

With the continuous development of human civilization, society's demand for energy has increased dramatically. Energy consumption on the planet is increasing at an alarming rate, and the total energy consumption in the 20th century is almost half of that of the whole last 19 centuries. Fossil fuels, as the ideal energy sources for centuries, provided 81.46% of the total world primary energy supply in 2015[1], and will remain its

dominance in the near future. However, fossil fuels are non-renewable, and the over-exploiting has caused drastic reduction of their reserves. It is predicted that crude oil, natural gas and coal would be depleted in 35 years, 37 years and 107 years, respectively[2]. Moreover, the use of fossil fuels has caused disastrous environmental problems like acid rain and global warming. Therefore, an energy transition of rational utilization and development of sustainable energy has become the most important issue of the earth[3].

Renewable energy sources like wind, solar, biomass and hydropower have been increasing their share in energy supply, but still accounted for a limited share[1]due to their limited conversion rate, low energy output, intermittency and relatively high cost. A backup power supply system is essential to maintain the reliability and stability of the output provided by renewable energy sources. Energy storage systems and devices can store power at high output level of the renewable energies and supply power at the low output level, and also can provide off-grid energy supply for poor and remote areas. The smart grid systems built for the utilization of renewable energy that consist of power generators, automatic power control management module and energy storage systems and devices, are rapidly developed as the new generation of renewable power systems[4]. With the fast development of portable electronics and electric cars, energy storage devices with high energy and power density will play a core role in the future integration of renewable energy sources into the existing power system. In this chapter, the development of energy storage devices like supercapacitors for the application of renewable energy sources is discussed.

1.2 Energy storage devices

Energy storage devices (ESDs) of both high energy density and power density has always been the core determinant of better using the renewable energy sources and integrating them into the existing energy system for the development of modern society. The development of high-performance hybrid electric vehicles, pure electric vehicles, laptops and smartphones are all dependent on the innovation of low-cost and high capacity ESDs.

Energy, the ability to perform work, and Power, the rate at which the energy is produced, are two metrics used to compare different kinds of ESDs. For characterizing the amount of energy stored per unit mass/volume/area, the specific gravimetric/volumetric/areal energy can be obtained and is used to describe the energy density. In this dissertation, specific energy and specific power are defined as the energy density and power density per unit mass, respectively. A simplified "Ragone plot" shown in Figure 1.1[5]illustrates the energy and power densities of a variety of common used energy storage devices. Supercapacitors (SCs)lie in the gap between traditional capacitors and batteries, which have higher specific energy compared with traditional capacitors, and higher specific power compared with batteries. Lithium-ion batteries (LIBs) are popular for their high energy densies by converting chemical energy into electricity, but the power is also limited by the kinetics of chemical reaction. SCs possess several advantages over LIBs, including long charging-discharging cycles, high power capability, and a large operating temperature range[6]. However, the energy density of supercapacitors is much lower than that of LIBs. Thus, improving the energy density of supercapacitors without sacrificing the high power density is desired.

3
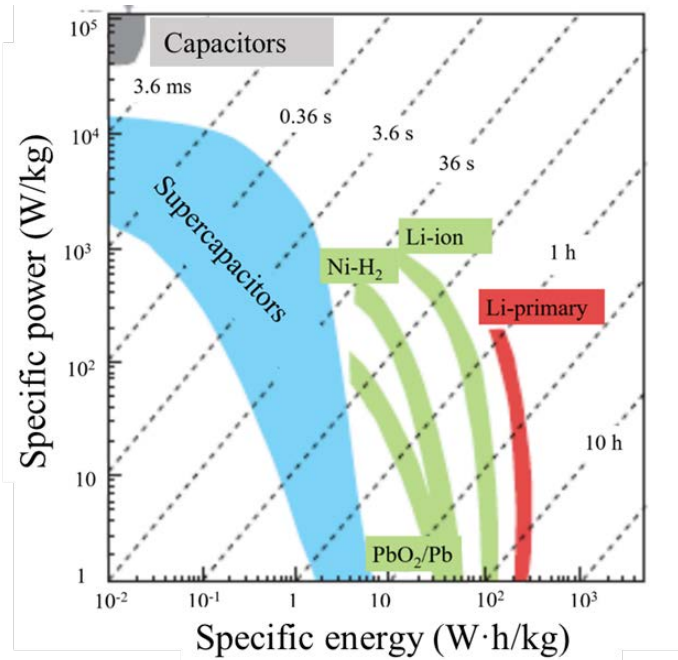
FIGURE 1.1 RAGONE PLOT SHOWING SPECIFIC POWER VERSE SPECIFIC ENERGY FOR VARIOUS ELECTRICAL ENERGY STORAGE DEVICES [5]

1.3   Supercapacitors

Supercapacitors can be classified into three types according to the energy storage mechanisms: electrochemical double layer capacitors (EDLCs), pseudo-capacitors, and hybrid capacitors (a combination of EDLCs and pseudo-capacitors). Although the mechanisms among these three are different, they share similar structure. SCs consists of two electrodes soaked in electrolyte, electric double layers are formed at the interfaces between the electrolyte and the electrodes to store energy, which is different from conventional capacitors that use dielectric layers to fill; current collectors, which usually are highly conductive materials, are directly connected to the external circuit; a separator, which is a thin, porous, non-conductive and ion-permeable film, is placed between the two electrodes to prevent short circuit.

4

The concept of the EDL was first introduced by von Helmholtz[7]in the 19th century, unlike conventional capacitors in which the capacity of energy storage is limited by the charge-storage area and the distance. EDL-based capacitors possess large surface area and the separation distance of charges at the nanoscale, they can store much more energy. There are no chemical redox reactions involved in the charge storage. The capacitance can be approximatively calculated as:

$$C_H = \frac{\varepsilon}{d_H} \tag{1.1}$$

where ε is the permittivity of the electrolyte, and d_H is the thickness of the Helmholtz layer.

Stern[8]modified the EDL model, as shown in Figure 1.2, which consists of two regions for the distribution of ions — an inner region as the compact layer, where ions (always hydrated) are adsorbed to the electrode, and a diffuse layer, in which electrolyte ions continuously distribute due to thermal motion in electrolyte. The diffusion capacitance can be expressed as:

$$C_{diff} = \frac{\varepsilon}{\lambda_D} \tag{1.2}$$

where λ_D is a temperature, ionic concentration-dependent constant, also is called the thickness of the diffuse electrical double layer.

The capacitance of EDL (C_{dl}) can be calculated as the capacitances of the two regions in series, which can be expressed as:

$$\frac{1}{C_{dl}} = \frac{1}{C_s} + \frac{1}{C_{diff}} \tag{1.3}$$

where C_s is the Stern layer capacitance.

(a)   (b)
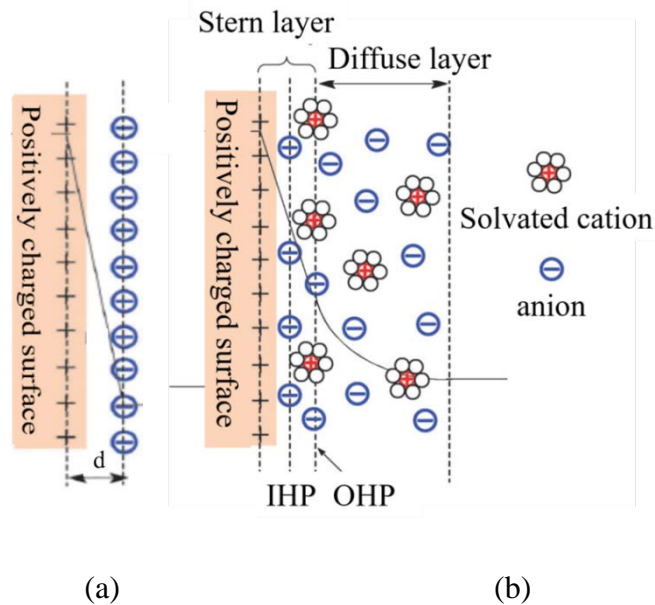
FIGURE 1.2 SCHEMATIC OF EDL MODELS AT A POSITIVELY CHARGED SURFACE: (A) HELMHOLTZ MODEL, AND (B) STERN MODEL, SHOWING THE INNER HELMHOLTZ PLANE (IHP) (COMPACT LAYER OR STERN LAYER) AND OUTER HELMHOLTZ PLANE (OHP) (DIFFUSION LAYER)[9]

1.4   EDLCs

EDLCs, whose energy storage is determined by the accumulation of electric charge at the electrode/electrolyte interface, have relatively long cycle lives, and their performance is dependent on several factors including electrical field intensity, electrolyte ions and solvent, and chemical affinity between adsorbed ions and electrode surface. For EDLCs, the two electrodes are always made with the same materials, which are also called symmetrical supercapacitors. Note that there are no terms of "anode" and "cathode" used for EDLCs since there are no redox reactions.

1.4.1 Carbon-based materials

Electrode is the most important component of SCs. The electrode of EDLCs is usually made from porous materials with high specific surface area (SSA), which makes it more complex than solid surface due to the irregular paths for mass transport, the pore-space constraint, the Ohmic resistance associated with electrolyte, and the wetting behavior of electrolyte on the pore surface. Carbon-based materials are the widely-used electrode materials for EDLCs, including activated carbons (ACs), carbon aerogels, carbon fibers, carbon nanotubes (CNTs), templated porous carbons (TPCs) and graphene. The pore population usually includes micropores (< 2 nm), mesopores (2-50 nm) and macropores (> 50 nm).Both pore sizes and the distribution of pore sizes play important roles in determining electrochemical behavior of the EDL-based capacitors made from porous materials. There are several modified models for the EDLCs from porous materials. The traditional porous carbon-based EDLC model is based on that submicropores are inaccessible to large solvated ions, and do not contribute to capacitance[10]. However, a significant contributions of micropores to the overall capacitance has also been reported[11],suggesting the presence of partial de-solvation of hydrated ions (Figure 1.3). It has been observed [5]that an maximum capacitance is contributed by pore sizes less than 1 nm, which is close to the ion size. The observation of the capacitance contribution from pores with sizes smaller than the solvated ion size leads to the development of several models taking pore curvature into consideration. One is electric double-cylinder capacitor (EDCC) model for mesoporous carbon electrodes, and the other is electric wire-in-cylinder capacitor (EWCC) model for microporous carbon electrodes[12]. The roles of micropores/mesopores/macropores in charge storage

still remain elusive, however, the wide distribution of the pore sizes is always detrimental for the energy density of SCs.
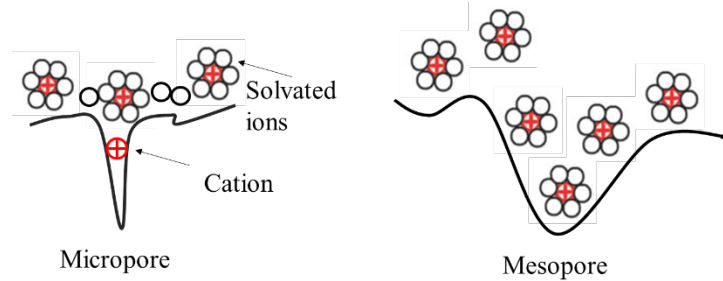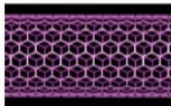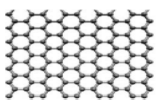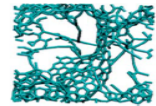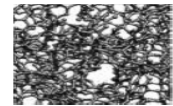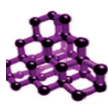
FIGURE 1.3 SCHEMATIC OF ADSORPTION OF SOLVATED IONS TO DIFFERENT PORE SIZES [11]

TABLE 1.1 CHARACTERISTIC OF CARBON STRUCTURES USED IN EDLCS [5]

Material	Carbon onions	Carbon nanotubes	Graphene	Activated carbon(ACs)	Carbide derived carbon	Templated carbon
Dimensionality	0 D	1 D	2 D	3 D	3 D	3 D
Conductivity	High	High	High	Structure dependent	Moderate	Low
Volumetric capacitance	Low	Low	Moderate	High	High	Low
Cost	High	High	Moderate	Low	Moderate	High
Structure						

The advantages of using carbon materials of various micro textures in EDLCs include high SSA, good electrical conductivity, interconnected pore structure and facile adjustable pore size. Among carbon materials of various micro textures, 3D carbon-based nanostructures such as AC-based architectures, CNT-based structures, graphene-based nanostructures, and hierarchical porous carbon-based networks likely possess high capacitive capacities due to interconnects of 3D networks. The skeleton of the porous

structures provides the path for electric conduction and better integrity. The characteristics of several carbon structures are listed in Table 1.1[5].

1.4.1.1 Activated carbons (ACs)

ACs with large SSA (~3000 m^2/g) and highly porous structure have potential applications of EDLCs. There are two activation categories of preparing ACs. One is chemical activation, using chemical agents such as potassium hydroxide (KOH) [13]and sodium hydroxide, acid and zinc chloride. The other is physical activation[14], using gaseous (oxidizing gasifying) agent such as carbon dioxide (CO_2) and steam activation (H_2O). Chemical activation as one of the methods to activate carbon has been used and studied in the past decades. Among various chemical reagents, KOH is widely used due to its efficiency in generating micropores and small mesopores into the skeleton of various structured carbons. Various activation mechanisms have been proposed, while the fundamental mechanisms controlling chemical activation remain elusive due to a large amount of factors contributing to the activation processes. Generally, the reaction between carbon and KOH starts with dehydration of KOH into K_2O at 673 K, then the oxidation of carbon with H_2O to carbon oxide and carbonate. At higher temperature (~1073 K), the potassium carbonate largely decomposes into potassium oxide (K_2O) and CO_2 and finally be reduced by carbon to metallic potassium at 1073 K[15].All the redox reactions etch the carbon matrix to form the pore network, and then the generated H_2O and CO_2 through the gasification of carbon further contribute the development of the porosity (i.e. physical activation). Finally, metallic potassium inflow into the carbon structure and expands the carbon skeleton. The expansion is irreversible, and a high microporous structure is created after the removal of the metallic potassium and other

potassium compounds through washing.KOH, $ZnCl_2$ and CO_2 have been used as chemical agents, respectively, in the activation of Bituminous coal[16]to study the effects of the processing parameters on the chemical activation and to determine the optimal conditions for the chemical activation of bituminous coal. The results show that the impregnation ratio plays the most important role in the chemical activation, and the effects of the carbonization temperature and time are dependent on the chemical agents used. The gas evolution of hydrogen on the activation of carbon in KOH[17]was also analyzed. It has been suggested that higher KOH/C mass ratio, faster sweep gas flow and higher temperature can increase the hydrogen content, and large amount of hydrogen is favorable for the increase of porosity during the chemical activation.

Physical activation always needs longer time, higher temperature (973 K~1473 K) than chemical activation [18]. However, it is easier and safer than chemical activation to operate, including the use of no corrosive agents and no need of washing process. The mechanisms of physical activation are relatively simpler than chemical activation so the activation process is more controllable. No matter which activation methods are used, the key point is to achieve well-tuned pore sizes[19]and optimal distribution of pore sizes[20].

1.4.1.2 Graphene

Graphene, a two-dimension carbon monolayer, has recently drawn great interest in the applications of supercapacitors. Graphene is a single atomic layer of graphite, so it is known as the thinnest material, and has excellent properties including good conductivity(thermal conductivity: 5000 W/(m•K) and electrical conductivity: 6000 S/cm[21]),large SSA and large mechanical strength (Young's modulus: 1 TPa[22])[23].

The effective surface area of graphene-based electrode highly depends on the number of layers. Electrode made from single or few-layer graphene can have large capacitance due to the large SSA. Xia et al.[24] reported that the capacitance of an ideal single layer graphene-based EDLC can reach up to 500 F/g. However, it needs to break the strong van der Waals interaction of the π-stacked layers in graphite in order to produce graphene sheets (GNSs)[25, 26]. There are several methods available to prepare GNSs. The first approach is to grow GNSs on substrate, including chemical vapor deposition (CVD) on metal foil substrate like Cu and Ge [27, 28], epitaxial growth on single-crystal silicon carbide substrate[29, 30], and thermo-splitting on polycrystalline silicon carbide[31, 32]. The second one is the oxidation–exfoliation–reduction[33-35] of graphite powder (also called as reduced graphene oxide, r-GO). GNSs can also be directly exfoliated from graphite[36-40]by sonication, intercalation or quenching. Organic coupling reactions[41, 42]are an important bottom-up fabrication method for nano-GNSs. When using graphene as the electrodes in EDLCs, the r-GO is treated with chemical or thermal reduction in aqueous dispersion/organic dispersion/dry system [43-47]to maintain a high SSA or high-porosity structure. In general, capacitance can be larger than 200 F/g. Introducing three-dimensional, macroporous structure or "spacer materials" such as nano-diamond particles and carbon black particles[48-50] can help maintain the high SSA of individual sheets, however, regional aggregation of single-GNSs and GNSs is inevitable, which makes it difficult to realize GNSs in large scale.

1.4.1.3 Carbon nanotubes(CNTs)

CNTs are tubular structured graphene layer, including single-walled carbon nanotubes (tube diameter: 1-2 nm) and multi-walled carbon nanotubes. They have the

potential as electrode materials of high power density due to the tubular structure, good electrical conductivity [51]and strong mechanical resilience, which is 100 times higher than steel[52]. Although CNTs have smaller SSA than ACs, the storage of electric charges is strongly dependent on the surface area of CNTs[53-55]. Also, the tubular structure allows fast diffusion of electrolyte ions, resulting in a small equivalent series resistance and high energy density. Vertically aligned CNTs grown on conductive substrates have been widely used since entangled CNTs hinder fast ionic transport[56]. However, the high cost of CNTs hampers the use of CNTs for large scale fabrication.

1.4.1.4 Carbon aerogels and carbon mixtures

Another approach to increase the power densities of carbon-based supercapacitors is to use mixture of different carbon-based materials[57]. For example, Aerogels are always used in carbon-based composites with CNTs.

Carbon aerogels are mesoporous carbon materials with interconnected networks of carbon nanoparticles, which can be used as electrode materials without binder. It has been prepared via the sol-gel method and controlled by catalysts and the mass ratio of reactants[58].

In summary, carbon-based materials can be produced in variable physical forms that possess a wide-range of physical, chemical and electrochemical properties.

1.4.2 Electrolytes of EDLCs

The electrolyte can be liquid or solid once it has a high enough ionic conductivity. The most common used electrolytes are aqueous electrolytes. They are nonflammable, low cost, high ionic conductive, and can provide different pH environment as desired. However, the working voltage of aqueous electrolytes is usually limited by the water

decomposition potential, which is 1.229 V. Since the energy density is proportional to the product of capacitance and the square of voltage window's value, maximizing the operating potential windows can largely increase the energy density of EDLCs.

Organic electrolytes, such as tetraethylammonium tetrafluoroborate and triethylmethylammonium tetrafluoroborate in acetonitrile, are less prone to decompose so that they can provide a large voltage window[59]. However, organic electrolytes are flammable, toxic, expensive and inconvenient to assemble in air. All of these have limited the applications of organic electrolytes. Also, AC-based systems with organic electrolytes have worse electrochemical performance than those with aqueous electrolytes due to small conductivity and large effective size of electrolyte ions.

Another type of electrolytes is ionic liquids (ILs). Ionic liquids are molten salts that consist of organic ions at room temperature[60],such as N-butyl-N-methylpyrrolidinium bis(trifluoromethanesulfonyl)imide and triethylammonium nitrate. ILs have unique advantages at high temperature due to high vapor pressure, high thermal stability, good conductivity and wide electrochemical windows[61, 62]. For the same electrode materials, ionic liquid electrolytes provide the highest specific energy while aqueous electrolytes provide the highest power density[61].

Solid electrolytes are vital for the fabrication of flexible and all-solid-state ESDs, which allow the movement of ions within solid components. To sum up, the function of electrolytes is to provide free ions with high mobility, the choice of the electrolyte in SCs should be based on its specific electrode materials and performance requirements.

1.4.3 Separators of EDLCs

Separators of EDLCs require high electrical resistance, high ionic conductivity, strong mechanical strength and flexibility to offer good stability throughout the cycling life of SCs. Common used separators includes Poly(vinylidene fluoride)-based macroporous separators, commercial cellulose-based separators and the Celgard ™ separators.

It is worth pointing out that the assembling of electrodes can also affect the capacitive behavior of SCs[63], where an optimal preparation condition of the electrodes can help reduce electrochemical impedance due to good porosity and low contact resistance. A high-performed SC is the result of taking all components into careful consideration.

1.5 Pseudo-capacitors and hybrid capacitors

Pseudo-capacitors, which are based on fast and reversible Faradaic redox reactions on the surface of electroactive species such as metal oxides, metal-doped carbons, or conductive polymers[35], usually exhibit higher energy densities at the cost of shorter cycle life and lower charging rate than EDLCs. It shares similar energy storage mechanism with the batteries, but has faster electrochemical processes than in batteries. Note that all pseudo-capacitors have double layers, so the electrostatic double-layer capacitance are also included in pseudo-capacitors.

The two electrode materials for pseudo-capacitors and the hybrid capacitors are different, so asymmetric structure is typically used. As a result, the working voltage ranges of the positive electrodes and the negative electrodes are different in asymmetric

supercapacitors, the overall voltage window can be larger than that of the symmetric supercapacitors, which can effectively increase the energy density of SCs.

One common property shared by EDLCs and pseudo-capacitors is that the energy storage mainly involves the material near the interface between electrolyte and electrode. Thus decreasing the particle size can likely increase the usage of active materials by providing a larger surface area. It has been accepted that designing ultrathin nanostructures with size less than 10 nm can realize high-performance supercapacitors[64]. However, a balance between specific surface area and the corresponding pore size of electroactive materials is desired because large microporosity (leading to bad conductivity) and wide distribution of pore sizes (increasing "dead volume") will cause a dramatic loss of capacitance especially at a large current density[65].

Pseudo-capacitances are always obtained from conducting polymers (CPs) and transition metal oxides. Conducting polymers (CPs) are semi-conducted conjugated carbon chains. CPs can become conductive after doping process. Polyaniline (PANI), as an economical, high conductive, and easily fabricated material with high doping and de-doping rate during charging and discharging, has drawn great attention in the application of high capacitance supercapacitors[66]. Moreover, its well-bonded and flexibility structure needs no more extra binders or conductive additives. Other common used CPs include polypyrrole (PPy)[67], ethylenedioxythiophene (PEDOT) and polythiophene (PTh).However, the structural degradation during redox reactions always cause a poor cycling life.

Transition metal oxides, such as ruthenium oxides (RuO_2)[68], manganese oxides (MnO_2) and iridic oxide(IrO_2) have been proposed for SCs. The advantage of transition metal oxides is that they can switch easily among a series of continuous redox reaction due to a variety of oxidation states of the transition metals. The reported specific capacitance (C_s) can be as large as 1100 F/g[69], which is 4-5 times of that for ACs-based SCs. However, transition metal oxides are of poor conductivity.

Hybrid capacitors, which is a combination of EDLCs and pseudo-capacitors, can function simultaneously as asymmetric capacitors and composite capacitors, depending on the structure of the electrode materials[64]. It has been noted that combining carbon-based materials with high power density and pseudo-capacitive nanomaterials is an effective approach to further improve the energy density of supercapacitors without sacrificing power density as well as good cycling stability[70], i.e. adding polymers and/or transition metal oxides of high energy density. It has been demonstrated[71]that the intertexture can create a synergistic effect on electrochemical performance due to the desired hierarchical porous channels with good mechanical durability and high conductivity.

Other improvements in the performance of carbon-based EDLCs includes adding other elements such as nitrogen and sulfur in carbon-based materials[72]. Oxygen functional group can modify the surface property of carbon-based materials to improve the wettability of the materials in aqueous electrolytes and enhance electrochemical performance[73]. In summary, mixing pseudo-capacitive materials into the carbon network can introduce a synergistic effect, which can greatly enhance electrochemical performance of EDLCs. However, the high cost of preparing such sophisticated

architectures as well as the difficulty in purification hinders the practical applications of hybrid-supercapacitors.

1.6 Recent developments of biomass-based activated carbon supercapacitors

Biomass, one of the main renewable energy sources on the earth, is abundant, renewable, highly economical, natural and environmental-friendly. It is predicted that biomass will take over 70% of the renewable energy supply by 2030[74].In view of economical and sustainable development of supercapacitors, biomasses have attracted increasing interest as ACs' precursors for the preparation of the electrode materials of EDLCs. While appropriate carbon sources as precursors and improved synthesis processes are of great importance to obtain ACs of good capacitive properties, such as good porosities, large SSA, accessible average pore size and effective dielectric permittivity, various waste materials derived from plants and animals, and natural biomass-based materials have been successfully converted into ACs[75-82], including sunflower seed shells (SSS), cherry stones, wheat straw, banana fibers, saw dust, waste paper and animals' bones. A summary of the biomass-derived ACs' properties and specific capacitances are listed in Table 1.2[15].All these natural biomass-derived materials show good capacitive behavior with capacitances ranging from 168 F/g to 335 F/g, indicating their promising applications as EDLCs' electrodes.

As discussed above, the performance of EDLCs is dependent on the preparation of electrode materials. The preparation of ACs from biomass can be divided into two parts: pretreatment (hydrothermal carbonization or pre-calcination) and activation. Direct combustion of biomass will cause low energy recovery and emit large amount of gases

like CO_2 and SO_2. The pretreatment is essential to transform biomass into biochar[91-95], which has high heating value, high carbon constituent and low emission of CO_2. There are several carbonization approaches to obtain biochar, such as pyrolysis[91, 96, 97], gasification and hydrothermal carbonization (HTC)[98-101]. Among all those methods, HTC has promising advantages over others. HTC is a heat treatment conducted in an aqueous solution, where biomass is well dispensed in the solution, under self-generated pressure at a relatively much low temperature of 423 K ~ 623 K in comparison with other carbonizations. The whole procedure requires no pre-drying and can dissolve most of gases such as SO_2, CO_2 and NO_x in the aqueous solution without involving any toxic chemicals [102].The biochar produced by HTC is usually named as hydrochar[103]. Hydrochar generally has a low ash content, high carbon recovery, uniform chemical and structural properties and higher surface oxygen-containing groups than the conventional biochar produced by other carbonization methods like pyrolysis[102-104].It is also accessible to the introduction of nitrogen and other functional groups by using dopant-carbon precursors or additives[105]. However, hydrochar have no open porosity (i.e. closed and bottle-neck pores) and limited SSA even at a high temperature.

The main components in biomass are cellulose, a polysaccharide made up of glucose; hemicellulose, monosaccharides like xylose and pectinose, and lignin, a phenolic polymer. Different biomasses have different ratios of these components and different structures, which determine the specific properties of their derived products. It was reported [84][87] that using a chemical activation process after HTC processing, the oxygen-functional groups from the surface of biomass-derived hydrochars can be removed thoroughly. The as-prepared ACs exhibit efficiently open pores and form

microporous structures within large SSA, resulting in high-performance electrodes of EDLCs. The activation temperature [106]and different ratios of KOH/C[107]have great effects in designing the structure and morphology of ACs, such as SSA, average pore size, degreeofgraphitization and conductivity. In summary, the HTC-activation approach has the potential for the preparation of biomass-derived carbon-based electrodes for applications in SCs, which exhibit high specific capacitance and rapid charging and discharging capability.

Table 1.2 Properties and characteristics of some KOH-activated carbons as the supercapacitors electrodes derived from natural biomass-based materials[83]

Starting materials	SSA (m^2/g)	Pore Volume (cm^3/g)	Activation method	Electrolyte	Specific capacitance (F/g)
Cherry stones[84]	1273	--	Chemical (KOH)	H_2SO_4	232
				Organic	120
Fish scale[83]	2273	2.74	Chemical (KOH)	KOH	168
Pig bone[83]	2157	2.26	Chemical (KOH)	KOH	185
Sunflower seed shell[83]	2585	1.41	Chemical (KOH)	KOH	311
Waste paper[83]	526	--	Chemical (KOH)	KOH	180
Wood sawdust[83]	2967	1.35	Chemical (KOH)	Organic	236
Hemp[85, 86]	2287	1.45	Chemical (KOH)	Liquid	142
Coconut kernel pulp[87]	1200	0.60	Chemical (KOH)	H_2SO_4	173
Pistachio shell[88]	1009	0.67	Physical (Steam)	$NaNO_3$	80
Fir woods[88]	1016	0.75	Physical (Steam)	$NaNO_3$	105
Corncob[89]	1210	0.67	Physical (Steam)	KOH	314
Coffee endocarp[90]	1050	0.5	Physical (CO_2)	H_2SO_4	176
HFCS	1364	0.86	Self-Physical	KOH	168

1.7   Research needs and goals

Due to the great needs to develop high-energy density and high-power density ESDs based on renewable energy sources, we propose to produce a high-performance ACs-based SCs from several biomass materials, including high fructose corn syrup and soybean, through the HTC-physical activation process, which is low-cost and environmental friendly.

The goal is to 1)synthesize high-performed ACs-based electrode materials for EDLCs from biomass; 2) investigate the electrochemical performance of the SCs made from the biomass-derived activated carbon in a symmetric, two-electrode system in aqueous electrolyte for the optimization of the electrode materials, and the effect of electrochemical cycling on the structural integrity of the supercapacitors; 3) study the mechanical response of the biomass-derived ACs; and 4) study the effect of compression on electrochemical impedance.

1.8   Organization of the dissertation

The first chapter provides a history background and literature review on energy supply structure in the past. The important role of ESDs and the fundamental components for SCs are discussed. Different kinds of electrode materials and the preparation methods of high-performance electrodes for EDLCs are briefly introduced.

In chapter 2, a HTC-physical activation method is presented to synthesize activated carbons from high fructose corn syrup (HFCS). The surface morphology and porous structure are characterized by SEM, TEM and N_2 adsorption and desorption isotherm. The activated carbons from HFCS are present in spherical shape and possess a high

surface area of 1473 m^2/g. Increasing the activation time increases the total surface area and the portions of micropores. The electrochemical performance of the supercapacitors made from the HFCS-derived ACs is investigated. The largest specific capacitance and energy density achieved are 168 F/g at an electric current density of 0.2 A/g and 4.2 W·h/kg at a power density of 1.5 kW/kg. The experimental results show a similar increase trend of the specific gravimetric capacitance (C_s) with the increase of the total surface area and portion of micropores, suggesting the importance of the activation time in controlling the porous characteristics of the activated carbons and the role of micropores in the electrochemical characteristics of the supercapacitor cells made from the activated carbons.

In chapter 3, a two-step hydrothermal carbonization followed by physical activation to prepare activated carbons from soybean residue is presented. Hollow-porous carbon spheres are formed. For the activation temperatures at 850 °C, a transition of amorphous carbon to crystalline carbon occurs with a specific surface area of 517 m^2/g. Using the activated carbons as electrodes, symmetrical two-electrode supercapacitor cells with 6 M KOH aqueous system as electrolyte are built. The experimental results show that the activated carbons formed at 850 °C exhibit the largest specific gravimetric capacitance of 227 F/gat the scan rate of 2 mV/s. This study proves that the 3-step HTC-physical activation method is a promising "top-down" method to utilize biomass for the electrode materials of EDLCs, where the activation temperature plays an important role in controlling the porous structures.

In chapter 4, the mechanical responses of HFCS-derived activated carbon-based EDLCs in dry and wet status are studied. A series of compression tests are performed,

and the compressive load-displacement curves are recorded. The stiffnesses at various extents of consolidation for both dry and wet ACs-disks are calculated and compared. This study reveals the consolidation effect on the stiffness of the carbon materials; increasing the maximum compression load will cause an increase of stiffness of the ACs-disks. A simple model of porous materials is used to explain the increase in the stiffness of a compressed disk with the increase of mechanical deformation.

In chapter 5, the EIS of HFCS-based ACs under compression is studied. EIS is an effective way to analyze the frequency-related behavior of EDLCs, and to determine the charge transfer resistance and system resistance of EDLCs. The relationship between the mechanical deformation and the frequency-related EIS electrochemical behavior is explored. The results show that increasing compression force can reduce the resistance and enhance the capacitive performance of EDLCs due to its effect on reducing the diffusion layer's thickness and maximizing the contact with the separator. The results shed insights into the mechanisms controlling the performance and lifetime of carbon-based EDLCs.

CHAPTER 2.   HFCS-BASED ACSFOR EDLCS

2.1   Introduction

Electrochemical double layer capacitor (EDLC) is an important branch of energy

storage devices which show superiority in high power density and long cycle life.

Activated carbons (ACs) are of highly porous structure and large specific surface area

(SSA) (1000~3000 m^2/g), so they are ideal as the electrode materials of EDLCs[19]. The

precursors used for the synthesis of ACs and the specific activation method greatly affect

the electrochemical performance of ACs.

Biomass is an important renewable energy resource, which is eco–friendly. The

main components in biomass are cellulose, a polysaccharide made up of linked D-glucose;

hemicellulose, monosaccharides like xylose and pectinose; and lignin, a phenolic

polymer. Different biomasses have different ratios of these components and different

structures, which determine the properties of the derived products. Activated carbons

have been widely used as the electrode materials of energy storage devices and systems,

including lithium-ion batteries [108], lithium sulfur batteries [109, 110], and EDLCs

[75-81] . One of the common application is the biomass-derived activated carbons (ACs)

for EDLCs.

There are two important steps to synthesize ACs from biomass; the first step is the

pretreatment of the biomass, e.g. pyrolysis[91, 96, 97], gasification and hydrothermal

carbonization (HTC)[98-101],which converts biomass into biochar [91-95]to avoid the low energy recovery and large emission of harmful gases like CO_2 and SO_2. Among all these methods, HTC has promising advantages over others. HTC is a heat treatment conducted in an aqueous solution, where biomass is well dispensed in the solution, under self-generated pressure at a relatively low temperature of 150 °C~ 350 °C in comparison with other carbonizations. The whole procedure requires no pre-drying process and can dissolve most of gases such as SO_2, CO_2 and NO_x in the aqueous solution without involving any toxic chemicals[102]. The biochar produced by HTC is usually named as hydrochar[103]. Hydrochar generally has a low ash content, high carbon recovery, uniform chemical and structural properties and higher surface oxygen-containing groups than the conventional biochar produced by other carbonization methods like pyrolysis [102-104]. It is also accessible to nitrogen and other functional groups by using dopant-carbon precursors or additives[105]. However, hydrochar have no open porosity (i.e. closed and bottle-neck pores) and possess limited SSA.

The other one is the activation at higher temperature to further remove the impurities and develop porosity and high SSA. A variety of ACs have been derived from different biomasses, e.g. hemp[85, 86], corncob residue [89] and coconut kernel pulp [87]. The activation method can be divided into chemical activation and physical activation, based on the type of the activation agent. Usually, chemical activation is more effective than physical activation due to the series of reaction between the chemical agent, the intermediate compounds and the carbonaceous products, and it always leads to a higher

24

capacitance. However, the use of the corrosive agent like KOH during chemical activation have added extra washing steps into the preparation process, and the high requirements like an anti-corrosive furnace tube would cause a high cost, e.g. Ni-based super alloy tube. It's worth mentioning that almost all the reported works require activation agent, just few studies on self-activation are reported.

High-fructose corn syrup (HFCS) is a liquid sweetener alternative to sucrose (table sugar) for commercial use like food processing industry and Beverage Manufacturing[111]. Its main composition is glucose and fructose and has an abundant production, thus it is an excellent carbon source for the application in EDLCs. It has been reported that[112]the microporous and mesoporous carbon aerogels from D-fructose could achieve a surface area of 1200 m^2/g and a specific capacitance of 245 F/g at a current density of 1 A/g. However, the use of HFCS to produce ACs for the application in EDLCs has not been studied.

In this study, HFCS was used as the precursor for the synthesis of ACs via hydrothermal carbonization process and physical self-activation process. Fructose is the basic products of some raw biomass materials, such as the enzymatic upgrade product of starch, the catalytic reaction product of raw cellulosic biomass and the isomerization product of glucose [113]. Using fructose or HFCS as the starting precursors, it can be treated as a bottom-up synthesis method of ACs. The effect of activation time on the surface area and porosity of the prepared ACs was investigated, and the electrochemical

25

performance of the EDLCs made from the HFCS-derived ACs was studied in 6 M KOH aqueous solution.

2.2 Experimental procedure

2.2.1 Materials and preparation

The precursor for hydrothermal carbonization process is HFCS55 (Cargill, Wayzata, MN). The HFCS55 is a liquid of light yellow-green color with ~77.1 wt.% solid, in which there is ~55 wt.% fructose. 70 ml of an aqueous solution consisting of ~10.4 vol.% HFCS55 and ~89.6 vol.% DI water was placed in a Teflon-lined autoclave of 100 ml, which was placed in a pre-heated oven at 220 °C ± 2 °C. A thermocouple of K-type was attached to the Teflon-lined autoclave to monitor the temperature evolution. It took ~2.5 hrs for the Teflon-lined autoclave with the aqueous solution to reach the temperature of 220 °C. The temperature of the Teflon-lined autoclave with the aqueous solution was then maintained at 220 °C for 1 hr before letting the Teflon-lined autoclave cool down to room temperature in the oven in air. The hydrothermal carbonization of the HFCS 55 took place during the heating and cooling process.

The hydrothermal product was first sonicated at room temperature for 1 hr. Using Grade 2 Whatman filter papers (Sigma-Aldrich, St. Louis, MO), the carbonized material was then collected by the filtration method with the use of DI water. The collected carbonized material was dried in an oven at 100 °C for 12 hrs.

The activation of the carbonized material was performed in a tube furnace (21100 tube furnace, Barnstead Thermolyne Drop., Ramsey, MN) with the passage of nitrogen gas at a temperature of 850 °C for different times. This temperature was selected according to exploratory work (see Figure 2.8). Note that no CO_2, steam or any oxidizing agents were used in the activation in contrast to the activation of carbonized materials reported in the literature. The whole activation process was conducted by the self-generated CO_2, H_2O and other volatile materials in high temperature. The ACs were collected in a vial after the furnace was cooled down to room temperature in the nitrogen environment, and then dried in an oven at 100 °C overnight. Note that the use of nitrogen gas avoided the burning and oxidation of the carbonized material during the activation and the cooling, respectively.

2.2.2   Characterization of surface morphology and composition analysis

The obtained samples were characterized with X-ray diffraction (Bruker D8, CuK_α, 40 kV, 30 mA) and FT-IR (Thermo Scientific Nicolet iS50 FT-IR spectrometer). The morphology and selected area electron diffraction (SAED) patterns of the activated carbons were examined using Field Emission Scanning Electron Microscopy (FESEM) (Tescan MIRA3 LMH) at 10 kV and Transmission Electron Microscopy (TEM) (JEOL 2100-F) at 200 kV.

2.2.3   Characterization of surface area and porosity

To determine the surface area, pore size and pore size distribution (PSD) of the activated carbons, the nitrogen adsorption-desorption isotherms were measured by an

27

automated gas adsorption analyzer (Micromeritics surface characterization, Norcross, GA). All the samples were heat-treated at 200°C in a vacuum for 2 hrs to degas. The Brunauer-Emmett-Teller (BET) and Density functional theory (DFT) methods were used to analyze the experimental results of nitrogen adsorption. The BET is a traditional method that is based on the relation between the pore size and the condensation pressure[114].However, for pores of micropore sizes (< 2 nm), capillary condensation is impossible, instead, the pore-filling will go continuously along with the increased pressure. Thus, the DFT method [115, 116]was used to interpret the whole adsorption isotherm and extract the detailed PSD, which is a molecular dynamics method that considers and calculates the balanced density distribution of both absorbed fluid on the surface and the fluid in the pores.

2.2.4   Assembly of EDLCs and electrochemical measurement

Supercapacitor cells of symmetrical type (two-electrodes) were prepared with the ACs as the electrode material, using a Teflon screw two-electrode cell (Swagelok cell). The ACs were first ground and dried in oven until there was no weight change. 1 mg ACs was placed on the surface of the current collector made from stainless steel to form an electrode. The electrodes were screwed tightly in a Teflon screw two-electrode cell with a 696 glass microfiber filter (VWR International, LLC.) as separator. Considering the wide use of KOH solutions in supercapacitors and the average pore size of ACs, 6 M KOH solution was used as the electrolyte. Note that no binders and additives were used in the preparation of the electrodes, since the preliminary results show that there is no

observable difference of specific gravimetric capacities between pure ACs and the same

ACs with PTFE binder of 8 wt.% (see Figure 2.8).

The electrochemical performance of the AC-based supercapacitor cells was

characterized using a VSP 5-channel potentiostat system (BioLogic Science Instruments,

Seyssinet-Pariset, France). The potential window for the cyclic voltammetry (CV)

measurement was in a range of 0 to 1 V, and the voltage scanning rate was in a range of 2

to 100 mV/s. The current densities for the galvanostatic charging and discharging (GC)

measurement were in a range of 0.2 A/g to 10 A/g with the voltage in a range of 0 to 1 V.

The EIS (electrochemical impedance spectroscopy) measurement was recorded in a

frequency range of 20 mHz to 1 MHz with a sinusoid alternative voltage of 10 mV.

To analyze the effect of the activation time on the topological characteristics of ACs

and the electrochemical characteristics of AC-based supercapacitor cells, the prepared

ACs are designated as AC-x. Here, the "x" represents the activation times of 1, 2, 3, and

4 hrs.

2.3 Results and discussion

2.3.1 Analysis of surface morphology

Figure 2.1 shows SEM images of the ACs formed via the HTC processing and the

physical activation. The HTC process usually contains a series of hydrolysis, dehydration,

decarboxylation and aromatization reactions. For fructose and glucose, they will firstly

dehydrate into hydroxymethylfurfural (HMF), and then experience carbonization and polymerization around 160 °C~ 180 °C, which lead to the nucleation and growth of hydrochar spheres. It has been noted that HMF is hydrophilic due to the existence of carboxyl, so the generated spheres stick together as shown in Figure 2.1a. The average size of the carbon spheres is ~1 μm.

Figure 2.1b-2.1e show the SEM images of the ACs with the activation times of 1, 2, 3, and 4 hrs. The activation of the carbonized spheres at 850 °C does not cause any growth and significant topological change of the carbon spheres, while it causes slight decrease of the diameter of carbon spheres and local solid-state sintering. Such behavior is due to the de-oxidization of hydrochar. Hydrochar is of high oxygen content with the existence of oxygen functional groups. The activation at high temperature removes the oxygen functional groups and generates some pore canals to the surface, which increase the SSA of the obtained carbon spheres. The local solid-state sintering is due to the surface interaction between carbon spheres, which causes the migration of atoms and molecules.

FIGURE 2.1 SEM images of carbon spheres made from HFCS55 via hydrothermal carbonization and physical activation; (a) without activation (AC-0), (b) with activation of 1 hrs (AC-2), (c) with activation of 2 hrs (AC-2), (d) with activation of 3 hrs (AC-3), and (e) with activation of 4 hrs (AC-4)

Figure 2.1b-2.1e show the SEM images of the ACs with the activation times of 1, 2, 3, and 4 hrs. The activation of the carbonized spheres at 850 °C does not cause any growth and significant topological change of the carbon spheres, while it causes slight decrease of the diameter of carbon spheres and local solid-state sintering. Such behavior is due to the de-oxidization of hydrochar. Hydrochar is of high oxygen content with the existence of oxygen functional groups. The activation at high temperature removes the oxygen functional groups and generates some pore canals to the surface, which increase the SSA of the obtained carbon spheres. The local solid-state sintering is due to the surface interaction between carbon spheres, which causes the migration of atoms and molecules.

Figure 2.2 shows TEM images of the carbon particles heat-treated with different activation times. The activated carbon particles are presented in spherical shape in accord with the SEM images shown in Fig. 2.1b-2.1d. Aggregated and stacked AC spheres are observed in all the TEM images, suggesting the neck formation associated with local solid sintering. There is no significant difference between the diameters (~0.8 μm) of the AC spheres. The embedded SADP pattern (selected area diffraction pattern) in Fig. 2.2d reveals that the AC spheres are amorphous. Such a result suggests that the activation of the carbon spheres at 850 °C does not cause detectable phase change from amorphous phase to crystalline phase.

(a)   (b)

(c)   (d)
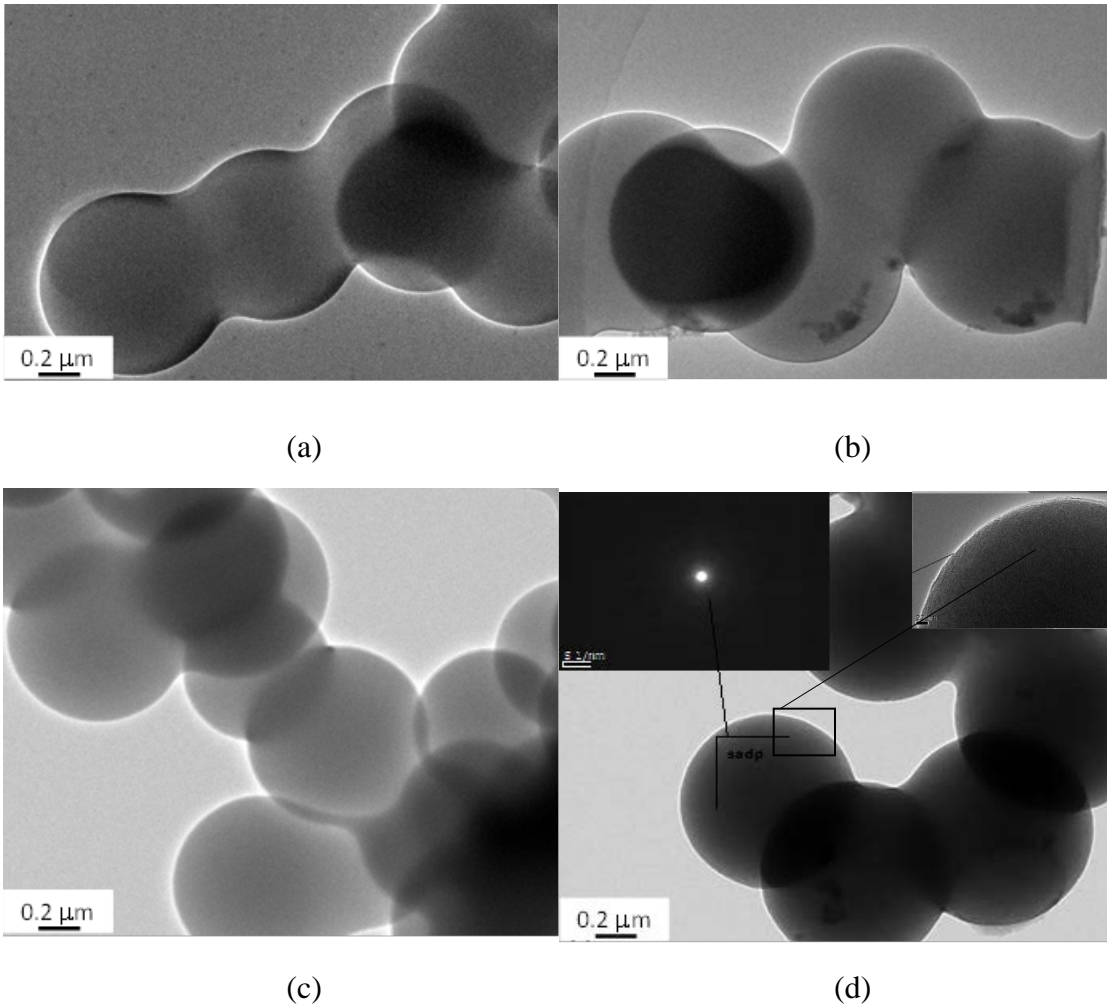
FIGURE 2.2 TEM IMAGES OF CARBON SPHERES TREATED WITH DIFFERENT ACTIVATION TIMES; (A) 1 HR (AC-1), (B) 2 HRS (AC-2), (C) 3 HRS (AC-3), AND (D) 4 HRS (AC-4)

2.3.2   Composition analysis

Figure 2.3 shows the XRD patterns of AC-x. The weak and broad peaks at around 20°, 25° and 43° corresponding to amorphous carbon and (002) and (100) planes of graphite, respectively, indicating a very low graphitization of AC-xs.
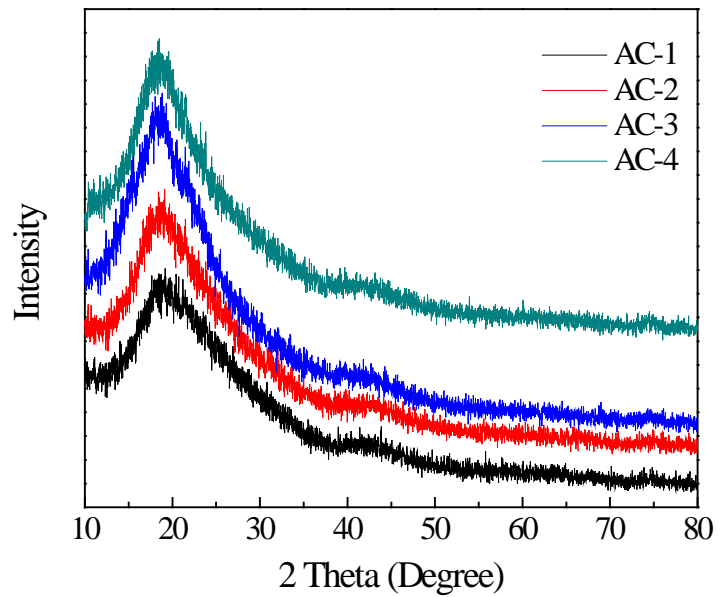
FIGURE 2.3 XRD PATTERNS OF AC-XS

2.3.3   Surface area and PSD analysis

(a)   (b)
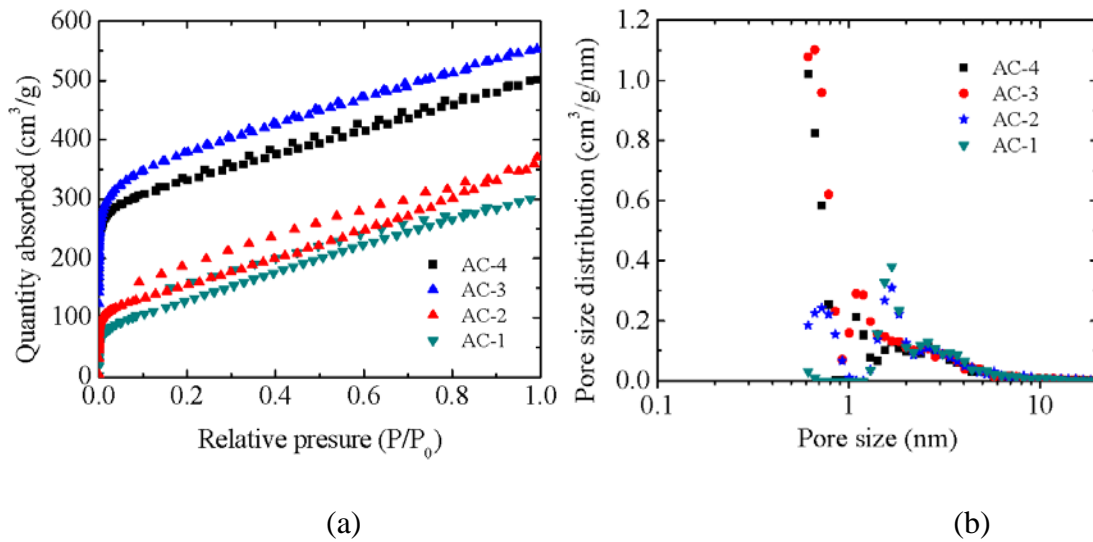
FIGURE 2.4 ADSORPTION BEHAVIOR OF AC-X: (A) NITROGEN ADSORPTION-DESORPTION ISOTHERMS, AND (B) DISTRIBUTION OF THE PORE SIZES CALCULATED FROM THE ADSORPTION ISOTHERMS VIA THE DFT (DENSITY FUNCTIONAL THEORY) METHOD

To determine the porous characteristics of the AC spheres, the nitrogen adsorption-desorption isotherms were measured by an automated gas adsorption analyzer (Micromeritics surface characterization, Norcross, GA). Figure 2.4a shows the nitrogen adsorption-desorption isotherms of the AC spheres of AC-xs (x: 1, 2, 3, and 4.). The isotherms of all the AC spheres show a combination of Type I and Type II features[117]. There is a rapid increase of the absorbed quantity in the range of low relative pressure, which is associated with the filling of micropores. This trend is the characteristic of Type I structure, indicating the presence of microporous structure. After the stage of rapid adsorption, the absorbed quantity increases slowly with the increase of the relative pressure, showing the characteristic of Type II structure. Such behavior suggests the presence of macroporous structure. The hysteresis and the increase of the absorbed quantity with the increase of the relative pressure reveal the presence of some mesopores. Note that the slope of the absorbed quantity v.s. relative pressure is associated with the filling of mesopores.

Figure 2.4b shows the distribution of the pore sizes of the AC spheres of AC-x, which was calculated by the DFT method. The AC spheres of AC-1 exhibits relatively monodisperse distribution with the largest differential pore volume at the pore size of 1.68 nm; the AC-2 exhibits bimodal distribution with the largest differential pore volume at the pore size of 1.68 nm, both the AC-3 and AC-4 have a similar distribution of pore sizes with the largest differential pore volume at the pore size of ~0.66 nm. Such a trend

reveals that increasing the activation time from 1 hr to 4 hrs leads to the decrease of the average pore size and the fraction of mesopores.

TABLE 2.1 POROUS PARAMETERS OF AC-X

Sample	Average pore diameter (nm)	S_{BET} (m^2/g)	S_{DFT} (m^2/g)	V_{total} (cm^3/g)	S_{micro} (m^2/g) (area%)	S_{meso} (m^2/g) (area%)	V_{micro} (cm^3/g) (vol%)	V_{meso} (cm^3/g) (vol%)
AC-1	5.52	399	433	0.55	264 (61)	169 (39)	0.19 (35)	0.36 (65)
AC-2	4.50	509	543	0.57	395 (73)	148(27)	0.26(46)	0.31(54)
AC-3	2.51	1364	1429	0.86	1280 (90)	149 (10)	0.50 (58)	0.36 (42)
AC-4	2.54	1223	1473	0.76	1328 (90)	145 (10)	0.44 (58)	0.33 (42)

Table 2.1summaries the surface characteristics of the AC spheres of AC-x. Two different methods were used to calculate the total surface area; one is the BET method with the calculated total surface area as S_{BET}, and the other is the DFT method with the calculated total surface area as S_{DFT}. The total pore volume was calculated at a relative pressure of 0.99. The DFT method was used to calculate the surface areas (S_{micro} and

S_{meso}) and pore volumes (V_{micro} and V_{meso}) of the micropores and mesopores. Note that

$S_{DFT} = S_{meso} + S_{micro}$ and $V_{total} = V_{meso} + V_{micro}$ (V_{total}: total pore volume).

From Table 2.1, one can note that the total surface area of S_{BET} increases from 399 m^2/g to 1364 m^2/g, and the ratio of S_{micro}/ S_{DFT} increases from 61 % to 90 % with the increase of the activation time from 1 hr to 3 hrs. There is no significant difference of the surface parameters between the AC spheres of AC-3 and AC-4. Such a trend suggests the important role of the activation time in controlling the evolution of the porous structures of ACs for the activation of carbonized materials at high temperatures. There likely exists a threshold for the activation time, above which the activation will not significantly change the characteristics of the porous structures of ACs. It is worth mentioning that the threshold of the activation time is dependent on the activation conditions and the structures of carbonized materials.

It is noted that the AC spheres of AC-4 have the largest total surface area and the surface area of micropores, and the AC spheres of AC-3 have larger S_{micro} and V_{micro} than AC-4. The more the amount of micropores, the higher is the total surface area.

2.3.4   Electrochemical analysis

Figure 2.5 shows the Nyquist plots of the AC spheres of AC-x, in which a semicircle and a spike appear in the high and low frequency regions, respectively. The semicircle suggests that the electron motion is the dominant mechanism controlling the electrical conductivity of the AC spheres in 6 M KOH in the high frequency region, and the AC spheres exhibit resistive nature. The spike reveals the capacitive behavior of electric

37

double layer in the AC spheres in the low frequency region. There is a transition between these two regions for medium frequency, in which both ionic transport and electron motion determine the electrical conductivity of the AC spheres. It is worth mentioning that multiple EIS measurements (>4) were performed for the same conditions. All the EIS results exhibit similar trend, which suggests that the Nyquist plots of the AC spheres reveal the impedance characteristics of the AC spheres of AC-x.

(a)   (b)
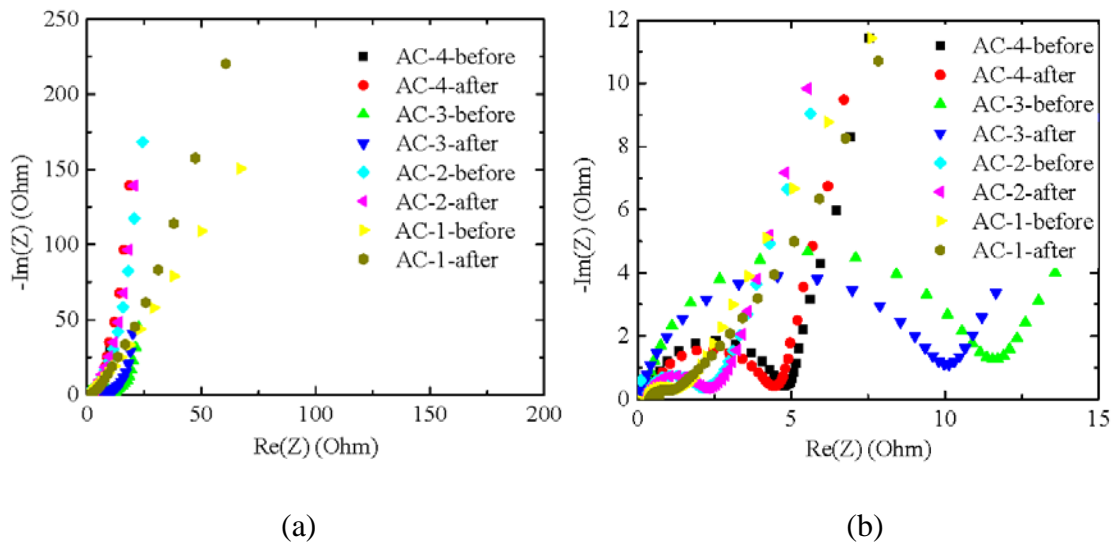
FIGURE 2.5 (A) NYQUIST PLOT OF THE AC SPHERES OF AC-X BEFORE AND AFTER 50 CYCLES OF CV TEST AND 60 CYCLES OF GC TEST, AND (B) ENLARGED VIEW OF THE NYQUIST PLOT OF (A) IN THE HIGH FREQUENCY RANGE

In general, the electrochemical impedance of a supercapacitor can be described by a lumped element model[118], consisting of 1) series resistance (R_s), depending on the electrolyte conductivity and the intrinsic resistance of separator, 2) AC/electrolyte interfacial impedance of capacitance (C_{dl}), resistance to charge transfer (R_{ct}), and the Warburg impedance, and 3) the capacitance and resistance associated with the defects of

current collector and separator. Using a lumped element model to analyze the Nyquist

plots of the AC spheres of AC-x in both the low and high frequency regions, one obtains

the values of the individual elements.

TABLE 2.2 FITTING VALUES OF R_S, R_{CT} AND C_{DL} OF THE SUPERCAPACITORS MADE FROM THE AC SPHERES OF AC-X BEFORE AND AFTER THE CYCLING TESTS (50 CYCLES OF CV TEST AND 60 CYCLES OF GC TEST)

	1h		2h		3h		4h	
	before	after	before	after	before	after	before	after
R_s	0.31±	0.31±	0.31±	0.32±	0.28±	0.25±	0.42±	0.46±
(ohm)	0.01	0.01	0.01	0.01	0.01	0.01	0.01	0.02
R_{ct}	2.77±	2.83±	1.64±	1.69±	10.83±	8.30±	4.16±	3.61±
(ohm)	0.02	0.02	0.01	0.01	0.05	0.05	0.02	0.02
C_{dl} (µF)	20.3±	19.8±	14.6±	14.1±	17.4±	23.2±	20.6±	24.4±
	0.1	0.1	0.1	0.1	0.1	0.1	0.1	0.1
τ (µs)	56.2±	56.0±	23.9±	23.8±	188.6±	192.7±	85.8±	88.1±
	0.2	0.2	0.2	0.2	1.1	0.8	0.4	0.4

Table 2.2 lists the fitting values of the R_s, R_{ct} and C_{dl} of the supercapacitors made

from the AC spheres of AC-x before and after the cycling tests (50 cycles of CV test and

60 cycles of GC test). Here, the characteristic time, τ, is calculated as $R_{ct}C_{dl}$, which is a

function of average pore size and associated with the ionic motion in small pores. It is

evident that there are no significant differences of the values of the four parameters for

the supercapacitor cells before and after the cycling tests. The cycling tests have no significant effect on the values of these four parameters. The supercapacitors made from the AC spheres of AC-3 have the smallest R_s, the largest R_{ct}, and τ in accord with the distribution of the pore sizes in Fig. 2.5b.

A knee frequency is defined as the initial frequency for the transition from the predominantly resistive behavior to the predominantly capacitive behavior[119, 120]. For frequency less than the knee frequency, ions (K^+) in electrolyte undergo directional migration to accumulate inside the pores of AC spheres, and the supercapacitor cell exhibits a good capacitive behavior. That is to say that a large knee frequency is preferable. The variation of the normalized capacitance with frequency is shown in Fig. 2.6, in which the capacitance is normalized by the corresponding capacitance at the frequency of 0.02 Hz. The normalized capacitance decreases with increasing frequency, and there is a sharp decrease of the capacitance in the frequency range of 0.2-0.6 Hz. From Fig. 2.6, the knee frequency is determined as the frequency at which the normalized capacitance is 0.8[119, 120]. The knee frequencies of the supercapacitors made from the AC spheres of AC-x are 0.14, 0.13, 0.079 and 0.067 Hz for the AC spheres of AC-4, AC-2, AC-3, and AC-1, respectively. The supercapacitors made from the AC spheres of AC-4 and AC-2 exhibit better capacitive characteristics than the other two. It needs to point out that the knee frequency is dependent on the microstructure of AC spheres, electrolyte, separator, and the assembling of the supercapacitor cells，so the value of knee

frequency is affected by the accessibility of the pores, the SSA, the depth and structure of the pores and the electric conductivity.
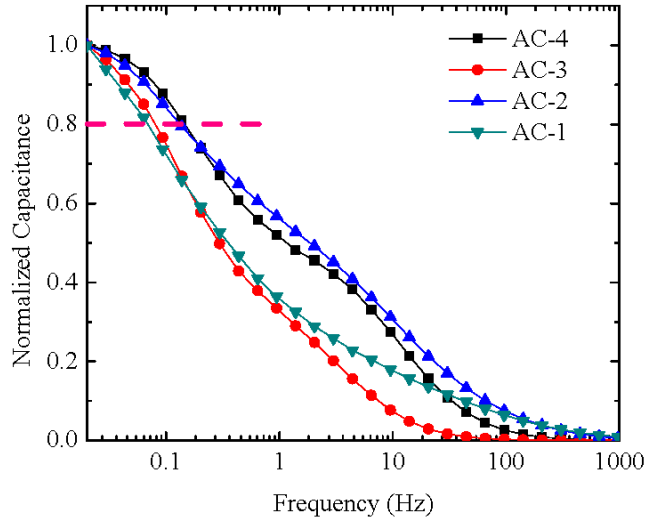
FIGURE 2.6 VARIATION OF NORMALIZED CAPACITANCE WITH FREQUENCY FOR THE SUPERCAPACITOR CELLS MADE FROM THE AC SPHERES OF AC-XS

Before investigating the electrochemical performance of the supercapacitor cells made from AC-xs activated at 850°C for different activation time, preliminary experiments had been performed. It was said that sometimes adding the binder like PTFE could help the electrode materials maintain a stable dispersion thus increase the electro conductivity and lead to an increase of the capacity. Thus a comparison study was conducted between pure AC spheres of AC-3 and the AC spheres of AC-3 with PTFE of 8 wt.% at a scanning rate of 10 mV/s. Figure 2.7 is the comparison results of these specific gravimetric capacity, from where we can see that the EDLC assembled with pure AC-3 possesses a slight higher specific gravimetric capacity than the one assembled with a PTFE mixture. Based on this result, the subsequent experiments were done with pure ACs.
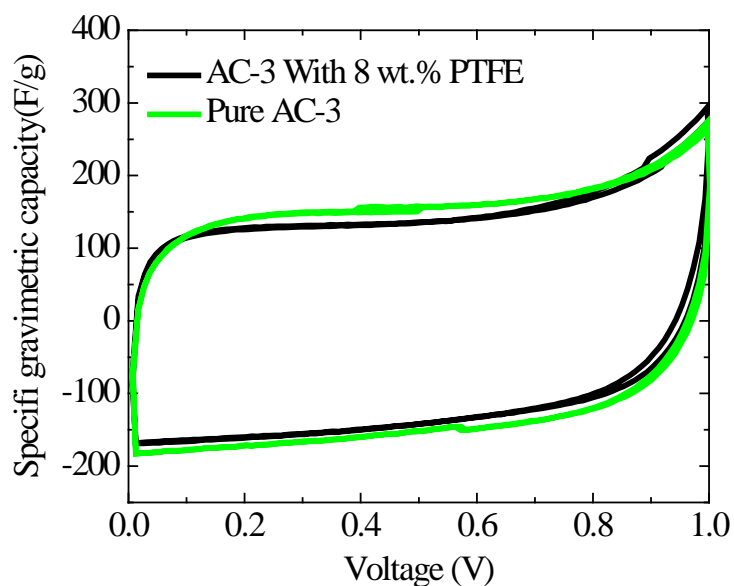
FIGURE 2.7 COMPARISON OF SPECIFIC GRAVIMETRIC CAPACITY BETWEEN PURE AC SPHERES OF AC-3 AND THE AC SPHERES OF AC-3 WITH PTFE OF 8 WT.% (SCANNING RATE: 10 MV/S)

Figure 2.8a shows the I-V (current and voltage) curves of the supercapacitor cells made from the AC spheres of AC-1 for various scan rates. The quasi-rectangular shape of the IV curves suggests a good capacitive behavior of the supercapacitor cells and good stability of AC spheres in the aqueous KOH electrolyte. The large enclosed area and the steep charge and discharge segments reveal that the supercapacitor cells possess excellent electrochemical performance. Note that increasing the scan rate leads to the deviation of the IV curves from rectangular shape, which is likely due to the presence of the characteristic time of τ associated with the migration and accumulation of ions. In general, the resistance to ionic motion and the resultant force acting onto the ions accumulated near the surfaces of pores are functions of local electric field (current density). The increase in the scan rate leads to temporal change of local electric field (current density),

and alter the motion of ions in and near pores. This trend causes the deviation of the IV

curves from the ideal shape of rectangle, and the deviation from the ideal shape of

rectangle increases with the increase of the scan rate.

The specific capacitance of one single electrode for a two-electrode supercapacitor

system can be calculated from both CV and GC measurements. Using the IV curves, the

specific gravimetric capacitance (SGC) in the unit of F/g can be calculated as [121,

122]

$$C = \frac{2I}{mv} \tag{2.1}$$

where I (A) is the electric current intensity, m (g) is the mass of single electrode, v (V/s)

is the scan rate. The average specific gravimetric capacitance (F/g) can be calculated

from the integration of voltammetric charge as

$$C = \frac{1}{mv} \frac{\int I(V)dV}{\Delta V} \tag{2.2}$$

where ΔV is the voltage window. Note that the mass can be replaced with area or volume,

which gives the specific areal capacitance and the specific volumetric capacitance.

(a)

(b)

(c)

(d)

(e)

(f)
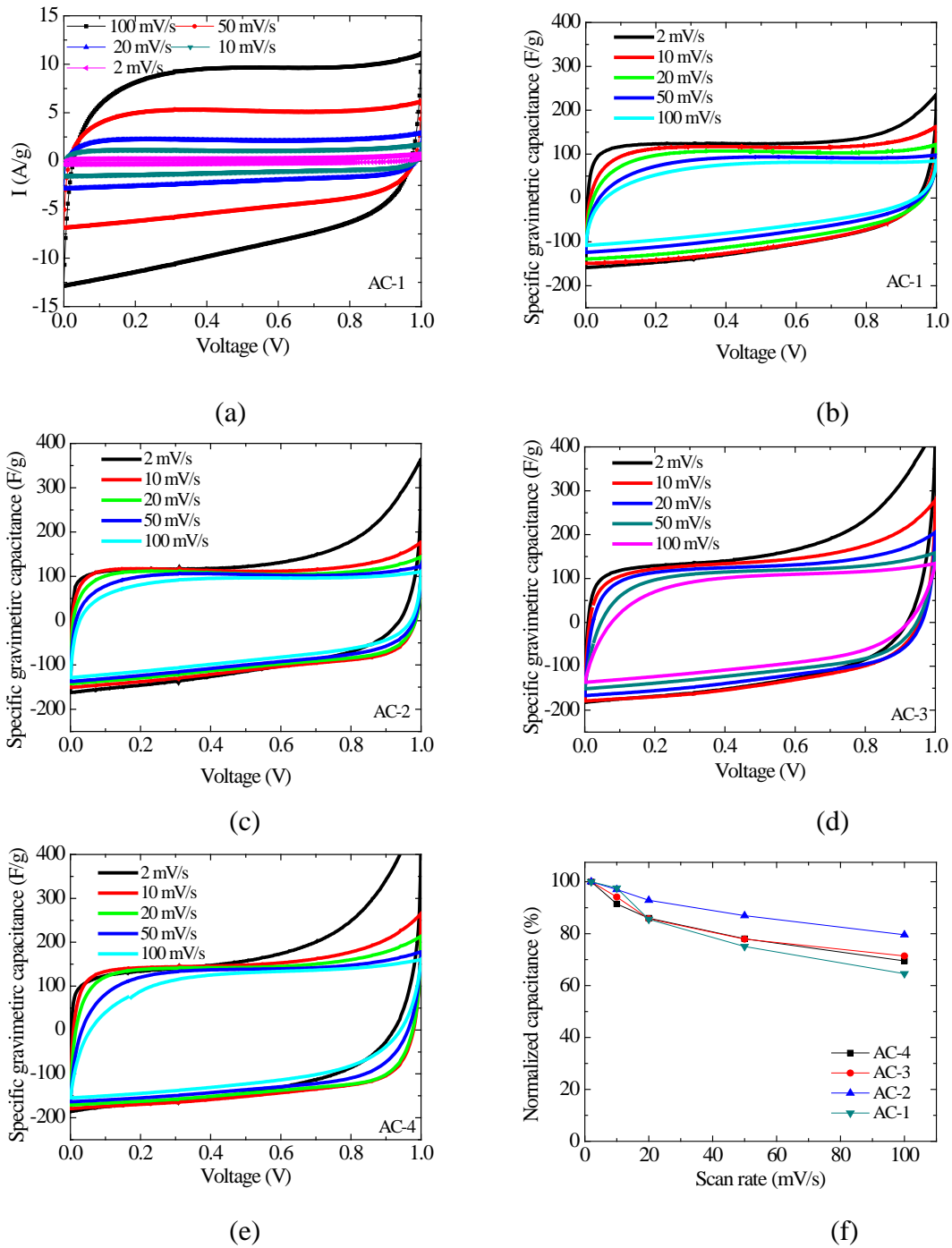
FIGURE 2.8 ELECTROCHEMICAL PROPERTIES OF THE SUPERCAPACITOR CELLS MADE FROM THE AC SPHERES OF AC-XS AT TENTH CYCLE; (A) IV CURVES OF AC-1, (B)-(E) CV CURVES OF AC-XS, AND (F) RATE DEPENDENCE OF NORMALIZED CAPACITANCE OF AC-XS

Using Eq. (2.1) and the IV curves, one can obtain the CV (capacitance and voltage) curves. Figure 2.8b-e shows the CV curves of the supercapacitor cells made from the AC spheres of AC-x for the tenth cycle for the scan rate in the range of 2 to 100 mV/s. All the CV curves are presented in a quasi-rectangular shape, indicating that all the AC spheres of AC-x possess microporous structures in accord with the measurement of the nitrogen adsorption– desorption isotherms and good capacitive characteristic for the charge storage. One can note that the CV curve at the smallest scan rate of 2 mV/s exhibits a spike at the voltage of 1 V for all the supercapacitor cells. The magnitude of the spike decreases with the increase of the scan rate. For the scan rate of 100 mV/s, the CV curves become more symmetric, and the spike at the voltage of 1 V nearly disappears. Such behavior reveals the presence of fast charging and discharging in the form of non-Faradic current at high scan rates.

Figure 2.8f shows the rate dependence of normalized capacitance of the supercapacitor cells made from the AC spheres of AC-xs, in which the capacitance of the corresponding supercapacitor cells measured at the scan rate of 2 mV/s was used in the normalization. Note that all the capacitances used in the calculation of the normalized capacitance is the average specific gravimetric capacitance at the tenth cycle, and the average specific gravimetric capacitances of the tenth cycle at the scan rate of 2 mV/s are 124, 133, 154 and 164 F/g for the supercapacitor cells made from the AC spheres of AC-1, AC-2, AC-3 and AC-4, respectively. It is evident that the supercapacitor cells made from the AC spheres of AC-2, which have the smallest τ, have the best rate

dependence with 79.6% of 133 F/g at the scan rate of 100 mV/s, and the supercapacitor

cells made from the AC spheres of AC-3 and AC-4 exhibit similar trend with ~70% of

154 and 164 F/g, respectively, at the scan rate of 100 mV/s. It is worth mentioning that

there are a variety of factors controlling the rate dependence of the capacitance of a

supercapacitor, including the distribution of pore sizesand surface properties, etc.

| (a) | (b) |
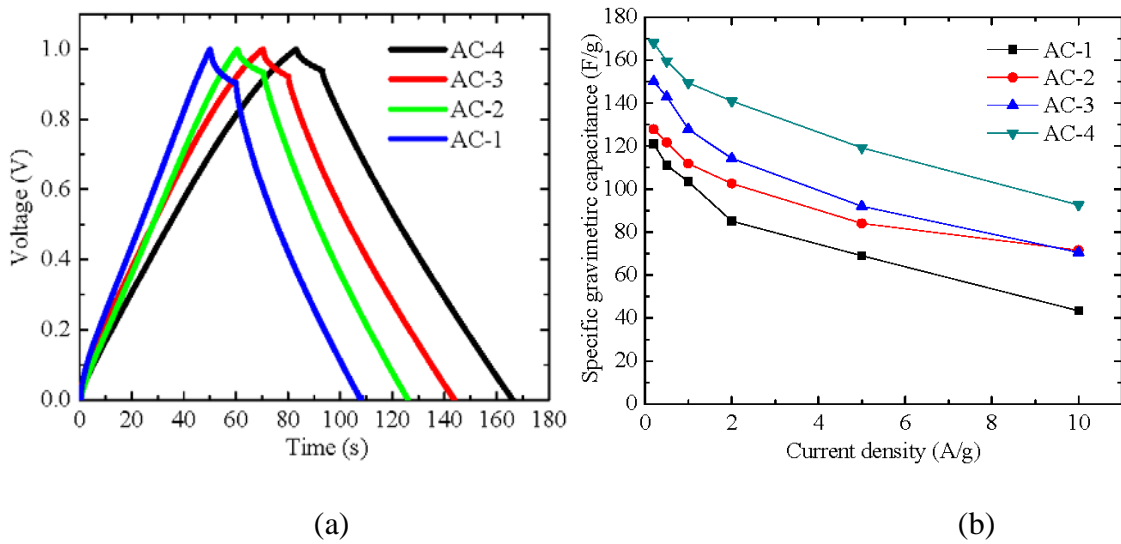
FIGURE 2.9 (A) GC CURVES OF THE SUPERCAPACITOR CELLS MADE FROM THE AC SPHERES
OF AC-XS AT THE TENTH CYCLE FOR AN ELECTRIC CURRENT DENSITY OF 0.5 A/G, AND (B)
VARIATION OF SGC WITH ELECTRIC CURRENT D
ENSITY

Galvanostatic charging and discharging measurements of the supercapacitor cells

made from the AC spheres of AC-xs were performed for electric current densities in a

sequence of 0.2 to 10 A/g with a voltage window of 0-1 V. For the GC tests, the specific

gravimetric capacitance is calculated as

$$C = \frac{4i}{\Delta V / \Delta t} \tag{2.3}$$

where i is the electric current density related to total mass of both electrodes, and $\Delta V/\Delta t$

46

is the slope of the discharging curve after the IR drop.

Figure 2.9a shows the GC curves of the supercapacitor cells made from the AC spheres of AC-x at the tenth cycle for an electric current density of 0.5 A/g. The GC curves display a triangle-like shape with reasonable symmetry, indicating good capacitive behavior of all the supercapacitor cells made from the AC spheres of AC-x. There exists an IR drop at the onset of the discharging, indicating the energy loss associated with the internal resistance of the supercapacitor cells. The SGCs are 111.1, 121.7, 142.9, and 159.5 F/g for the AC spheres of AC-1, AC-2, AC-3 and AC-4, respectively, compatible with the results from the CV measurement. Such a trend again demonstrates the importance of the activation time in determining the electrochemical performance of the supercapacitors made from ACs.

Figure 2.9b shows the variation of the SGC measured from the GC test with electric current density for the supercapacitor cells made from the AC spheres of AC-x. The SGC of all the supercapacitor cells decreases with the increase of electric current density, suggesting the effect of electric current density on the motion of ions and the energy storage. The larger the electric current density, the less is the ions accumulated at the electrolyte/electrode interface.

The supercapacitor cells made from the AC spheres of AC-4 have the largest SGC, which decreases from 168 F/g for the electric current density of 0.2 A/g to 159.5 F/g and 92.6 F/g for the electric current densities of 0.5 and 10 A/g, respectively. The supercapacitor cells made from AC-1 have the smallest SGC. The largest decrease of the

SGC for all the supercapacitor cells occurred for small electric current density. This trend suggests that there likely exists the effect of electric field (current) on the motion of ions, i.e. the electrophoretic velocity of ions, near the interfaces between electrolyte and AC spheres. The larger the electric current density, the larger is the driving force for the motion of ions. The interaction between AC spheres and the ions in electrolyte likely cannot counterbalance the driving force on the ions, and more ions can easily move away from AC spheres and migrate back to the electrolyte. This causes the reduction of ions accumulated in the AC spheres and the decrease of the capacitance.

The effect of electrochemical cycling on the capacitive behavior of the supercapacitor cells made from the AC spheres of AC-x was studied for the charging-discharging cycles up to 2000 at an electric current density of 0.5 A/g. Figure 2.10a shows the effect of charging-discharging cycle on the capacitive behavior of the supercapacitor cells. For the supercapacitor cells made from AC-1 and AC-2, the specific gravimetric capacitance decreases relatively fast for the first few cycles, and the cells approach relatively stable state with small decrease in the capacitance with the increase of the cycle number. For the supercapacitor cells made from AC-3 and AC-4, the specific gravimetric capacitance decreases slowly with the increase of the cycle number and then approaches relatively stable states. The supercapacitor cells made from the AC spheres of AC-4 have the largest specific gravimetric capacitance, and the supercapacitor cells made from the AC spheres of AC-1 have the smallest specific gravimetric capacitance. This result reveals the importance of the porous structures in the energy storage. The AC

spheres of AC-4 have the largest fraction of micropores, and the AC spheres of AC-1 have the least fraction of micropores.
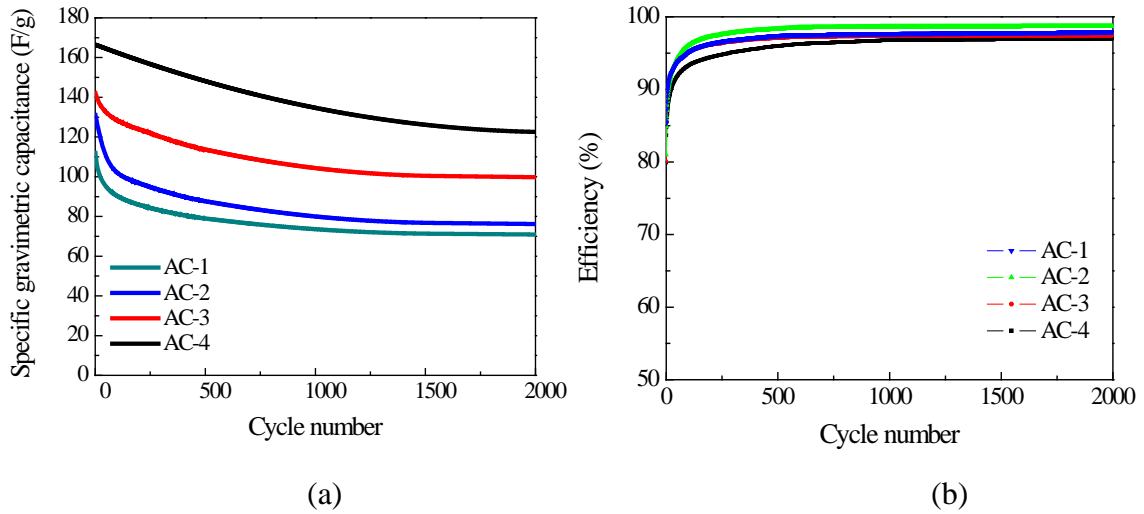
FIGURE 2.10 EFFECT OF CHARGING-DISCHARGING CYCLE ON CAPACITIVE BEHAVIOR OF THE SUPERCAPACITOR CELLS MADE FROM THE AC SPHERES OF AC-X (ELECTRIC CURRENT DENSITY: 0.5 A/G); (A) SGC RETENTION, AND (B) COULOMBIC EFFICIENCY

Figure 2.10b shows the variation of the Coulombic efficiency of the supercapacitor cells. The Coulombic efficiency increases with the increase of the cycle number, and approaches about 100%, indicating a highly reversible adsorption/desorption of K^+ ions on the surfaces of the pores of AC spheres and a prosperous cycle-life. Note that the supercapacitor cells made from the AC spheres of AC-2 has the highest Coulombic efficiency, while the supercapacitor cells made from the AC spheres of AC-4 has the lowest Coulombic efficiency. It is known that the Coulombic efficiency represents the cyclic stability of electrode materials. The results shown in Fig. 2.12b indicate good stability of the AC spheres of AC-xs.
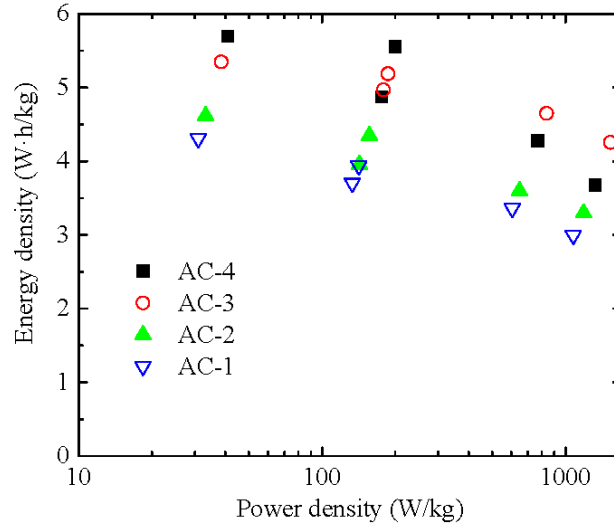
FIGURE 2.11 RAGONE PLOT OF THE SUPERCAPACITOR CELLS MADE FROM THE AC SPHERES OF AC-XS

The specific energy density and power density are calculated from the CV curves to further analyze the electrochemical performance of the supercapacitor cells made from the AC spheres of AC-x, using Eq. (2.4)

$$E(W \cdot h/kg) = \frac{C(\Delta V)^2}{8 \cdot 3.6} \quad \text{and} \quad P(\text{W/kg}) = 3600 \frac{\nu E}{\Delta V} \tag{2.4}$$

Figure 2.11 shows the Ragone plot of the supercapacitor cells made from the AC spheres of AC-x. It is evident that increasing the power density leads to the decrease of the energy density. Generally, both the energy density and power density of a supercapacitor depend on the characteristics of porous structures and the chemo physical properties of the electrode material. As discussed above, increasing the scan rate will cause the decrease of the capacitance due to the increase in the resistance to the ionic motion and the decrease of the accumulation of ions at the electrolyte/electrode interfaces. For the same porous structures, it is impossible to increase the energy density and the

50

power density simultaneously. Supercapacitors using electrode materials of optimal porous structures need to be explored, as revealed in Fig. 2.11 that the supercapacitor cells made from the AC spheres of AC-3 and AC-4 have approximately the largest energy density for the same power density. The more the micropores, the larger is the energy density at the same power density for the supercapacitors with aqueous electrolytes.

2.4   Conclusion

In summary, activated carbons of spherical shape were prepared with high fructose corn syrup via hydrothermal processing and physical self-activation. The effect of the activation time on the geometrical and porous characteristics was investigated. The size of the prepared AC spheres is about 0.8 μm which is independent of the activation time. Increasing the activation time leads to the increase of the fraction of micropores with the pore size of ~0.67 nm and also the increase of the surface area of micropores.

Using the AC spheres as electrode materials, supercapacitor cells of symmetrical type (two-electrodes) were prepared without any additives and binders. The electrochemical performance of the supercapacitor cells was characterized. The supercapacitor cells made from the AC spheres of AC-4 exhibited excellent electrochemical performance with a specific capacitance of 168 F/g at an electric current density of 0.2 A/g and an energy density of 4.2 W·h/kg at a power density of 1.5 kW/kg,

higher than the reported activated carbon-based supercapacitors with high specific

surface area, which is in the range of 0.8 ~1 kW/kg. Increasing the surface area and

fraction of micropores leads to the increase of the specific gravimetric capacitance.

CHAPTER 3.   SOYBEAN-RESIDUE-BASED ACS FOR EDLCS

3.1   Introduction

There are two important energy storage technologies; one is ion-based batteries, such as lithium-ion battery and sodium-ion battery, and the other is supercapacitors, such as electric double layer capacitors (EDLCs). Supercapacitors, which are mostly based on carbon materials, can be charged-discharged in a few seconds in contrast to ion-based batteries and can provide instant high power and long life. These advantages of supercapacitors over ion-based batteries have attracted great interests in the use of supercapacitors for energy storage in fields like the power of small appliances, high power and high pulse power of portable wireless communication, the starter power of internal-combustion engine and auxiliary power supply of photovoltaic products.

Biomass wastes are sustainable sources of activated carbons (ACs), which have been used in a variety of energy storage devices, including EDLCs. Soybean, a natural product with annual production over 300million tons worldwide [123], has been used in the production of soymilk and tofu for our daily life, leading to a large amount of biomass waste of soybean residue (SR). Currently, significant amount of SR is often discarded or burnt, which causes serious environmental concerns[124].Since SR is rich in cellulose (~50%) of dry weight[125, 126], it has been considered as the potential "top-down" precursor for the production of carbonaceous materials via hydrothermal carbonization (HTC) and chemical/physical activation processes.

There have been multiple studies in the application of EDLCs from the soybean-related product. Using HTC process at 200 ℃ and a KOH chemical activation in a temperature range of 600 ℃ to 800 ℃, Ferrero et al. [127] prepared nitrogen-doped porous carbon from defatted soybean – the by-product after the extraction of soybean oil. The porous carbon had an average pore size of ~0.7 nm. They used the prepared porous carbon as the electrodes of EDLCs, and obtained specific gravimetric capacitances of 250 F/g and 176 F/g at a current density of 0.2 A/g for electrolytes of H_2SO_4 and Li_2SO_4, respectively. Carbonizing soybean root, Guo et al. [128] produced char in nitrogen at 500 ℃ for 2 h, and used KOH to chemically activate the obtained char at 800 ℃ for 2 hrs. The activated carbon exhibited 3D-hierarchical porous structure with a large SSA of 2143 m^2/g. Using the 3D-hierarchical porous carbon as the electrodes in a symmetric two-electrode supercapacitor cell with 6 M KOH aqueous solution as the electrolyte, they obtained the largest specific gravimetric capacitance of 276 F/g at a current density of 0.5 A/g. Without pre-carbonization of soybean curd residue at low temperature, Ma et al. [129] carbonized soybean curd residue (SCR) at temperatures of 600, 700, 800, and 900 °C, and found that the carbonized SCR at 700 °C has the largest specific capacitance of 215 F/g at a current density of 0.5 A/g in a two-electrode cell with 0.5 mol/L Na_2SO_4aqueous solution as electrolyte. Using a two-step carbonization process with KOH in chemical activation, Xu et al. [130] synthesized hierarchical porous carbon with an interconnected microstructure from ground soybean. They studied the electrochemical characteristics of the synthesized hierarchical porous carbon in a three-electrode system

54

in 6 M KOH aqueous solution, and obtained a specific capacitance of 337.3 F/g at a current density of 1 A/g. It needs to point out that all of the works requires the wash of the carbonized materials in HCl to remove inorganic impurity in order to use the carbonized materials in supercapacitor cells.

Chemical activation is an effective way to prepare activated carbon with large specific surface area, while it always involves the use of a large amount of KOH which requires more difficult operation conditions, and an extra washing process with acid. It is of practical importance to explore a different approach to prepare ACs from biomass waste, such as soybean residue, without the use of KOH in activation. In this work, we develop a three-step synthesis of ACs from SR, which consists of a two-step HTC and a post physical activation. The synthesized ACs are used as the electrode material of EDLCs, and the electrochemical performance of the EDLCs is investigated in 6 M KOH aqueous solution.

3.2   Experimental detail and methodology

3.2.1   Experimental detail

Soybean residue was used as the precursor for HTC process. Cleaned fresh soybean was pre-soaked in water overnight, and blended to extract the soybean milk. The residue was collected and kept in refrigerator for the HTC processing. The HTC processing of SR was conducted in a 100 mL Teflon-lined autoclave. A mixture consisting of 40 g SR, 30

ml DI water and 1 ml 30 wt.% H_2SO_4 was well stirred and placed in an autoclave, in which the sulfuric acid was used as the catalyst for the carbonization of sugars from cellulose-rich biomass[95, 131]. The sealed autoclave was placed in a pre-heated oven at 200ºC with an attached thermocouple of K-type to monitor the temperature evolution. It took ~2 hrs for the Teflon-lined autoclave with the aqueous suspension to reach 200 ºC, and the temperature of the Teflon-lined autoclave with the aqueous suspension was maintained at 200 ±2 ºC for 20 hrs before cooling down to room temperature in air.

The hydrothermal product was collected, using Grade 2 Whatman filter papers (Sigma-Aldrich, St. Louis, MO). The mixture consisting of the collected hydrothermal product and DI water was sonicated for 1 h, and then filtrated through Grade 2 Whatman filter papers; and the remainder, which is referred to as HTC-1, was collected and dried in an oven at 90 ºC overnight.

Further HTC processing of the HTC-1 was performed in a sealed,100 mL Teflon-lined autoclave. 8 g HTC-1 was mixed with 30 ml DI water and 5 ml 6 M KOH aqueous solution in the autoclave, which was placed in an oven pre-heated to 200ºC. It took ~2 hrs for filled autoclave to reach 200 ºC, and the temperature of the autoclave was maintained at 200 ±2 ºC for 5 hrs before cooling down to room temperature in air. Following the same process as the collection of HTC-1, the HTC product made from the HTC-1 was collected, and referred to as HTC-2. The HTC-2was dried in an oven at 90 ºC overnight without any further treatment.

Physical activation of the HTC-2 was performed in a tube furnace (Lindberg/Blue M Mini-Mite Tube Furnace B2, Thermo Fisher Scientific) only with the flow of pure nitrogen in a temperature range from 450 ℃~ 850℃ for 3 hrs. Note that the physical activation did not use any gaseous agents or additives in contrast to most physical activations reported in the literature. The activated carbons were collected after the furnace was cooled down to room temperature in the environment of nitrogen, and then stored in an oven at 90 ℃ over night. The activated carbons (ACs) are denoted as AC-X with "X" representing the activation temperatures of 450, 550, 650, 750 and 850 ℃.
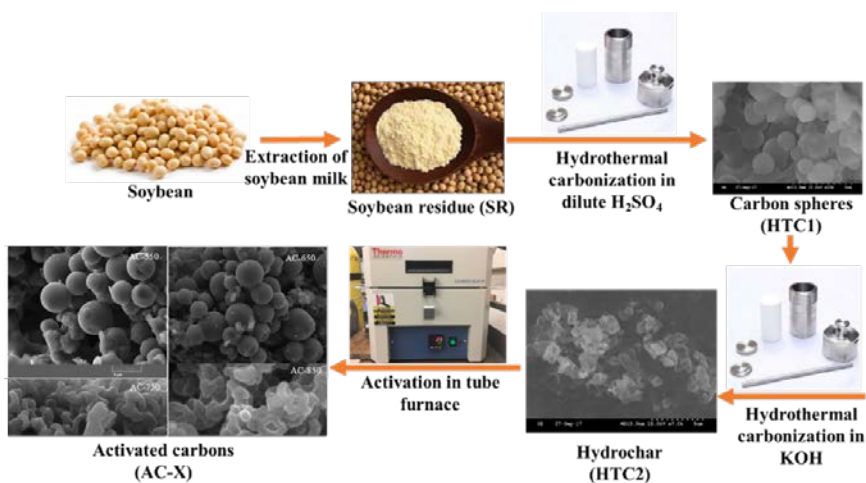
FIGURE 3.1 SCHEMATIC OF THE FLOW CHART FOR THE PREPARATION OF AC-X FROM SR

The microstructures of the prepared materials were characterized by X-ray diffraction (XRD)on an X-ray spectrometer (Bruker D8). The morphology and selected area electron diffraction (SAED) patterns of the activated carbons were examined on a Field Emission Scanning Electron Microscope (FESEM) (Tescan MIRA3 LMH) and a Transmission Electron Microscope (TEM) (JEOL 2100-F). The surface area and

distribution of pore sizes of the activated carbons were determined by nitrogen adsorption–desorption isotherms on an automated gas adsorption analyzer (Micromeritics surface characterization, Norcross, GA).

Electrodes for supercapacitor cells were made from the synthesized AC-X without the use of any binders or additives. The ACs taken out of the oven were ground first, and then placed back the oven at 90 °C for 30 min prior to the preparation of the electrodes. ACs of 1±0.1 mg were uniformly placed on the surfaces of two current collectors made from stainless steel, respectively, to form a thin disk of ~7 mm in diameter. The separator was 696 glass microfiber filter (VWR International, LLC.), and the electrolyte was 6 M KOH aqueous solution. The electrodes, separator and electrode were assembled in a Swagelok cell to form a symmetrical two-electrode system.

The electrochemical performance of the two-electrode system was characterized on a Princeton Applied Research PARSTAT MC potentiostat (AMETEK, Inc., PA). The cyclic voltammetry (CV) measurement was conducted in a voltage window of 0 to 1 V at a voltage scanning rate in the range of 2 to 100 mV/s. The galvanostatic charging and discharging (GC) measurement was performed at a current density in a range of 0.2 to 10 A/g in a voltage range of 0 to 1 V. The EIS measurement of the ACs-based electrodes was performed in a frequency range of 20 mHz to 1 MHz with a sinusoid alternative voltage of 10 mV.

3.2.2 Methodology

The specific gravimetric capacitance (SGC) of one single electrode in the unit of F/gfor the two-electrode system was calculated according to the following equation [121, 122]

$$SGC = \frac{\int I(V)\,dV}{m\mathrm{v}\Delta V} \tag{3.1}$$

from the CV curves, and

$$SGC = \frac{4i}{\Delta V / \Delta t} \tag{3.2}$$

from the GC curves, respectively. Here, I is the electric current intensity, m is the mass of single electrode, v is the scan rate, ΔV is the voltage window, i is the electric current density per unit mass, and $\Delta V/\Delta t$ is the slope of the discharging curve after the IR drop.

The specific energy density (E) and power density (P) of the two-electrode system were calculated from the CV curves as

$$E\left(\mathrm{W\cdot h/kg}\right) = \frac{(SGC)(\Delta V)^2}{8\cdot 3.6} \quad \text{and} \quad P(\mathrm{W/kg}) = 3600\frac{\mathrm{v}E}{\Delta V} \tag{3.3}$$

3.3 Results and discussion

3.3.1 Materials characterization

Fig. 3.2 shows XRD patterns of the synthesized ACs. It is evident that the ACs of AC-450 are present in amorphous phase with a broad peak around $2\theta=\sim23°$. Increasing the activation temperature from 450 °C to 850 °C led to the presence of three peaks around $2\theta = 21.7°$, 24º and 43.1º, whose intensities increase with the increase of the

activation temperature. The wide and weak peaks indicate that the ACs are disordered carbon with low crystallinity. For ACs of AC-850, the intensity at $2\theta = 21.7°$ becomes relatively weak, and the intensities at $2\theta = 24$ and $43.1°$ become relatively strong. Note that the peaks around $2\theta = 24$ and $43.1°$ correspond the (002) and (100) planes of graphitic carbon, which suggests that the heat treatment at high temperatures increases the crystallinity of ACs. The HTC processing and physical activation indeed converted the soybean residue to activated carbons with low crystallinity.
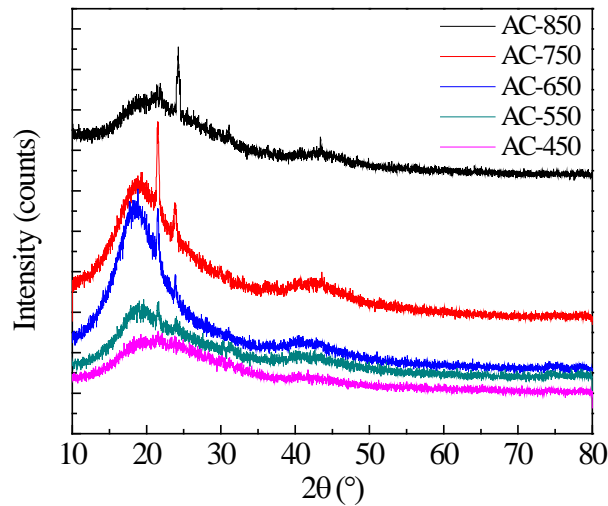
FIGURE 3.2 XRD PATTERNS OF ACS

Fig. 3.3 shows SEM images of the as-synthesizedHTC-1, HTC-2 and AC-X (450, 550, 650, 750 and 850). From Fig. 3.3 a and a_1, HTC-1 presents as sphere-like shape within two diameter ranges, where the larger one is from $4 – 7\mu m$ and the smaller one is around 1 μm. This indicates that the carbon microspheres can be obtained via hydrothermal processing of the soybean residue. As shown in Fig. $3.3b_1$, after hydrothermal processing of HTC-1 in the KOH aqueous solution, there exists the

morphologic change from spherical particles to irregular particles for carbon spheres with the small size, this can be explained by the saponification reaction of KOH and the oil and lipid materials. Water-soluble materials are generated from the saponification of the lipid substances, leading to the inhomogeneity and cohesion of the carbonaceous materials. In addition, due to the large ion size of K^+, the stronger attraction between K-O would cause the open of the original C-O bond, which further breaks the spherical structure. No obvious morphology change can be observed for carbon microspheres (Fig. 3b). From Fig. 3c-e, carbon microspheres can be obviously observed for AC-450, AC-500 and AC-650. The surface of carbon microspheres becomes more smooth and their sizes decrease with increasing the activation temperature from 450 ℃ to 650 ℃, which indicates that the physical activation at the temperature of 450 ℃-650 ℃ causes little morphologic change for carbon microspheres. In addition, the number of nanosphere increases with the increase of the activation temperature from 450 ℃ to 850 ℃. For AC-450 and AC-550, distorted carbon nanospheres can be found distributing in irregular particles in Fig. 3.3c$_1$ and Fig. 3.3d$_1$. While for AC-650, AC-770 and AC-850 (Fig. 3e-g), a mass of carbon nanospheres are formed, and adhere to each other severely. Such a result suggests that the physical activation causes the formation of nanospheres from irregular particles. Increasing the activation temperature to 750 ℃ and 850 ℃, the spherical structure of carbon microspheres is destroyed by excess-carbonization of AC-750 and AC-850 (Fig. 3f and g). The spherical carbon framework can be maintained for nanospheres for AC-750 and AC-850 (Fig. 3f1 and g1).
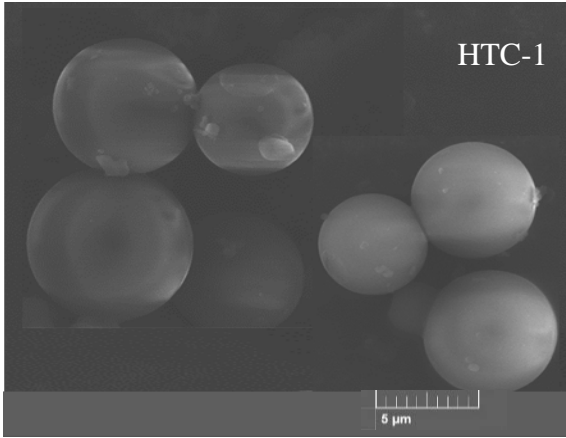
(a)
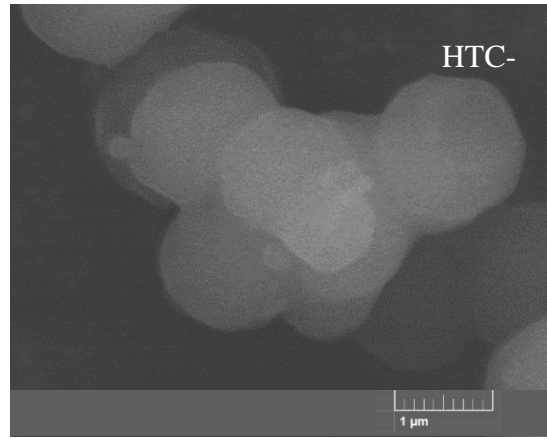
(a₁)
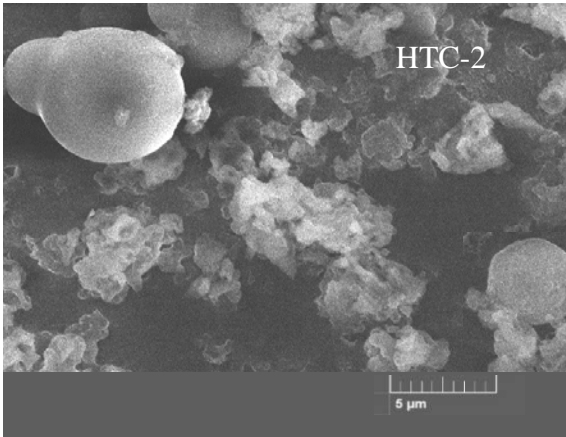
(b)
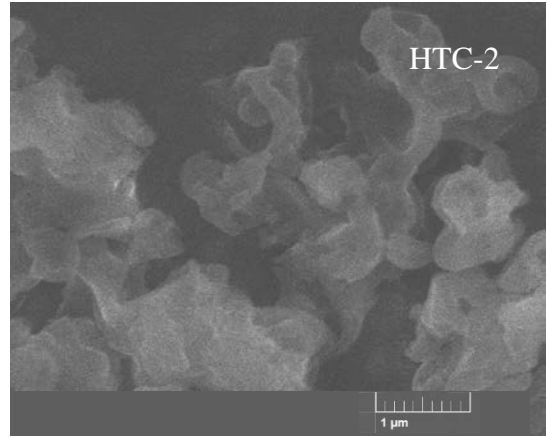
(b₁)
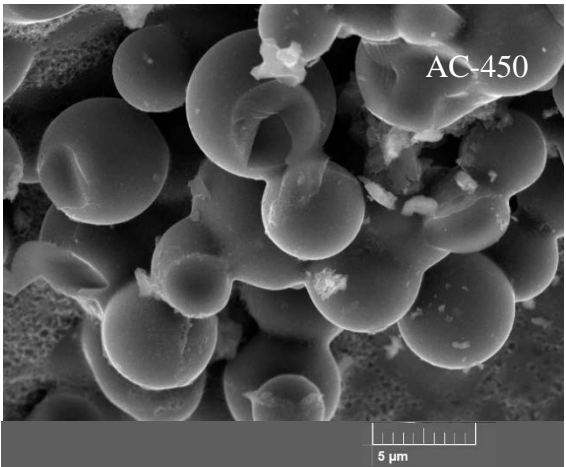
(c)
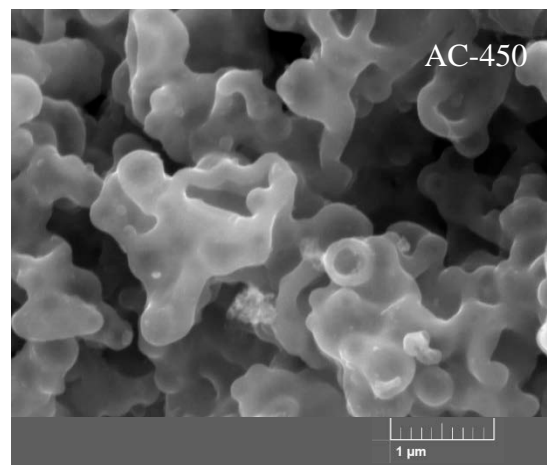
(c₁)

Figure 3.3 SEM images of HTC products and ACs: (a and a$_1$) HTC-1, (b and b$_1$) HTC-2, (c and c$_1$) AC-450 (HTC-2 activated at 450 ℃)
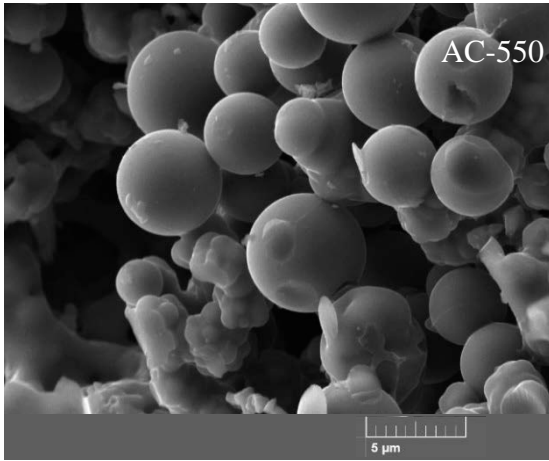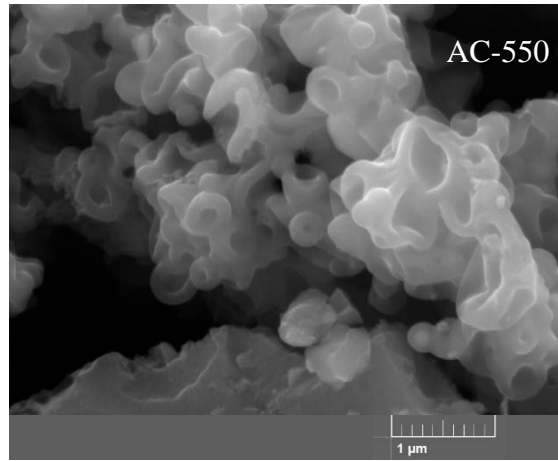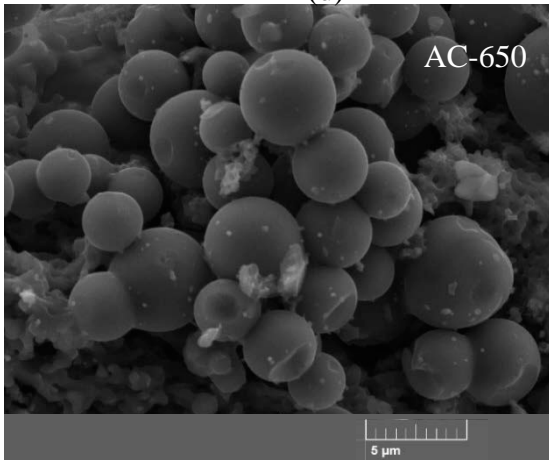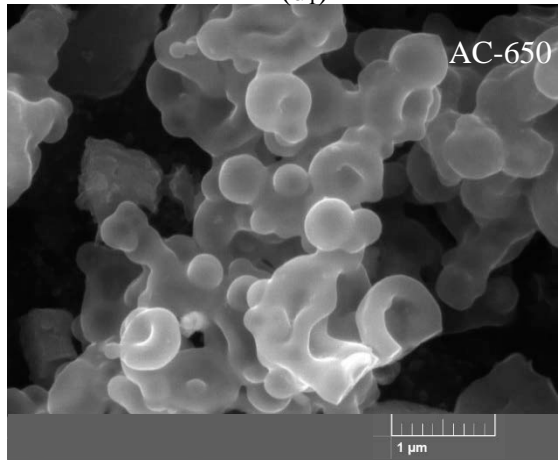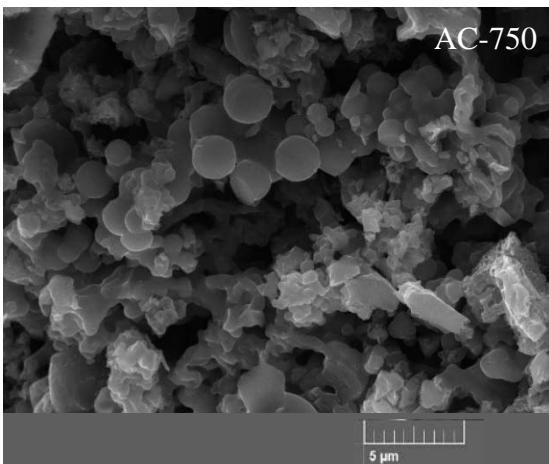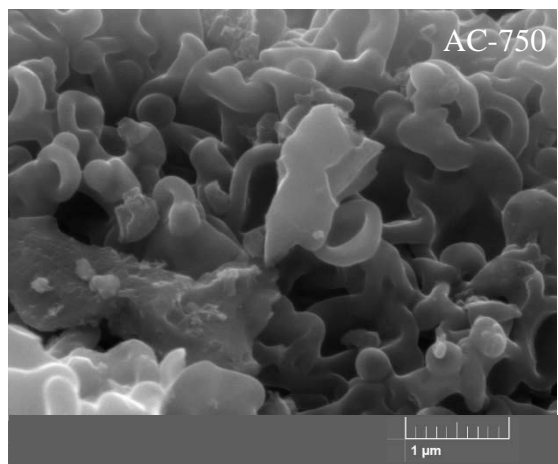
Figure 3.3 (continued) SEM images of HTC products and ACs: (d and d₁) AC-550 (HTC-2 activated at 550 ℃), (e and e₁) AC-650 (HTC-2 activated at 650 ℃), (f and f₁) AC-750 (HTC-2 activated at 750 ℃)

<p style="text-align:center">(g)   (g₁)</p>
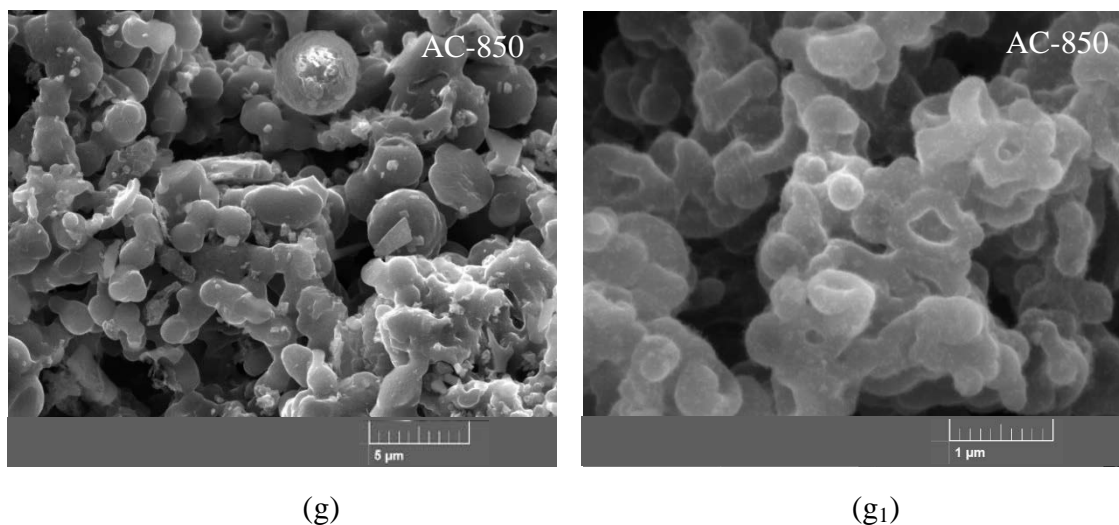
Figure 3.3 (continued) SEM images of HTC products and ACs: (g and g₁) AC-850 (HTC-2 activated at 850 ℃)

The microstructure of the AC-X (450, 550, 650, 750 and 850) is further investigated by TEM observation. Fig. 3.4 shows TEM images of carbon microspheres in Fig. 3.3(c-g). As observed in Fig. 3.4a-c, the carbon microspheres exhibit the solid structure for the AC-450, AC-550 and AC-650, indicating that activating HTC-2 at 450 °C to 650 °C did not cause any significant change to the microstructure of ACs. For AC-750 and AC-850, irregular carbon particles can be observed, in agreement with SEM results. The activation of HTC-2 at 850 °C led to the transition of amorphous carbon to crystalline carbon and the formation of laminate-like structure, as shown in the SADP pattern embedded in Fig. 3.4e-f,where the diffraction rings in Fig. 3.4f reveal the crystallinity of the AC-850, and the diameter of 3.281 1/nm corresponds to the (110) crystal plane of carbon (PDF 50-0926), in accordance with the XRD result.
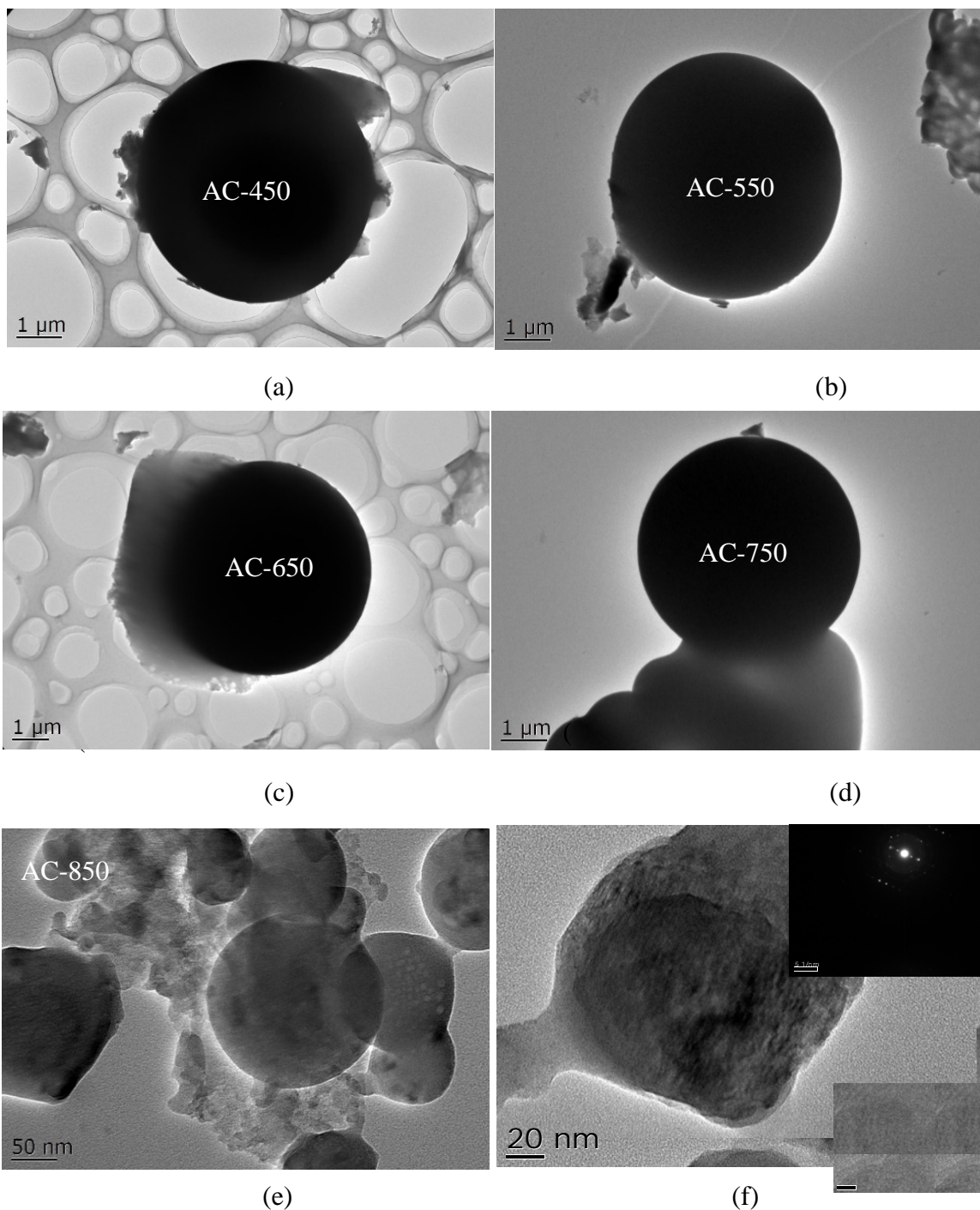
Figure 3.4 TEM images of AC-Xs: (a) AC-450(HTC-2 activated at 450 ℃), (b) AC-550 (HTC-2 activated at 550 ℃), (c) AC-650 (HTC-2 activated at 650 ℃), (d) AC-750 (HTC-2 activated at 750 ℃) and (e and f) AC-850 (HTC-2 activated at 850 ℃)

The TEM images of the carbon particles with small sizes in Fig. 3a and b and Fig.

$3c_1$-g_1 are shown in Fig. 3.5. The carbon particles with small sizes in the HTC-1 are

hollow spheres with wall thickness of ~70 nm, and small particles are found in the interior of spheres (Fig. 3.5a). For HTC-2 after hydrothermal processing, carbon nanospheres are found adhesive tightly to each other, along with other irregular shaped particles (Fig. 5b). After physical activation, hollow carbon nanospheres can be obtained in AC-X (550, 650, 750 and 850), and no obvious morphology changes are caused by the physical activation temperatures (Fig. 5c-e).

(a)　　　　　　　　　　　　　　　　　(b)

(c)　　　　　　　　　　　　　　　　　(d)
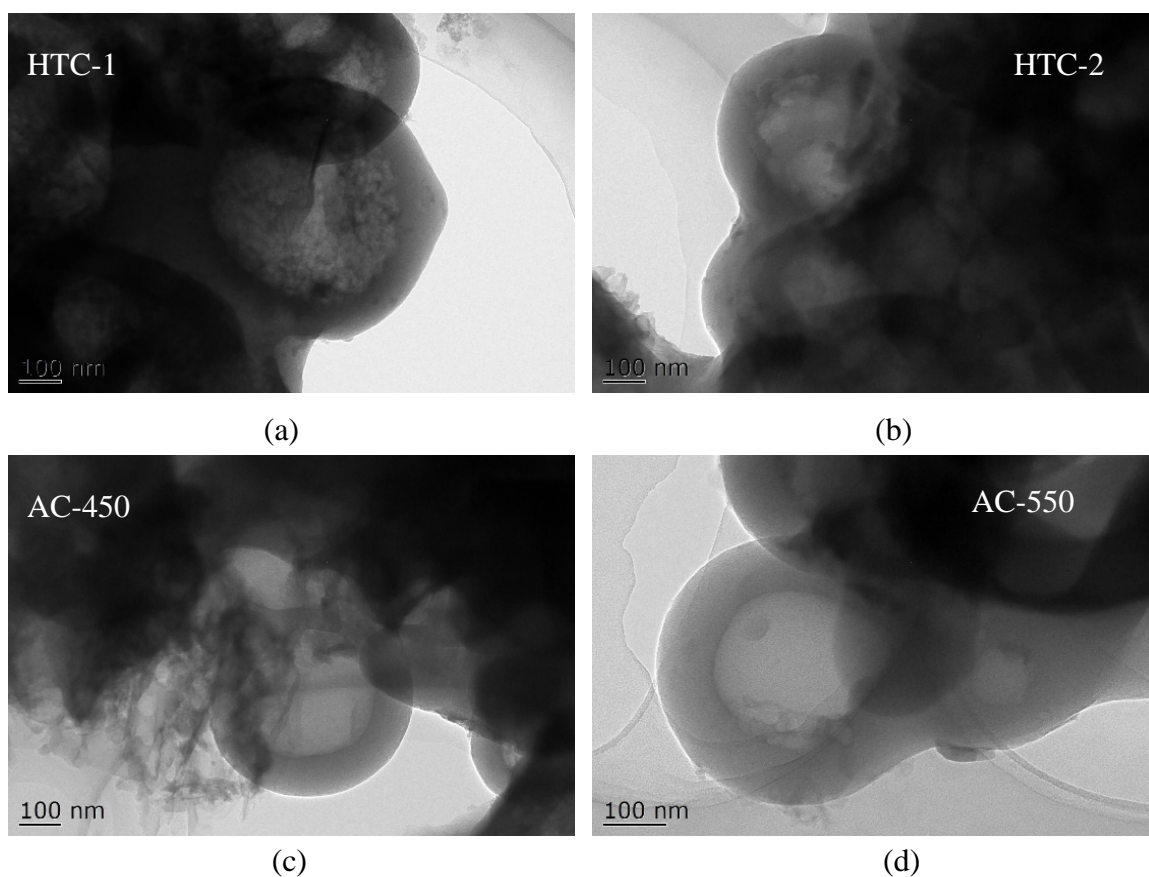
Figure 3.5 TEM of ACs: (a) HTC-1, (b) HTC-2, (c) AC-450 (HTC-2 activated at 450 ℃), (d) AC-550 (HTC-2 activated at 550 ℃)
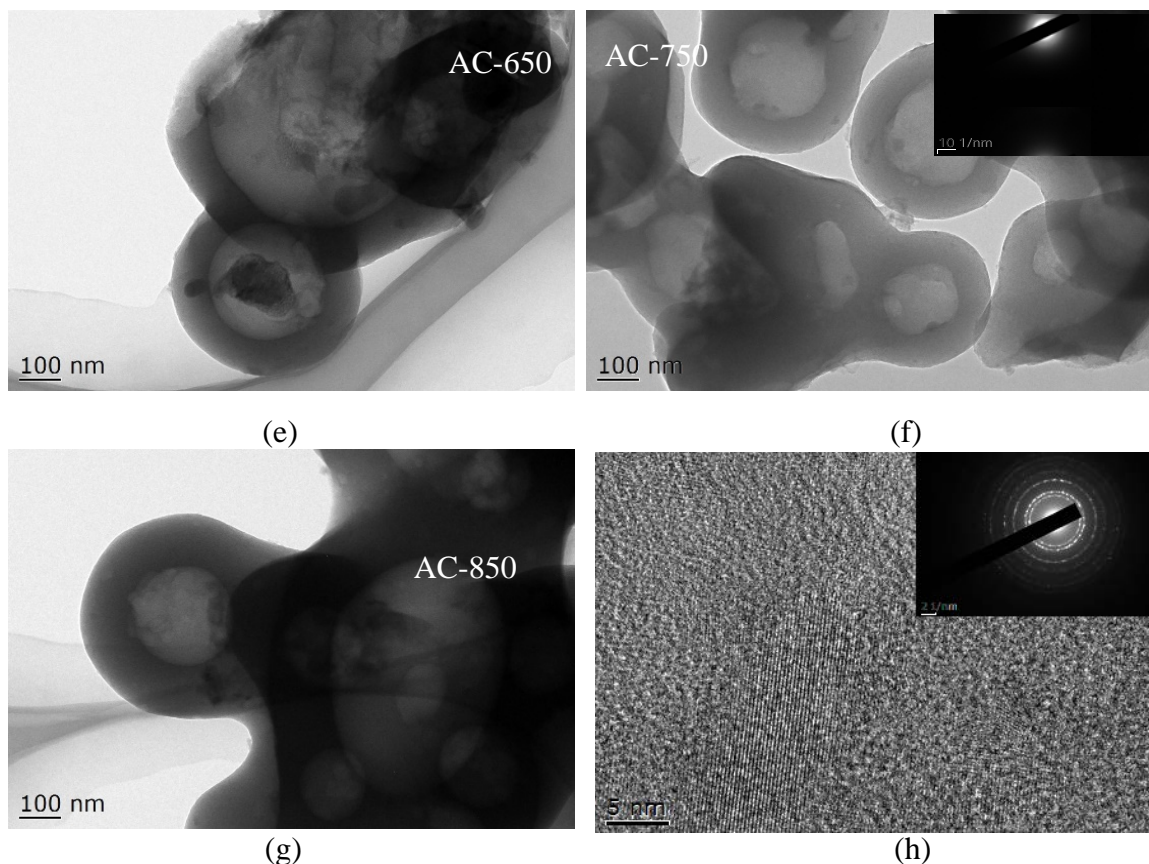
Figure 3.5 (Continued) TEM of ACs: (e) AC-650 (HTC-2 activated at 650 ℃), (f) AC-750 (HTC-2 activated at 750 ℃), (g and h) AC-850 (HTC-2 activated at 850 ℃)

The surface characteristics of the ACs were analyzed on a gas adsorption analyzer (Micromeritics surface characterization, Norcross, GA). Figure 3.6a shows the nitrogen adsorption-desorption isotherms of the ACs. The ACs of AC-450 to AC-650 exhibit a combination of Type II and Type III features [117]. There is only small amount of adsorption at low relative pressure, suggesting the weak interaction between nitrogen and the ACs of AC-450 to AC-650. The increase of the amount of adsorption with increasing relative pressure for the ACs of AC-450 to AC-650 reveals the lack of porous structures in the ACs of AC-450 to AC-650, which suggests that temperature less than 650℃ is too low to activate HTC-2. For ACs of AC-750 and AC-850, there is a rapid absorption of

nitrogen at low relative pressure, corresponding to the filling of micropores (Type I feature). The inflection point at the relative pressure of 0.8exhibits the characteristic of Type II feature, revealing the presence of macroporous structure, as supported by the hysteresis loops. It needs temperature larger than or equal to 750℃ in order to activate HTC-2. For ACs of AC-450 to AC-750, the hysteresis loops possess the characteristic of H3 type, i.e. there are slit holes from the aggregation of flaky particles. The hysteresis loop of the ACs of AC-850 exhibits the characteristic of H4 type, suggesting the presence of slit holes from lamellar structure. Such results are in accordance with the SEM and TEM observation.

(a)   (b)
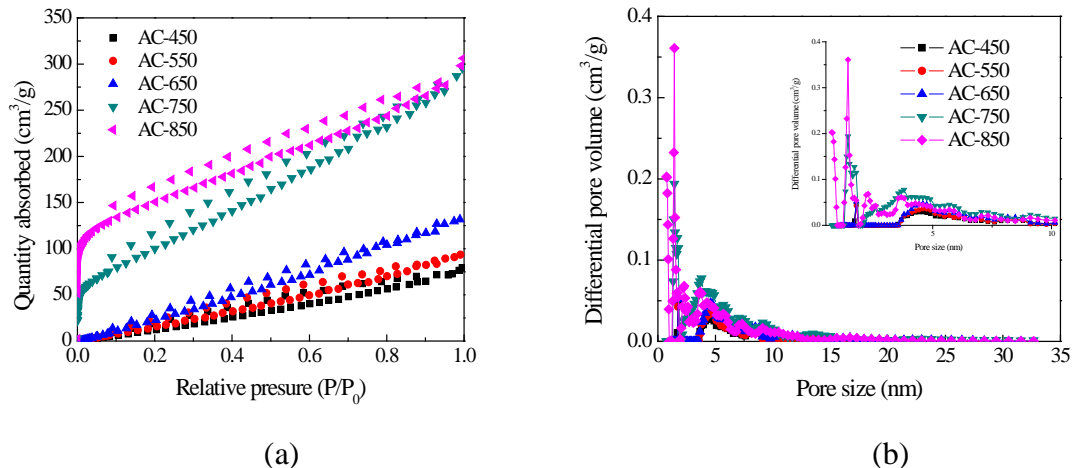
FIGURE 3.6 ADSORPTION BEHAVIOR OF ACS: (A) NITROGEN ADSORPTION-DESORPTION ISOTHERMS, AND (B) PORE SIZE DISTRIBUTION CALCULATED BY THE DFT (DENSITY FUNCTIONAL THEORY) METHOD

Figure 3.6b shows the distribution of the pore sizes of ACs of AC-X calculated from the adsorption-desorption isotherms by the method of density functional theory (DFT). The ACs of AC-450, AC-550 and AC-650 have similar distribution of pore sizes for

mesopores (2 nm < pore size < 50 nm). The activation of HTC-2 at temperature less than

or equal to 650 °C only leads to small amount of mesopores and no micropores (< 2 nm),

and the pores with the pore size of 4.5 nm have the largest differential pore volume.

There are micropores formed in the ACs of AC-750 and AC-850. It needs temperature

larger than or equal to 750 °C to physically activate the HTC-2 in order to produce

micropores in ACs.

Table 3.1 summarizes the surface characteristics of the ACs. Both the BET

(Brunauere-Emmette-Teller) [114] and DFT [115, 116] methods were used to calculate

the total surface area; which are referred to as S_{BET} and S_{DFT}, respectively. Note that the

BET method does not consider the contribution of micropores. The pore volumes of

micropores, mesopores and total pore volume are represented by V_{micro}, V_{meso} and V_{total},

respectively. There are $S_{DFT}= S_{meso} + S_{micro}$ and $V_{total}=V_{meso} + V_{micro} + V_{macro}$.

TABLE 3.1 SURFACE CHARACTERISTICS OF THE ACs

T (°C)	Average pore size (nm)	S_{BET} (m^2/g)	S_{DFT} (m^2/g)	V_{total} (cm^3/g)	S_{micro} (m^2/g) (area%)	S_{meso} (m^2/g) (area%)	V_{micro} (cm^3/g) (vol.%)	V_{meso} (cm^3/g) (vol.%)
450	236	2	73	0.12	5 (7)	68 (93)	0.004 (3)	0.11 (92)
550	124	5	84	0.14	4 (5)	80 (95)	0.004 (3)	0.13 (93)
650	36	23	116	0.2	5 (4)	111 (96)	0.004 (2)	0.19 (95)
750	6.3	291	341	0.46	83 (24)	258 (76)	0.06 (13)	0.36 (78)
850	3.7	517	577	0.47	365 (63)	212 (37)	0.16 (58)	0.26 (42)

According to Fig. 3.6 and Table 3.1, we can conclude that the porous structures of the ACs are dependent on activation temperature. Increasing the activation temperature from 450 °C to 850 °C results in the increase of the total surface area of S_{DFT} from $73m^2/g$ to $517 \, m^2/g$.

3.3.2   Electrochemical performance of ACs

Figure 3.7 depicts the Nyquist plot of ACs in the frequency range of 20 mHz to 1 MHz. A single semicircle is present for all the ACs in the range of mid-high frequency, displaying the resistive characteristic for the charge transfer between electrolyte and the ACs. An enlarged view of the high frequency region was inserted in the top right corner. All AC-Xs had a low value of R_s. With the increase of activation temperatures from 450 °C to 850 °C, R_s got little decreased from 0.16 ohm to 0.09 ohm, while the value of R_{ct} differed largely from several hundred ohms to 3.4 ohms, which is in accord with the porous characteristic of the ACs, indicating a large improvement of the electrical conductivity and accessibility of the electrolyte ions. The diffusion impedance in medium frequency region is called Warburg impedance, indicating the efficiency of ion transfer in the interface of electrode and electrolyte, the shorter of this transition section, the sooner of the transition from resistive behavior to capacitive behavior, suggesting faster electron transfer and better capacitive properties. From Fig. 3.7, it can be observed that higher activated temperature with more developed microporous structure facilitates the capacitance performance.
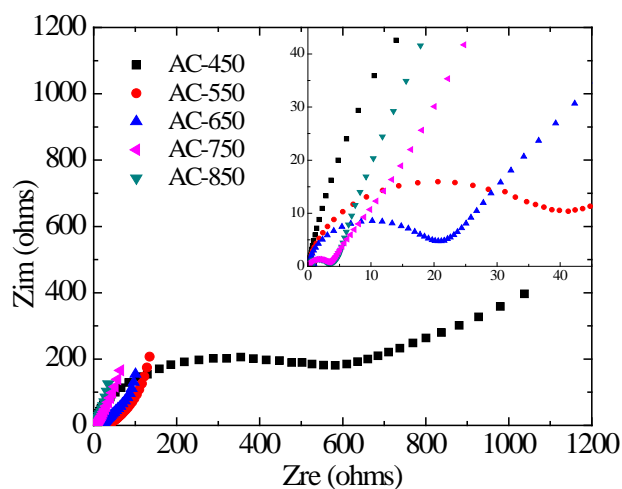
FIGURE 3.7 NYQUIST PLOT OF ACS

Figure 3.8a and 3.8b show I-V curves of the tenth cycle for the supercapacitor cells with ACs as electrodes. According to Fig. 3.8a, the supercapacitor cells with ACs of AC-450 exhibit poor capacitive behavior, and can only store limited amount of charge. Such a result is due to that there are limited SSA and the lack of micropores in the ACs of AC-450. The I-V curves of the ACs of AC550 to AC-850 are present in a quasi-rectangular shape, suggesting the presence of capacitive behavior. The enclosed area, which is proportional to the capacitance, increases with the increase of the activation temperature, revealing the importance of the activation temperature in controlling the charge storage in ACs. The deviation of the I-V curves from the ideal-rectangular shape at high voltage is likely due to the polarization at the interface between electrolyte and the ACs and the spatial confinement to the accumulation of ions inside the pores of ACs. The effect of the scan rate on the I-V characteristics of the ACs of AC-850 is shown in Fig. 3.8b for the scan rate up to 100 mV/s. It is evident that the

71

I-V curves are present in a quasi-rectangular shape, independent of the scan rate. The enclosed area increases with the increase of the scan rate, and there are more ions accumulated in the ACs.

(a)

(b)

(c)
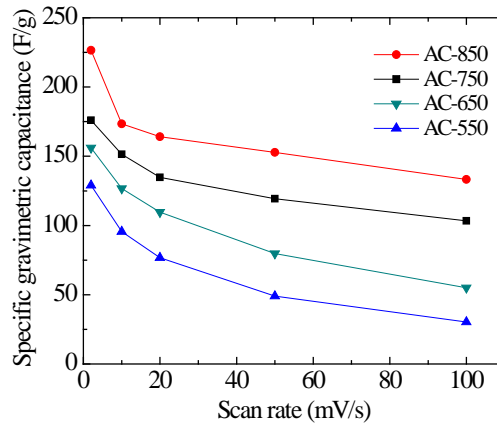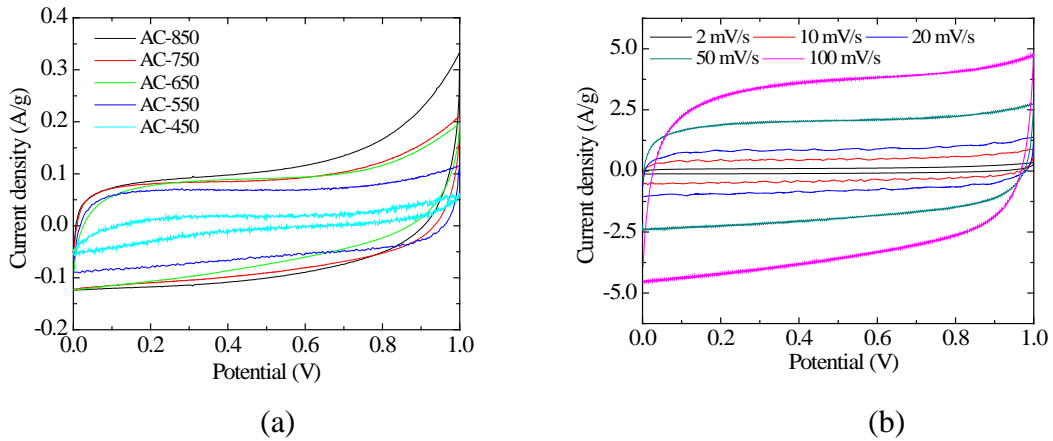
FIGURE 3.8 (A) I-V CURVES OF SUPERCAPACITOR CELLS WITH ACS AS ELECTRODES AT A SCAN RATE OF 2 MV/S IN 6 M KOH AQUEOUS SOLUTION, (B) I-V CURVES OF SUPERCAPACITOR CELLS WITH ACS OF AC-850 AS ELECTRODES AT DIFFERENT SCAN RATES, AND (C) SPECIFIC GRAVIMETRIC CAPACITANCE OF SUPERCAPACITOR CELLS WITH ACS AS ELECTRODES AT DIFFERENT SCAN RATES

From the I-V curves and Eq. 3.1, we calculate the specific gravimetric capacitance. Figure 3.8c shows the dependence of the specific gravimetric capacitance on the scan rate

for all the ACs. In general, the specific gravimetric capacitance decreases with the increase of the scan rate likely due to the increase of the electric driving force on ions. Even though more ions accumulate in the ACs under a large scan rate, the ions have less time to migrate into ACs. The average specific gravimetric capacitances of the supercapacitors at the tenth cycle at the scan rate of 2 mV/s are 129, 156, 176 and 227 F/g, respectively, for the ACs of AC-550, AC-650, AC-750 and AC-850. According to Fig. 3.7c, the specific gravimetric capacitance decreases with the decrease of the activation temperature for the same scan rate, which reveals the importance of the porous structures in the charge storage. The largest decrease of the capacitance occurs at the scan rate of 10 mV/s, and the corresponding capacitances are 96, 127, 152 and 174 F/g, respectively. Note that the supercapacitors made from the ACs of AC-450 has very small specific gravimetric capacitance, and the corresponding results are not included in Fig. 3.8c.

Figure 3.9 depicts GC curves of the supercapacitors made from ACs in the tenth cycle at a current density of 0.2 A/g. All the GC curves are present in a triangle-like shape with reasonable symmetry, suggesting that all the supercapacitor cells made from the AC spheres of AC-x possess capacitive behavior. Note that the supercapacitors made from the ACs of AC-450 have no capacitive behavior, and no results are included in Fig. 3.9.

(a)

(b)

(c)
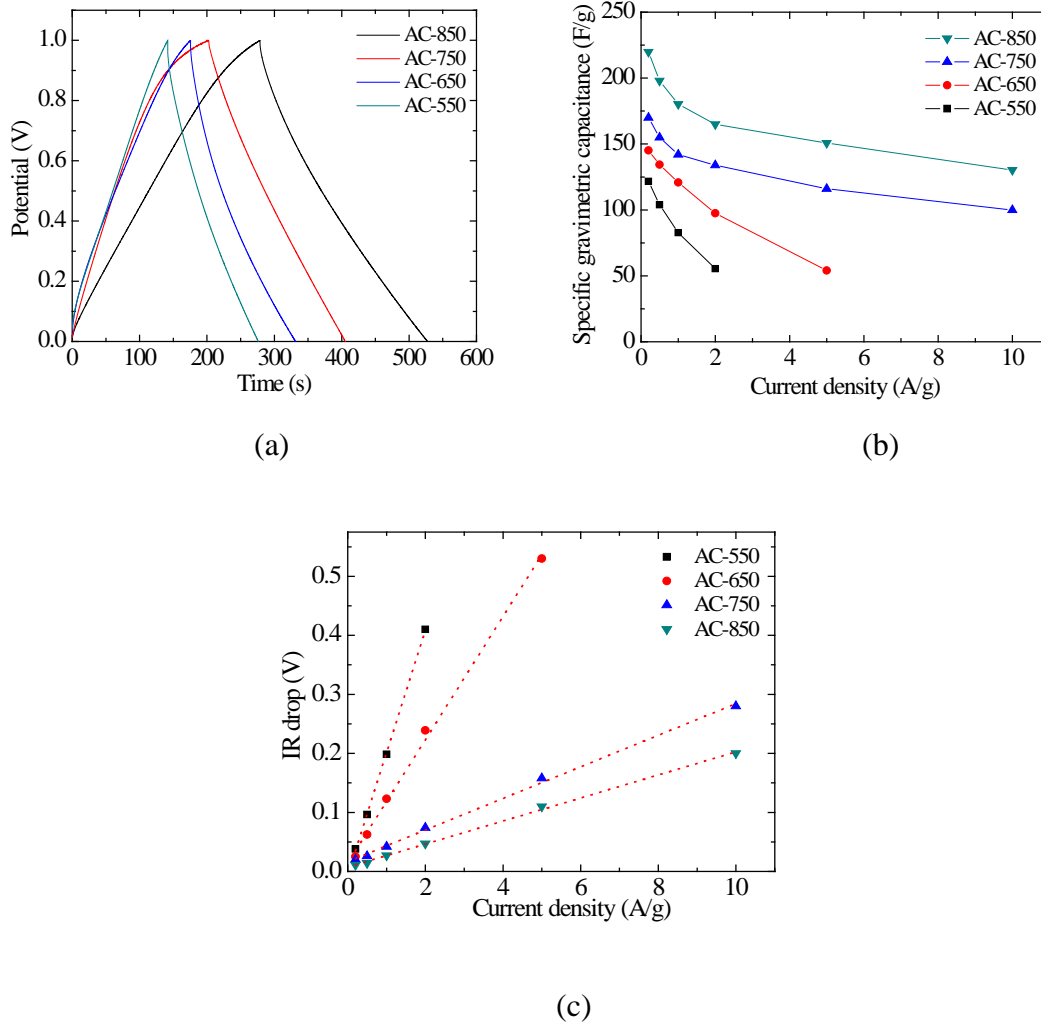
FIGURE 3.9 (A) GC CURVES OF SUPERCAPACITORS MADE FROM ACS IN THE TENTH CYCLE AT A CURRENT DENSITY OF 0.2 A/G, (B) SPECIFIC GRAVIMETRIC CAPACITANCE OF SUPERCAPACITOR CELLS W45EITH ACS AS ELECTRODES AT DIFFERENT CURRENT DENSITIES, AND (C) IR DROP OF SUPERCAPACITOR CELLS WITH ACS AS ELECTRODES AT DIFFERENT CURRENT DENSITIES

Figure 3.9 depicts GC curves of the supercapacitors made from ACs in the tenth cycle at a current density of 0.2 A/g. All the GC curves are present in a triangle-like shape with reasonable symmetry, suggesting that all the supercapacitor cells made from the AC spheres of AC-x possess capacitive behavior. Note that the supercapacitors made

from the ACs of AC-450 have no capacitive behavior, and no results are included in Fig. 3.9.

Using the GC curves and Eq. 3.2, the specific gravimetric capacitance of supercapacitor cells with ACs as electrodes were calculated. Fig. 3.9b shows the variation of the specific gravimetric capacitance of supercapacitor cells with ACs as electrodes with the current density. For the same current density, the supercapacitor cells with the ACs of AC-850 have the largest specific gravimetric capacitance, and the supercapacitor cells with the ACs of AC-550 have the smallest specific gravimetric capacitance. The better electrochemical performance of the supercapacitor cells with the ACs of AC-850 than those with the ACs of AC-750 confirms the important role of micropores over mesopores in ionic transport for the capacity retention in aqueous system[132]. For the supercapacitor cells with the same ACs, the specific gravimetric capacitance decreases with the increase of the current density. Such behavior is due to the energy dissipation associated with the resistive characteristics of the supercapacitor cells and the large driving force. In general, ions under the action of electric current experience local electric force, which is proportional to local current density. Increasing the current density for galvanostatic operation leads to the increase in the driving force, which reduces to the amount of ions accumulated in ACs and the storage of energy.

It has been suggested that the ideal pore size of a porous structure for the accumulation of ions would be the one matching the size of solvated ions, namely, the effective ions [133], since the electro-adsorption of ions cannot occur at smaller pores.

Also, the impinged ions in compact layers would reduce the usable surface area for electro-adsorption for pore sizes slightly less than two-fold of the size of effective ions [132, 134], and significantly larger pores have smaller SSA. For the electrolyte used in this work, the effective ions are hydrated K^+ with ionic size of ~0.66 nm, which is compatible with the micropore sizes developed in the ACs of AC-850.

The energy dissipation associated with the discharging of a supercapacitor cell can be represented by the IR drop shown in the GC curves. Figure 3.8c shows the variation of the IR drop with the current density for the supercapacitor cells made from the ACs. The IR drop increases linearly with the increase of the current density for all the supercapacitor cells made from the same ACs. The average differential ratios of the IR drop with respect to the current density are 0.21, 0.11, 0.03 and 0.02, for the supercapacitor cells made from the ACs of AC-550, AC-650, AC-750 and AC-850, respectively. There exists effect of porous structures on the IR drop, which suggests that the resistance to ionic migration determines the IR drop (energy dissipation) and is current-dependent.
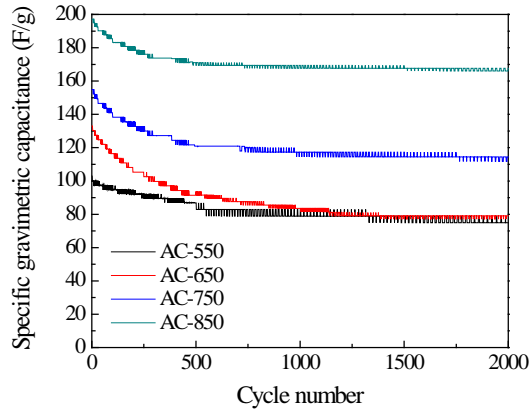
FIGURE 3.10 CYCLE STABILITY OF SUPERCAPACITOR CELLS MADE FROM ACs (CURRENT DENSITY: 0.5 A/G)

The cycle stability of the supercapacitor cells made from ACs were examined at a current density of 0.5 A/g. Figure 3.10 shows the variation of the specific gravimetric capacitance of the supercapacitor cells made from ACs with the cycle number. The capacity retentions of the supercapacitor cells made from the ACs are74.9%, 59.5%, 73.9% and 85.2%, respectively, for AC-550, AC-650, AC-750 and AC-850. Such results suggest that the capacity retentions of the supercapacitor cells made from the ACs of AC-850 have the best cycle stability.
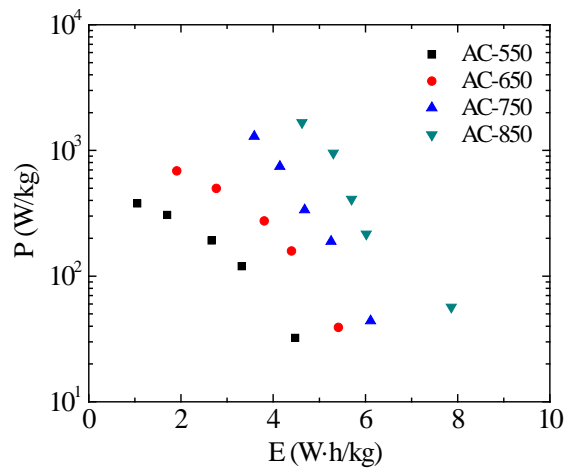
FIGURE 3.11 RAGONE PLOT OF SUPERCAPACITOR CELLS MADE FROM ACs

Figure 3.11 shows the relative relationship between the specific energy density and power density. The supercapacitor cells made from the ACs of AC-850 possess the highest energy density of7.9 W h/kg at a power density of 56.6 W/kg and the highest power density of1.7kW/kg at an energy density of 4.6 W/kg. The specific power density decreases with the increase of the specific energy density, as expected. Compromise must be made between the specific energy density and the specific power density to optimize the efficiency and performance of supercapacitors due to the dependence of ionic migration and the accumulation of ions in ACs on the driving force on ions.

3.4   Conclusion

We have used two-step hydrothermal processing and physical activation to prepare ACs from soybean residues. The experimental results reveal the importance of the activation temperature in controlling the evolution of porous structures, which determines the electrochemical behavior of the supercapacitor cells made from the ACs. The following summarizes the main results.

The two-step hydrothermal processing of soybean residues lays a foundation of the success of the physical activation, which largely reduce the use of KOH and leads to the formation of hollow-spherical carbon spheres or laminate-like porous structure at high activation temperatures.

The activation temperature needs to be larger than or equal to 550 ºC in order to activate the carbonized materials from the soybean residues. Increasing the activation temperature from550 ºC to 750 ºC does not cause any significant change in the morphologies of the activated carbon from those produced from the two-step hydrothermal processing, and there is a slight decrease in the size of the activated carbon in comparison with the corresponding hydrothermal products. However, a transition of amorphous carbon to crystalline carbon was found for the activation at 850ºC.

The symmetrical two-electrode supercapacitor cells made from the ACs exhibit relatively good capacitive behavior, which depends on the porous structures of the ACs controlled by the activation temperature. The supercapacitor cells with the ACs of AC-850 exhibit the best capacitive characteristics, and possess a specific gravimetric capacitance of 227 F/g at the scan rate of 2 mV/s, an energy density of 56.6 W·h/kg at a power density of 7.9 kW/kg, and a power density of1.7kW/kg at an energy density of 4.6 W/kg.

CHAPTER 4.   COMPRESSION TEST OF HFCS-BASED ACS

4.1   Introduction

Compression is of practical importance in the preparation of electrode materials for SCs, and has a direct effect on the physical behavior of the electrode and electrochemical performance of SCs, including density, electrical conductivity and structures of materials, such as microstructure and porosity [135]. There are studies focusing on compressible SCs for mechanical stretchable power source devices, which mainly use graphene, carbon nanotubes and conducting polymer to form aerogel or foam supercapacitors [136-139]. This type of SCs is present in a three dimensional structure interconnected with open pores that can undergo deformation with more than 40% compressive strain, which is recoverable after hundreds of compression and release cycles. It would be of great importance to evaluate the structural durability of this type of SCs under mechanical loading.

The structural durability of SCs is dependent on structural evolution and load bearing of electrode materials. It has been reported all-solid-state supercapacitors, which are made from porous carbon materials such as foam-like graphene with conducting or pseudocapacitive additives [140], can retain good and stable capacitance after multi-mechanical tests like tensile, shear and compression testing [141]. The study has been on the retention capacity after compressive deformation and their bearing tolerance

of the integral supercapacitors under various compression situations [142]. However, none of them has investigated the structural integrity of electrode materials under mechanical loading, which plays an important role in determining the electrochemical performance of SCs.

This chapter is focused on the mechanical response of porous carbons under compression in both dry and wet conditions. The material used in this work is the HTC-based ACs derived from the HFCS, as described in Chapter 2. The compression tests were performed on a Micro-Combi Tester (CSM Instruments, Peseux, Switzerland), using a cylinder punch (D= 6.33 mm) made from stainless steel.

4.2   Experimental details

The activated carbons of AC-4 from HFCS55 were used as the material for the study. The preparation method was described in detail in Chapter 2. Briefly, ~10.4 vol.% HFCS55 and ~89.6 vol.% DI water were mixed in a 100 ml autoclave for hydrothermal carbonization treatment (HTC) at 220±2 ℃ for an hour. After cooling, sonication, filtering, washing and drying, the dried product was placed in a tube furnace with a passage of nitrogen and heated to 850 ℃ for 4 hours. The product after the heat treatment was collected and stored at 100 ℃ for further use.

Polytetrafluoroethylene (PTFE) powder (Alfa Aesar, MA, USA) was used as the binder for the fabrication of disks from the activated carbons of AC-4 for the

compression tests. 95 wt.% AC-4 and pre-ground 5 wt.% PTFE were weighed and mixed together. The mixing took about one hour with mechanical grinding in an agate mortar. A stainless steel cylinder mounting mold was used to make disks of ~8 mm in diameter. 0.202 g fully-mixed mixture was weighed for three times for accuracy and placed on a mold carefully to ensure a relatively uniform distribution. The mounted mold with the mixture was placed in an oven at 80 °C for 40 min to soften the binder for better binding. A hydraulic machinery (Carver model #3912, IN, USA) was used to compress the disks at a load of 0.2 metric ton for 60 s, corresponding to a pressure of ~40 MPa. The prepared disks were around 4 mm in thickness and were placed on the stage of the Micro-Combi Tester for compression tests.

The compression test was performed on a Micro-Combi Tester (CSM Instruments, Peseux, Switzerland). The load-control mode was used with the same loading and unloading rates of 200 mN/min. an intermediate holding phase was set between the loading phase and the unloading phase, at which the load remained the same as the maximum load. A pre-load of 20 mN was applied to the punch prior to the compression test to ensure an intimate contact between the punch and the surface of sample to avoid the impact effect. The minimum compression load was 100 mN, and the maximum compression load was 900 mN. A linear increment of loading was set for five cycles, which was unloaded to 20 mN and followed by the new cycle until the last one ended to zero. Both the loading and unloading curves were recorded. The slopes of the unloading curves at the onset of unloading were used to calculate the stiffness of the disks. Each

experiment was repeated for ten times, all the graphs were plotted using the mean value, and the error bar was added based on the standard deviation. Each disk was used for one time only.

4.3 Results

4.3.1 Dry disks

Figure 4.1a shows the load-displacement curves of the compression tests of the dry disks with different holding times in the intermediate stage at 300 mN. In general, the load-displacement curves exhibit reasonable repeatability. There is a linear segment at the beginning of the loading period. Figure 4.1b shows the load-displacement curves of the compression tests of dry disks for different forces at holding time of 8s. It can be seen that the linear region for next loading period is larger than previous ones.

(a)   (b)
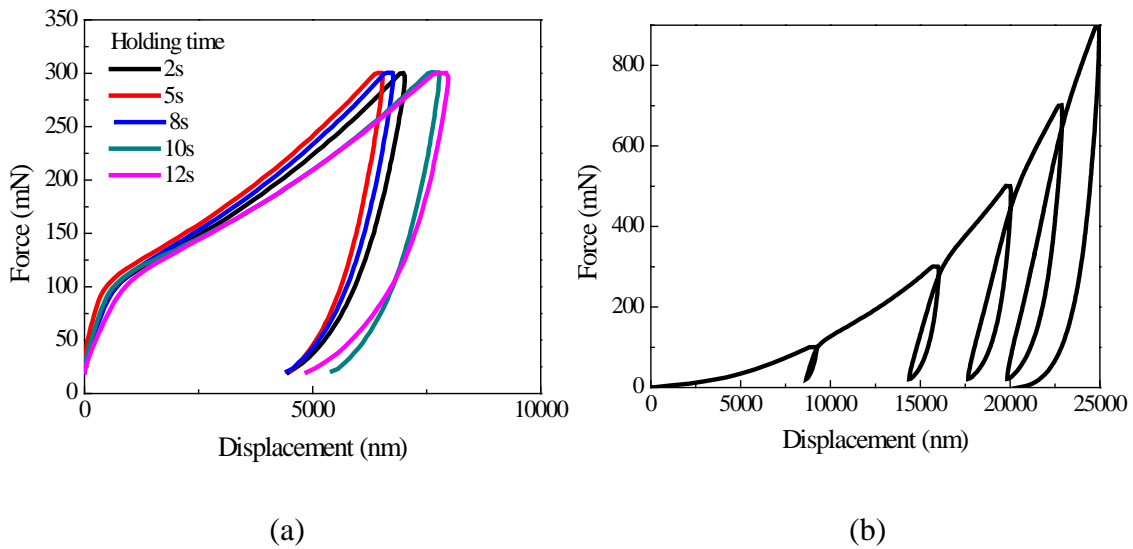
FIGURE 4.1 (A) LOAD-DISPLACEMENT CURVES OF THE COMPRESSION TESTS OF DRY DISKS FOR DIFFERENT HOLDING TIME AT 300 mN, AND (B) LOAD-DISPLACEMENT CURVES OF THE COMPRESSION TESTS OF DRY DISKS FOR DIFFERENT FORCES AT HOLDING TIME OF 8S
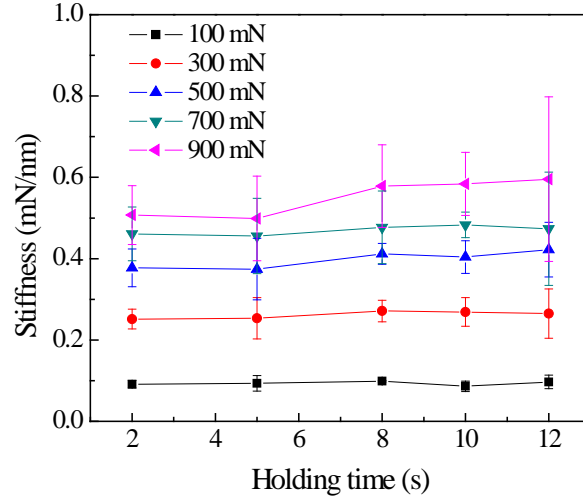
FIGURE 4.2 VARIATION OF STIFFNESS WITH HOLDING TIME FOR DRY DISKS

From the load-displacement curves, the stiffness of the disks, *S*, is calculated from the slope of the unloading curve at the onset of the unloading phase as

$$S = \frac{dP}{dh} \qquad (4.1)$$

where *P* is the compression load, and *h* is the displacement of the punch. Figure 4.2 shows the variation of the stiffness with the holding time. It is evident that the stiffness increases with the increase of the holding time, and reaches a plateau for the holding time larger than or equal to 8s, i.e. the stiffness becomes independent of the holding time larger than or equal to 8s. Thus, the results reported below are for the compression tests with the holding time of 8s.
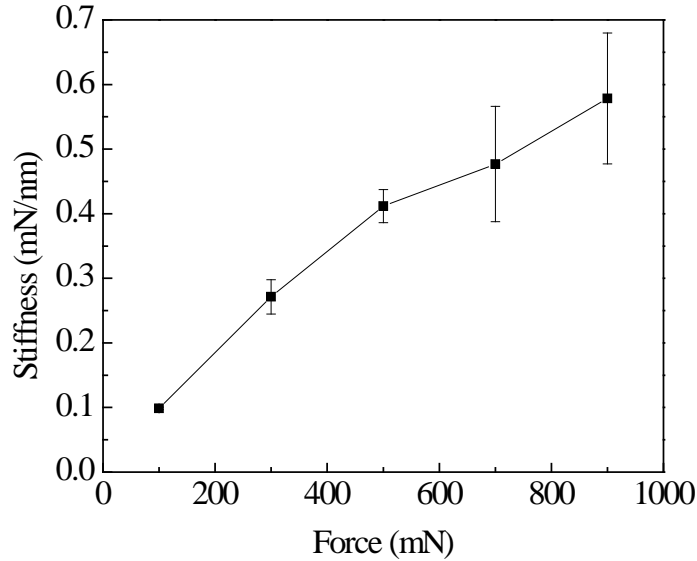
FIGURE 4.3 VARIATION OF THE STIFFNESS WITH MAXIMUM COMPRESSION LOAD FOR DRY DISKS

Figure 4.3 shows the variation of the stiffness with the maximum compression load. It is evident that the stiffness of the dry disks increases with the increase of the maximum compression load. Such behavior is due to the consolidation of the activated carbons and binder in the disks. Increasing the maximum compression load increase the packing density and the elastic modulus of the disks.

In order to simulate the solvation condition in SCs, the disks were immersed in purified water for five minutes with the compressed surface up and remained in water during the compression tests. This was achieved by using a special-made PTFE stage with a stainless steel holder which has a hole of an inner diameter of 8 mm.

4.3.2   Wet disks
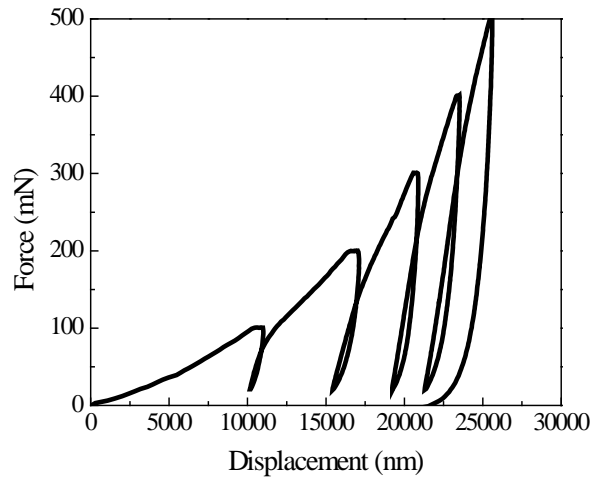
FIGURE 4.4 LOAD-DISPLACEMENT CURVES OF THE COMPRESSION TESTS OF WET DISKS

Figure 4.4 shows the load-displacement curves of the compression tests of the wet disks with different holding times in the intermediate stage. In general, the load-displacement curves also exhibit reasonable repeatability. Similarly, there is a linear region at the beginning of the loading segment, but the linear region is smaller than the corresponding dry one. From the load-displacement curves, the stiffness of the disks, *S*, is also calculated from the slope of the unloading curve at the onset of the unloading phase.

Figure 4.5 shows the variation of the stiffness with the maximum compression load. It is evident that the stiffness of the dry disks increases with the increase of the maximum compression load. Such behavior is again due to the consolidation of the activated carbons and binder in the disks. Increasing the maximum compression load increase the packing density and the elastic modulus of the disks.
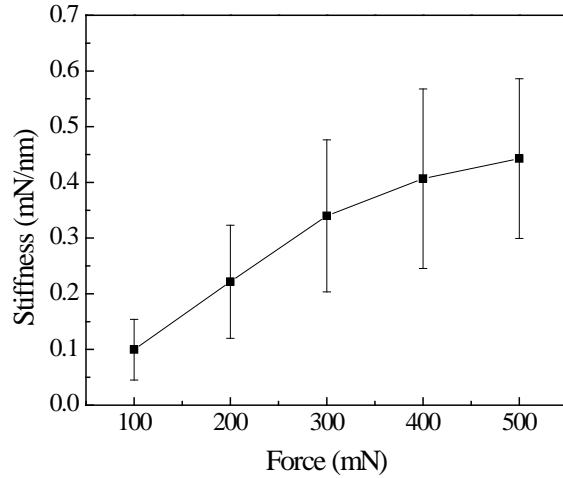
FIGURE 4.5 VARIATION OF THE STIFFNESS WITH MAXIMUM COMPRESSION LOAD FOR WET DISKS

For comparison, the variation of the stiffness with the maximum compression load for both the dry and wet disks is plotted in Fig. 4.6. It is evident that the wet disks have higher stiffness than that of the dry disks at the same maximum load. Such a difference reveals the effect of water on the motion/rotation of carbon particles, leading to different consolidation behavior.
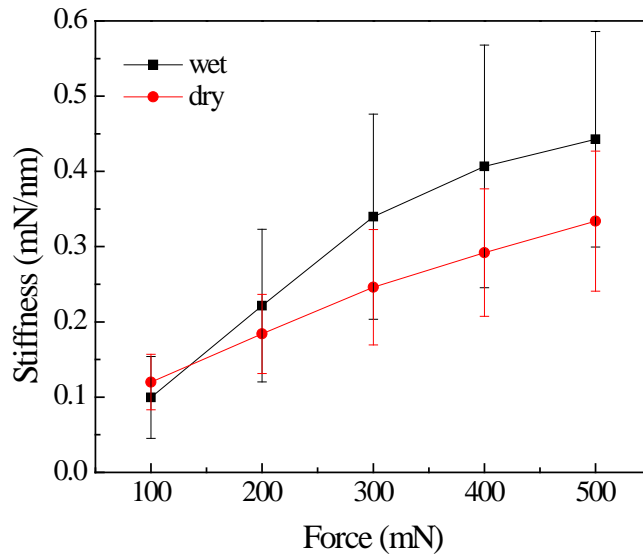
FIGURE 4.6 VARIATION OF THE STIFFNESS WITH MAXIMUM COMPRESSION LOAD FOR BOTH DRY AND WET DISKS

87

4.4   Discussion

It is known that stiffness is proportional to elastic modulus of materials, and the elastic modulus of porous materials is a function of the volume fraction of pores. For the compressed disks, we can approximate them as porous materials with different porosities. Note that there are various models for the calculation of the elastic modulus of porous materials. For detailed information, see the book by Gibson and Ashby [143].

Here, we assume the compressed disks as isotropic material (the matrix) consisting of n spherical voids under the action of external shear stress of τ_0. In general, the stress in a porous material is a function of spatial position as $\tau_0 + \Delta\tau$. Here, $\Delta\tau$ represents the stress variation induced by the pores. Using the principle of Eshelby's equivalent inclusion [144], we obtain

$$\tau_0 + \Delta\tau = \mu_0(\gamma_0 + \Delta\gamma - \gamma^*) = 0 \tag{4.2}$$

on the surface of the pores. Here, $\gamma = 2S_{33}\gamma^*$, $\tau_0 = 2\mu_0\gamma_0$, and $S_{33} = (4-5v_0)/15(1-v_0)$ which is the Eshelby parameter. μ_0 and v_0 are the shear modulus and Poisson's ratio of the matrix. Using Tanaka-Mori's theorem [145], we have

$$\int_{\Omega-V} \tau d\Omega = \int_{\Omega} \tau d\Omega = 0 \tag{4.3}$$

with Ω being the total volume of the porous material (consisting matrix and pores), and V being the volume occupied by pores. Substituting Eq. (4.2) into (4.3) yields

$$\int_{\Omega} \tau d\Omega = \frac{(2S_{33}-1)\phi\tau_0}{1-2S_{33}} \neq 0 \tag{4.4}$$

where ϕ is porosity. Equation (4.4) is in contradictory to the requirement of (4.3), suggesting that there exist a uniform shear stress of τ^* as

$$\tau^* = -\frac{(2S_{33}-1)\phi\tau_0}{1-2S_{33}}$$ (4.5)

applied to the porous material. Such a stress introduces a uniform shear strain to the shear strain of $\gamma_0 + \Delta\gamma$. The average strain under the action of $\tau_0 + \Delta\tau$ is

$$< \gamma_0 + \Delta\gamma > = \int_\Omega (\gamma_0 + \Delta\gamma) d\Omega$$ (4.6)

Using the definition of shear modulus and Eqs. (4.5) and (4.4), we obtain

$$\mu = \mu_0 \left(1 + \frac{15(1-v_0)}{7-v_0}\phi\right)^{-1}$$ (4.7)

which shows that decreasing the porosity increases the shear modulus. It is known that shear modulus is proportional to Young's modulus, which is proportional to stiffness. Thus, the elastic modulus of a compressed disk increases with the increase of the degree of consolidation, in accord with the trend shown in Fig. 4.6.

4.5 Conclusion

In this chapter, I have studied the effect of compression on the stiffness of compressed AC disks. Using the as-prepared HFCS-based ACs (AC-4), I have conducted the compression tests of AC disks, and obtained the compressive load-displacement curves of the compressed AC disk (mixed with 5 wt.% PTFE) in both dry and wet conditions. The results show that there is a linear region at the beginning of the loading

segment for both dry and wet disks, and the compression of the wet disks has a smaller linear region than that of the dry disks. The stiffness of the disks, S, which is proportional to the elastic modulus, is calculated from the slope at the onset of unloading curve. An increase of stiffness with the increase of the maximum compression load is found in both dry and wet disks, suggesting a consolidation effect. Increasing the maximum compression load would fortify the consolidation, leading to the increase of packing density and the elastic modulus of the disks. A simple model of porous materials is used to explain the increase in the stiffness of a compressed disk with the increase of the degree of consolidation. The comparison of the stiffness for both dry and wet disks reveals that the wet disks have a higher stiffness than that of the dry disks at the same maximum load, suggesting an effect of water on consolidation behavior, e.g. the motion and rotation of carbon particles in water would affect the consolidation degree.

CHAPTER 5.   EFFECT OF COMPRESSION ON EIS OF HTC-BASED ACS

5.1   Introduction

EDLC, as a new and economical type of ESDs in the 21st century, has drawn numerous attention on improving its power density and energy density. Multiple studies on the preparation and development of electrode materials and electrolytes have been done to enhance the performance of EDLCs. However, there are few studies focusing on the deformation effect on the performance of EDLCs. EDLCs store charge via the adsorption of electrolyte ions on the electrode-electrolyte interface, which is a combination of counter-ion adsorption and a co-ion expulsion[146]. Thus, the surface area and porous structure like pore-to-ion size and pore length are important parameters determining the charge storage in EDLCs.

In general, there are no remarkable volumetric changes caused by the charge storage in EDLCs. There do exist volumetric changes called charge-induced deformation due to the change in interface surface energy [147]. Structural degradation can occur especially under the action of a large current density, leading to the failure of EDLCs [148]. The relationship between the mechanical deformation and the electrochemical behavior of the electrode of EDLCs has a great research potentiality and has gradually attracted research interest. The mechanical pressure can greatly change the resistance of EDLCs by reducing the thickness of the diffusion layer and thus possibly increase the capacity [149].

It has been reported that introducing force into EDLCs' assembly can help to minimize the gap between the electrodes and maximize the contact with the separator, thus enhance the performance of EDLCs, but the limits of the applied force still need further studies [150].

In this chapter, the EIS of HFCS-based ACs was analyzed under the action of compression. EIS is an effective way to obtain the charge transfer resistance and equivalent resistance of EDLCs. It can also reflect the frequency-related behavior of EDLCs. The results show that increasing compression force can reduce resistance and enhance the capacitive performance of EDLCs.

5.2   Experimental details

5.2.1   Electrode preparation

The electrode preparation was the same as that discussed in Chapter 4.2. Briefly, the mixture of 95 wt.% HFCS-based activated carbon of AC-4 and pre-ground 5 wt.% PTFE after grinding in an agate mortar for an hour was mounted in a stainless steel cylinder mounting mold and was compressed under 0.2 metric ton for 60 s to make an electrode disks of ~8 mm in diameter, i.e. a pressure of 400 kg/cm^2. It is known that the capacitance of EDLCs is proportional to the active surface of porous materials, and negatively correlated to the effective thickness. Thus, increasing the fraction of a thick layer will not increase specific gravimetric capacitance. Compared with the common

parameters, the circular electrodes of 100~150 μm in thickness were prepared with an area density of 5 mg/cm^2.

Figure 5.1 shows schematic of the EDLC cell for the EIS measurement under compression. A separator of 696 glass microfiber filter (VWR International, LLC.) was placed between two electrode disks. A stainless steel was used as the current collector, whose end was connected with a potentiostat. 6 M KOH solution was used as the electrolyte. The EIS (Electrochemical Impedance Spectroscopy) analysis of the material were performed in a frequency of 0.02 Hz – 1 MHz on a Princeton Applied Research PARSTAT MC potentiostat (AMETEK, Inc., PA) with a sinusoid alternative voltage of 10 mV.

All experiments were done at room temperature.
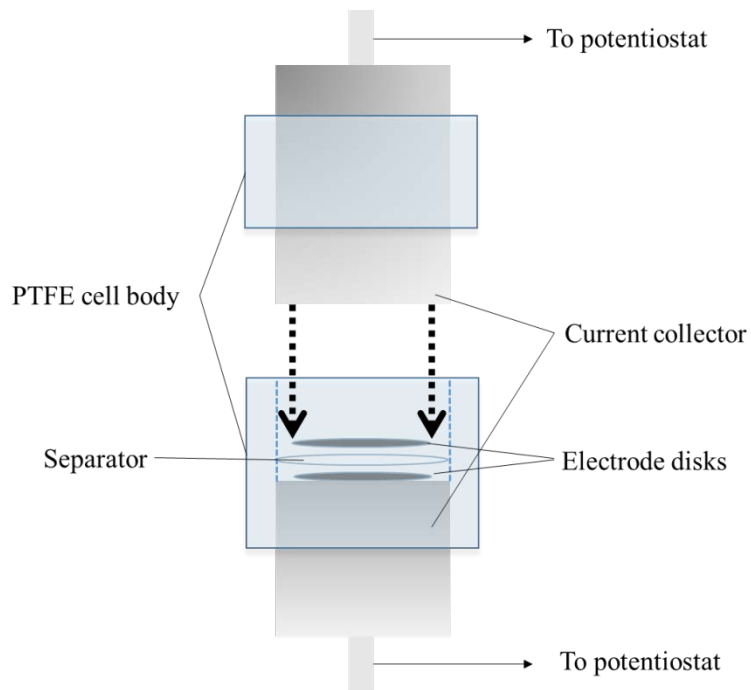
FIGURE 5.1 SCHEMATIC OF THE EDLC CELL FOR EIS MEASUREMENT UNDER COMPRESSION

5.2.2 EIS measurement

The electrochemical impedance of EDLCs was measured by applying a low-amplitude sin-wave alternative voltage ΔV to a steady-state potential V_s as

$$\Delta V(\omega) = \Delta V_{max} e^{j\omega t} \tag{5.1}$$

where ω is the angular frequency ($\omega = 2\pi f$), and ΔV_{max} is the amplitude. The output current is a sine-wave function with the same ω as the applied voltage and a phase shift φ as

$$\Delta I(\omega) = \Delta I_{max} e^{j(\omega t + \varphi)} \tag{5.2}$$

The electrochemical impedance $Z(\omega)$ is calculated as

$$\Delta Z(\omega) = \frac{\Delta V(\omega)}{\Delta I(\omega)} = |\Delta Z(\omega)| e^{-j\varphi} \tag{5.3}$$

which consists of the real part Z' and the imaginary part Z" as

$$Z(\omega) = Z'(\omega) + jZ''(\omega) \text{ and } Z'^2 + Z''^2 = |Z(\omega)|^2 \tag{5.4}$$

Define $C(\omega)(= C'(\omega) + i C''(\omega))$ as the capacity of the supercapacitor. There is

$$Z(\omega) = \frac{1}{j\omega \times C(\omega)} \tag{5.5}$$

From Eqs. 5.4 and 5.5, we obtain

$$C(\omega) = \frac{1}{\omega \times (jZ'(\omega) - Z''(\omega))} = \frac{-(Z''(\omega) + jZ'(\omega))}{\omega |Z(\omega)|^2} \tag{5.6}$$

which gives $C'(\omega)$ and $C''(\omega)$ as

$$C'(\omega) = \frac{-Z''(\omega)}{\omega |Z(\omega)|^2} \tag{5.7}$$

$$C''(\omega) = \frac{Z'(\omega)}{\omega |Z(\omega)|^2} \tag{5.8}$$

From Eqs.5.7 and 5.8, it can be seen that when ω is close to zero, i.e. at a very low frequency, the value of $C''(\omega)$ is also close to zero, so $C(\omega) = C'(\omega)_{low-frequency}$, which is the static capacitance of the cell measured in direct current measurement like CV and GC. When the frequency reaches $-\frac{\pi}{4}$, $C'(\omega) = \frac{1}{2}C'(\omega)_{low-frequency}$, and $C''(\omega)$ reaches its peak value. This peak frequency is defined as the characteristic frequency f_0, and the corresponded time is defined as the characteristic relaxation time τ_0, where $\tau_0 = \frac{1}{f_0}$. Since τ_0 is a reference value corresponding to the half of the $C'(\omega)_{low-frequency}$, it has been used to measure the performance of EDLCs. The smaller of the value of τ_0, the faster is the EDLC' charging and discharging rate [151].

5.3 Results and discussion

5.3.1 EIS equivalent circuit model and Nyquist Plots

EIS analysis was carried out in a frequency range of 0.02 Hz to 1MHz. The Nyquist plots of the disks under different compression pressures are shown in Figure 5.2, where the X-axis shows the value of the real part of impedance (Z′) and the Y-axis shows the negative value of the imaginary part of the impedance (Z″). There are many EIS models for supercapacitors, and each model is consisted with some electric equivalent elements like resistor (R), capacitor (C), constant phase element (Q) and Warburg element (W). The imaginary part of resistor'(R's) impedance is zero, so it's plotted as a dot in the X axis on the Nyquist diagram, the constant value in Z' is the value of resistor's impedance.

95

The capacitor (C) impedance is frequency-dependent, which would decrease with the increasing frequency. Its Nyquist diagram is a vertical straight line parallel to the Y axis. The constant phase element (CPE) is also a frequency-dependent element, which will also decrease with the increasing frequency; its Nyquist diagram is a straight line in the first quadrant with the positive imaginary value (-Z″>0) and a $-\dfrac{\alpha\pi}{2}$ angle with the X axis. The Warburg element (W) is used for the simulation of a semi-infinite diffusion, including the redox ion diffusion in batteries and pseudo capacitors and also a counter-ion and co-ion diffusion in EDLCs. It's a constant phase element that always has a constant angle of $-\dfrac{\pi}{4}$ with the X axis, which means the value of Z′ and -Z″ are equal at all frequencies [152].

One of the basic model for EDLCs is a resistance-capacitance RC-transmission line circuit, which consists of a resistance (R_1) and a capacitor (C) in series and parallel with another resistance (R_2). which can be generally simplified as a pure resistance at high frequencies (HF) and a RC in series at low frequencies (LF). In this case, the impedance in high frequency is a semi-circle where the first intercept on the real axis represents the value of R_1 and the other intercept represents (R_1+R_2), i.e. the diameter of the circle equals the value of R_2. Recalling the results from Eqs.5.7 and 5.8 that when ω reaches -$\dfrac{\pi}{4}$, the reciprocal of the corresponding frequency is the characteristic relaxation time τ_0, so in this case, τ_0 is the corresponding τ at the peak of the semi-circle. Since $RC = \dfrac{U}{I} \times \dfrac{Q}{U} = \dfrac{U}{I} \times \dfrac{It}{U} = \tau$, this is the method to calculate the C from R_2 and τ. However, instead of an expected semicircle with the center on the real axis of the Nyquist

diagram, it is more like an arc of a circle with a depressed semicircle for real-world

supercapacitors. The most common explanation for this phenomena is the inhomogeneity

or the distribution of some physical properties in the charging and discharging system

[153]. This could be simulated by a QR parallel model, and the C could be obtained via

the low frequency capacity $C'(\omega)_{low-frequency}$.

For EDLCs, one of the most important part is the electrolyte ion transfer (or ion

diffusion). In an EIS equivalent circuit model, this transfer is described by Warburg

element (W), which is a straight line with an angle of $-\frac{\pi}{4}$ with the X axis in the middle

frequency range of Nyquist plot. At high frequencies, electrolyte ions can hardly transfer

into the porous electrode materials in such a short time, the effect of W could be ignored,

so the existence of W is more like a transition region that shifting the capacitive behavior

at LF toward a resistive behavior at HF. The size of the shifting region indicates the

diffusion rate of the electrolyte ions, where the electrode porosity, electrode

pore/electrolyte ion ratio and the diffusion layer thickness are taking effects. The smaller

the shifting region, the faster is the diffusion rate of the electrolyte ions.

An EIS model consisting of R, C and W for EDLCs is shown in Figure 5.2a, and a

corresponding Nyquist diagram is plotted in Figure 5.2b. Here, R_s is the system resistance

of the bulk electrode and solution, R_{ct} is the charge transfer resistance affected by the

diffusion at the electrode/electrolyte interface, C_{dl} represents the double layer capacitance

of EDLCs, and W is the Warburg impedance resulted from the electrolyte ions diffusion.

It's worth mentioning that the EIS equivalent circuit model is a simplification of the real

circuit, for any real circuit, there could be more than one EIS equivalent circuit model that fit well with the EIS results. So the equivalent circuit model analysis is a relatively subjective method that doesn't possess uniqueness.

(a)   (b)
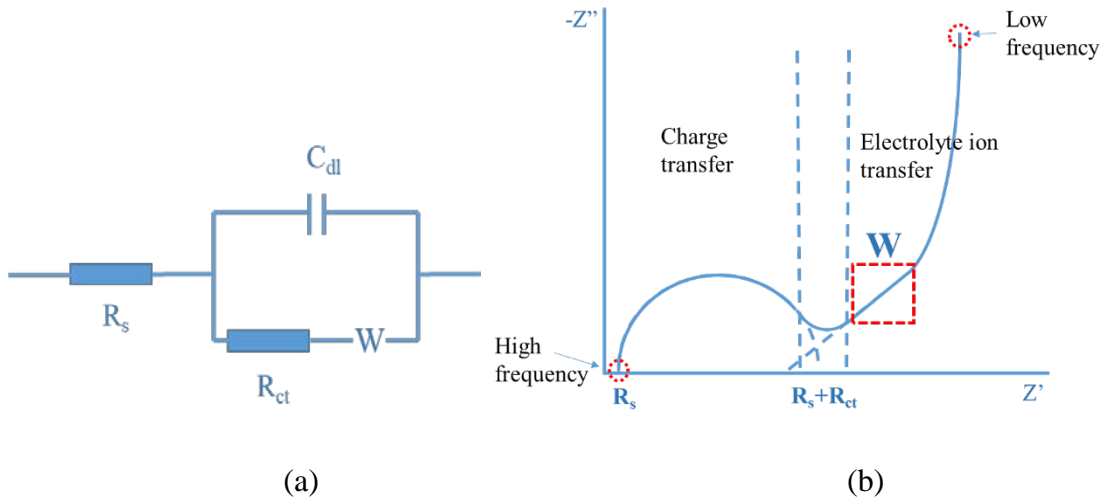
FIGURE 5.2 (A) SCHEMATIC OF A EDLCS' EQUIVALENT CIRCUIT, AND (B) THE CORRESPONDING NYQUIST PLOT

5.3.2   Results and discussion

The Nyquist plots of disks under different mechanical pressure are shown in Figure 5.3a, while Figure 5.3b is the enlarged view of the Nyquist plot in the high frequency region for disks compressed under pressures equal to and higher than 21.5 KPa. From the Nyquist plots, we can obtain Rs and Rct, which are shown in Figure 5.4 and Figure 5.5 respectively.
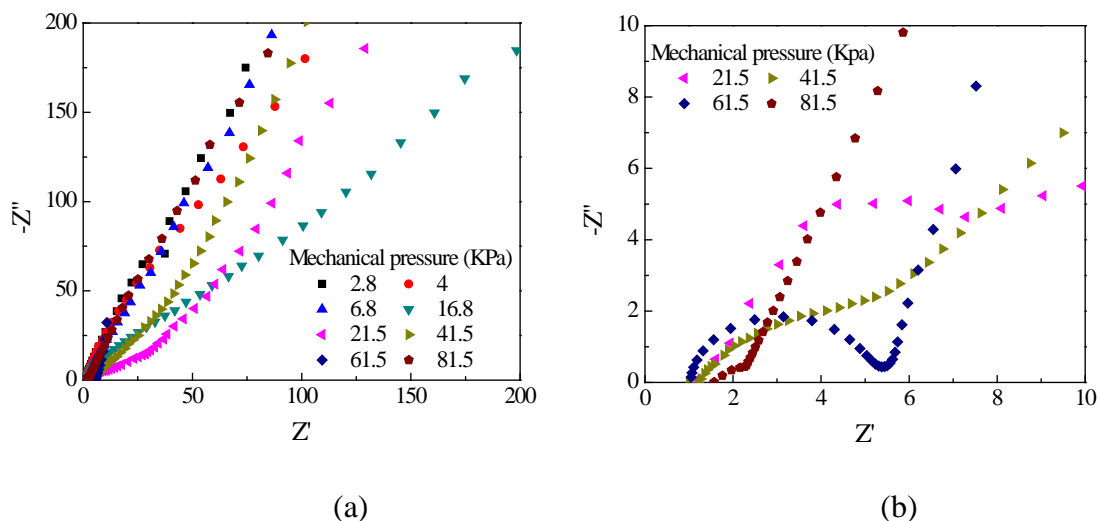
FIGURE 5.3 (A) NYQUIST PLOTS OF DISKS UNDER DIFFERENT MECHANICAL PRESSURES (KPA), (B) ENLARGED VIEW OF NYQUIST PLOTS OF DISKS IN HIGH FREQUENCY REGION UNDER MECHANICAL PRESSURE LARGER THAN 21.5 KPA.

For disks compressed under low pressure less than 6.8 KPa, the diameter of the semi-circle is very large, which is around 400 Ohms. No capacitive properties are observed, indicating that a low pressure would cause a bad assembly of the EDLCs. When increasing the pressure to 16.8 KPa, the diameter decreased to around 200 Ohms, but the shifting region in medium frequency is still very large. Continually increasing the pressure to 21.5 KPa and higher, relatively intact semi-circles are observed as shown in Figure 5.3b. With the increase of the compressive pressure, the diameter of the semi-circles is largely decreased, while the shifting region is also getting much smaller. Along the real axis (X axis) from the medium frequency region to the low frequency region, the Nyquist plot is transferring from an 45° line to a line with a sharply increased angle, indicating the capacitive properties. However, unlike the vertical line for C in the Nyquist plot, the real-world EDLCs are more like a line with the inclined angle between

45° and 90° between Warburg diffusion and ideal capacitive ion diffusion. This may be caused by the different penetration depth of the alternating current signal in virtue of pore size distribution at both electrodes.

Equation	y = a + b*x		
Adj. R-Square	0.12108		
		Value	Standard Error
Rs	Intercept	0.94468	0.19104
Rs	Slope	0.00665	0.00475
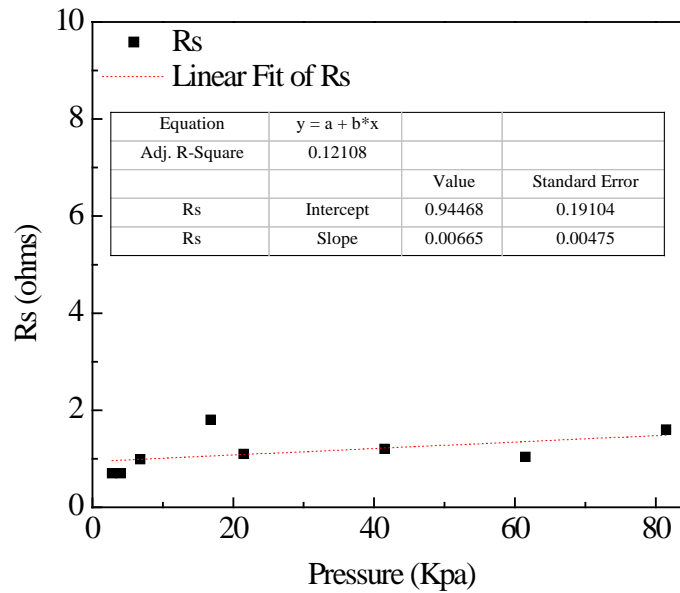
FIGURE 5.4 VARIATION OF R_S WITH THE MECHANICAL PRESSURE

Figure 5.4 shows the variation of R_s with mechanical pressure, where the value is obtained from the intercept of the semi-circle with the real axis at high frequency. The R_s is in a reasonable steady change, with the maximum value of 1.8 Ohms and the minimum value of 0.7 Ohms. The small slope of the linear fitting line further proves the little change of R_s under different mechanical pressure. R_s is the system resistance from the intrinsic resistance of electrode materials, electrolyte solutions, current collector and line connection, so it is generally considered to be constant for a specific system.

R_{ct} is the charge transfer resistance affected by the diffusion at the electrode/electrolyte interface, reflecting interfacial resistance. Generally, R_{ct} has larger value than R_s, since the charging and discharging process is controlled by ionic diffusion with R_{ct} being dominate over R_s. Acceding to the Stern model shown in Chapter 1, there are two layers near the electrode and electrolyte interface (Figure 1.2). One is the inner Helmholtz plane (IHP), which is a compact layer of mono-solvated electrolyte ions on the surface of electrode materials. The other is the outer Helmholtz plane (OHP), which is the diffusion layer next to the compact layer. The capacitance of an EDLC (C_{dl}) is the total capacitance of these two regions' capacitances in series, i.e. C_{dl} is decided by the smaller capacitance between these two. Usually, the diffusion layer owns a smaller capacity and a larger resistance than that of mono compacting layer due to its thicker layer [154]. So the properties of the diffusion layer, such as capacity and resistance, are playing dominant roles in determining the properties of the EDLCs.

Figure 5.5 shows the variation trend of R_{ct} under different mechanical pressures, where the value of R_{ct} is obtained from the diameter of the semi-circle in Nyquist plot. With the increase of the compressed pressure, R_{ct} shows a great decrease from 420 Ohms (2.8 KPa) to 1.5 Ohms (81.5 KPa), indicating the dramatic effect of mechanical pressure on reducing the resistance. One possible explanation for this phenomenon is that the increase of compressive pressure decreases the thickness of the diffusion layer, thus the R_{ct} accordingly. More factors may need to be taken into consideration when the diffusion layer is compressed into a very thin layer that close to an ideal zero, for example, the

contacting area, the effective ion concentration, and the porosity of the electrode materials. Further compression might firstly increase the contacting interface area and facilitate ionic diffusion which leads to a decrease of R_{ct}. However, further increasing compression pressure would cause a leakage of electrolyte, reduce the effective ion concentration, and destroy the intrinsic structure of the electrode materials, which leads to a negative impact to the EDLCs. This work needs further study to find the threshold value of the pressure.
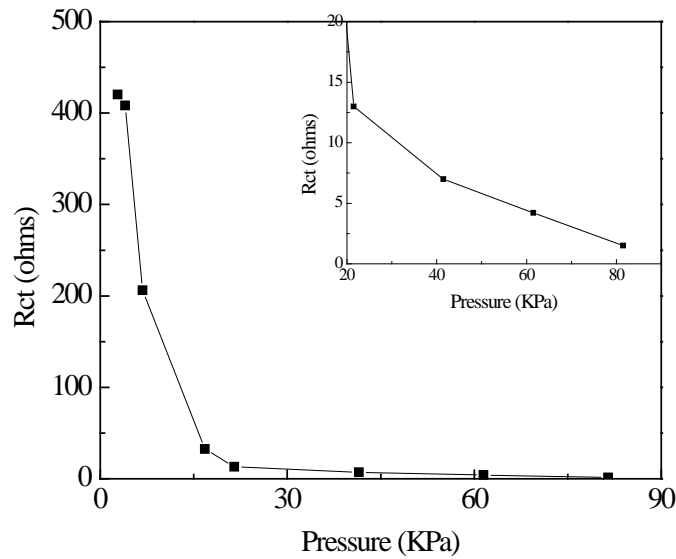
FIGURE 5.5 VARIATION OF R_{CT} WITH THE MECHANICAL PRESSURE

Since the energy density and power density are both in inverse proportion to the value of resistance. Decreasing the resistance is also an effective method of improving the energy density and power density for EDLCs. Applying an external compressive pressure can largely reduce the charge transfer resistance, and increase the energy density and power density of EDLCs accordingly. However, further work is required to study the

relation between the threshold value of the applied pressure and the thickness of diffuse layer, and also the pressure effect on the structure of electrode and the electrode/electrolyte interface.

5.4   Conclusion

In this chapter, the effect of mechanical pressure on EIS was studied. The EIS equivalent circuit model was discussed to analyze the EIS results. A series of pressure from 4 KPa to 81.5 KPa was applied, and the measured EIS results show a relatively steady change of the system resistance (R_s) and a dramatic reduction of the charge transfer resistance (R_{ct}) from 420 Ohms to 1.5 Ohms. The importance and dominance of the R_{ct} over R_s was discussed. R_{ct} is strongly depended on the thickness of the diffusion layer and the contacting area of the interface, where a thicker diffusion layer or a smaller contacting area both leads to a large R_{ct}. According to the experimental results, increasing mechanical pressure is an effective method to reduce the charge transfer resistance of EDLCs, which can increase the energy density and the power density accordingly.

CHAPTER 6.   SUMMARY AND FUTURE WORK

6.1   Summary

In this thesis, the activated carbons were prepared from biomass in both "bottom-up" and "top-down" patterns. High fructose corn syrup (HFCS) and soybean residues were used as the precursors, respectively. Both of these precursors were treated via hydrothermal carbonization processing and further activated via a physical self-activation. The mechanical responses of the as-prepared ACs were investigated, and the effect of the compression pressure on the EIS was also explored.

In chapter 2 of this thesis, HFCS was used for the first time as the precursors of the electrode materials of EDLCs. A simple HTC-physical self-activated method was used to synthesize activated carbons of a spherical shape. The largest specific surface area of the obtained ACs is 1473 m^2/g. The average size of the prepared AC spheres is ~0.8 μm. Increasing the activation time, increases the surface area of micropores and the fraction of micropores of the pore size ~0.67 nm.

The supercapacitor cells of symmetrical type (two-electrodes) were prepared without any additives and binders by using the prepared AC spheres as electrode materials. The supercapacitor cells made from the AC spheres of AC-4 show an excellent electrochemical performance with a specific capacitance of 168 F/g at an electric current density of 0.2 A/g and an energy density of 4.2 W·h/kg at a power density of 1.5 kW/kg.

In Chapter 3, a two-step hydrothermal processing and physical activation method was developed to treat soybean residues. A HTC process with low-concentration KOH was added to further treat the soybean residues due to complicated composition of soybean residues. Hollow-spherical carbon spheres were formed. ACs were derived with the activation temperature larger than or equal to 550 ℃. The geometrical and porous characteristics of soybean residue-derived ACs reveal the importance of the activation temperature in controlling the evolution of porous structures. The symmetrical two-electrode supercapacitor cells made from the ACs exhibit relatively good capacitive behavior, especially the supercapacitor cells with the ACs of AC-850 possess a specific gravimetric capacitance of 227 F/g at the scan rate of 2 mV/s, an energy density of 56.6 W·h/kg at a power density of 7.9 kW/kg at an energy density of 4.6 kW/kg.

In Chapter 4, the compression tests of the as-prepared ACs were performed. A linear region at the beginning of the loading segment for both dry and wet disks was observed, and the compression of the wet disks has a smaller linear region than that of the dry disks. An increase of stiffness with the increase of the maximum compression load was found for both dry and wet disks, suggesting the consolidation effect. A simple model of porous materials was used to explain the increase in the stiffness of the compressed disks with the increase of the compression force. The wet disks have a higher stiffness than that of the dry disks at the same maximum load, suggesting an effect of water on consolidation behavior, e.g. the motion and rotation of carbon particles in water would affect the consolidation degree.

In Chapter 5, the effect of mechanical compression on EIS was investigated. There are a relatively steady change of the system resistance (R_s) and a dramatic reduction of the charge transfer resistance (R_{ct}) from 420 Ohms to 1.5 Ohms from increasing the pressure from 4 KPa to 81.5 KPa. The importance and dominance of the R_{ct} over R_s was discussed. Increasing mechanical pressure is an effective method to reduce the charge transfer resistance of EDLCs, and increase the energy density and the power density.

6.2   Future work

From the analysis and discussion of the finished work in Chapters 2~5, it can be concluded that biomass like high fructose corn syrup and soybean residue can be used as good carbon sources for EDLCs. Mechanical behavior is playing an important role in determining the electrochemical performance of the electrode materials of EDLCs. In this dissertation, the synthesis of biomass-derived activated carbon in both "bottom-up" and "top-down" patterns were investigated with hydrothermal carbonization process and activated by a physical self-activation. HFCS was investigated for the first time as the precursor for electrode materials of EDLCs, and a physical self-activation method was used for the activation of hydrochar without any additive agent. In the future work, the focus of tuning the particle size, SSA, pore size and pore size distribution via controllable HTC process and self-activation method can provide a direction for efficient utilization of

106

different biomass-derived activated carbon electrode materials of EDLCs in different electrolytes.

This dissertation points out that compression pressure is an effective method to reduce the charge transfer resistance and thus facilitate the performance of the EDLCs. The threshold value of the compression pressure that minimize the charge transfer resistance will be the one of the focus in the future work for improving the performance of EDLCs. The other future research emphasis is on the variation of the mechanical responses under the action of the electrochemical charging and discharging cycling, which is of significance for the study of mechanical-electrochemistry.

REFERENCES

1.   *International energy agency (IEA) Statistics web site*. Available from: https://www.iea.org/statistics/?country=WORLD&year=2015&category=Key%20indicators&indi cator=TPESbySource&mode=chart&categoryBrowse=false.

2.   Shafiee, S. and E. Topal, *When will fossil fuel reserves be diminished?* Energy Policy, 2009. **37**(1): p. 181-189.

3.   Dias, R.A., C.R. Mattos, and J.A. P. Balestieri, *The limits of human development and the use of energy and natural resources.* Energy Policy, 2006. **34**(9): p. 1026-1031.

4.   Keyhani, A., *Smart Power Grids 2011*. 1st ed.. ed, ed. A. Keyhani and M. Marwali. 2012: Berlin, Heidelberg : Springer Berlin Heidelberg : Imprint: Springer.

5.   Simon, P. and Y. Gogotsi, *Materials for electrochemical capacitors.* Nature materials, 2008. **7**(11): p. 845-854.

6.   Kötz, R. and M. Carlen, *Principles and applications of electrochemical capacitors.* Electrochimica acta, 2000. **45**(15): p. 2483-2498.

7.   Helmholtz, H.v., *Ueber einige Gesetze der Vertheilung elektrischer Ströme in körperlichen Leitern mit Anwendung auf die thierisch-elektrischen Versuche.* Annalen der Physik, 1853. **165**(6): p. 211-233.

8.   Stern, O., *The theory of the electrolytic double-layer.* Z. Elektrochem, 1924. **30**(508): p. 1014-1020.

9.   Zhang, L.L. and X.S. Zhao, *Carbon-based materials as supercapacitor electrodes.* Chem Soc Rev, 2009. **38**(9): p. 2520-31.

10.   Zhang, H., X. Zhang, and Y. Ma, *Enhanced capacitance supercapacitor electrodes from porous carbons with high mesoporous volume.* Electrochimica Acta, 2015. **184**: p. 347-355.

11.   Raymundo-Pinero, E., et al., *Relationship between the nanoporous texture of activated carbons and their capacitance properties in different electrolytes.* Carbon, 2006. **44**(12): p. 2498-2507.

12.   Huang, J., B.G. Sumpter, and V. Meunier, *A universal model for nanoporous carbon supercapacitors applicable to diverse pore regimes, carbon materials, and electrolytes.* Chemistry, 2008. **14**(22): p. 6614-26.

13.   Wennerberg, A.N. and T.M. O'Grady, *Active carbon process and composition*. 1978, Google Patents.

14.   Marsh, H. and F.R. Reinoso, *Activated carbon*. 2006: Elsevier.

15.   Wang, J. and S. Kaskel, *KOH activation of carbon-based materials for energy storage.* Journal of Materials Chemistry, 2012. **22**(45): p. 23710.

16.   Ahmadpour, A. and D.D. Do, *The preparation of active carbons from coal by chemical and physical activation.* Carbon, 1996. **34**(4): p. 471-479.

17.   Lozano-Castelló, D., et al., *Carbon activation with KOH as explored by temperature programmed techniques, and the effects of hydrogen.* Carbon, 2007. **45**(13): p. 2529-2536.

18.   Świątkowski, A., *Industrial carbon adsorbents.* Studies in Surface Science and Catalysis, 1999. **120**(Part A): p. 69-94.

19.   Xiong, W., et al., *A novel synthesis of mesoporous carbon microspheres for supercapacitor electrodes.* Journal of Power Sources, 2011. **196**(23): p. 10461-10464.

20.   Dai, Y., et al., *Controlled Synthesis of Ultrathin Hollow Mesoporous Carbon Nanospheres for Supercapacitor Applications.* Industrial & Engineering Chemistry Research, 2014. **53**(8): p. 3125-3130.

21.   Chen, S.S., et al., *Thermal conductivity of isotopically modified graphene.* Nature Materials, 2012. **11**(3): p. 203-207.

22.   Lee, C., et al., *Measurement of the Elastic Properties and Intrinsic Strength of Monolayer Graphene.* Science, 2008. **321**(5887): p. 385-388.

23.   Stankovich, S., et al., *Graphene-based composite materials.* nature, 2006. **442**(7100): p. 282-286.

24.   Xia, J., et al., *Measurement of the quantum capacitance of graphene.* Nature nanotechnology, 2009. **4**(8): p. 505-509.

25.   Sun, Y., Q. Wu, and G. Shi, *Graphene based new energy materials.* Energy & Environmental Science, 2011. **4**(4): p. 1113-1132.

26.   Luo, B., S. Liu, and L. Zhi, *Chemical Approaches toward Graphene-Based Nanomaterials and their Applications in Energy-Related Areas.* Small, 2012. **8**(5): p. 630-646

27.   Li, X., et al., *Large-area synthesis of high-quality and uniform graphene films on copper foils.* Science, 2009. **324**(5932): p. 1312-1314

28.   Lee, J.-H., et al., *Wafer-scale growth of single-crystal monolayer graphene on reusable hydrogen-terminated germanium.* Science, 2014. **344**(6181): p. 286-289

29.   De Heer, W.A., et al., *Epitaxial graphene.* Solid State Communications, 2007. **143**(1): p. 92-100.

30.   Berger, C., et al., *Electronic confinement and coherence in patterned epitaxial graphene.* Science, 2006. **312**(5777): p. 1191-1196

31.   Deng, D., et al., *Freestanding graphene by thermal splitting of silicon carbide granules.* Advanced Materials, 2010. **22**(19): p. 2168-2171

32.   Wang, Y., et al., *Large area, continuous, few-layered graphene as anodes in organic photovoltaic devices.* Applied Physics Letters, 2009. **95**(6): p. 209.

33.   Li, D., et al., *Processable aqueous dispersions of graphene nanosheets.* Nature nanotechnology, 2008. **3**(2): p. 101-105

34.   Park, S., et al., *Colloidal suspensions of highly reduced graphene oxide in a wide variety of organic solvents.* Nano letters, 2009. **9**(4): p. 1593-1597

35.   Stoller, M.D., et al., *Graphene-based ultracapacitors.* Nano letters, 2008. **8**(10): p. 3498-3502

36.   Zhu, Y., et al., *Graphene and graphene oxide: synthesis, properties, and applications.* Advanced materials, 2010. **22**(35): p. 3906-3924

37.   Hernandez, Y., et al., *High-yield production of graphene by liquid-phase exfoliation of graphite.* Nature nanotechnology, 2008. **3**(9): p. 563-568.

38.   Bourlinos, A.B., et al., *Liquid-phase exfoliation of graphite towards solubilized graphenes.* small, 2009. **5**(16): p. 1841-1845.

39.   Li, X., et al., *Highly conducting graphene sheets and Langmuir–Blodgett films.* Nature nanotechnology, 2008. **3**(9): p. 538-542.

40.   Vallés, C., et al., *Solutions of negatively charged graphene sheets and ribbons.* Journal of the American Chemical Society, 2008. **130**(47): p. 15802-15804

41.   Tang, Y.B., et al., *High-quality graphenes via a facile quenching method for field-effect transistors.* Nano letters, 2009. **9**(4): p. 1374-1377.

42.   Feng, X., et al., *Supramolecular organization and photovoltaics of triangle -shaped discotic graphenes with swallow - tailed alkyl substituents.* Advanced Materials, 2008. **20**(14): p. 2684-2689

43.   Murugan, A.V., T. Muraliganth, and A. Manthiram, *Rapid, facile microwave-solvothermal synthesis of graphene nanosheets and their polyaniline nanocomposites for energy strorage.* Chemistry of Materials, 2009. **21**(21): p. 5004-5006.

44.   Chen, S., et al., *Synthesis and characterization of large-area graphene and graphite films on commercial Cu–Ni alloy foils.* Nano letters, 2011. **11**(9): p. 3519-3525

45.   Stankovich, S., et al., *Synthesis of graphene-based nanosheets via chemical reduction of exfoliated graphite oxide.* carbon, 2007. **45**(7): p. 1558-1565.

46.   Zhu, Y., et al., *Microwave assisted exfoliation and reduction of graphite oxide for ultracapacitors.* Carbon, 2010. **48**(7): p. 2118-2122

47.   Lv, W., et al., *Low-temperature exfoliated graphenes: vacuum-promoted exfoliation and electrochemical energy storage.* ACS nano, 2009. **3**(11): p. 3730-3736.

48.   Murugan, A.V., T. Muraliganth, and A. Manthiram, *Rapid, facile microwave-solvothermal synthesis of graphene nanosheets and their polyaniline nanocomposites for energy strorage.* Chemistry of Materials, 2009. **21**(21): p. 5004-5006

49.   Yan, J., et al., *Electrochemical properties of graphene nanosheet/carbon black composites as electrodes for supercapacitors.* Carbon, 2010. **48**(6): p. 1731-1737.

50.   Yu, D. and L. Dai, *Self-assembled graphene/carbon nanotube hybrid films for supercapacitors.* The Journal of Physical Chemistry Letters, 2009. **1**(2): p. 467-470

51.   Niu, J.J., et al., *An approach to carbon nanotubes with high surface area and large pore volume.* Microporous and Mesoporous Materials, 2007. **100**(1-3): p. 1-5.

52.   *Strength and toughness of fibre composites: by B. Harris, S. E. Dorey and R. G. Cooke, Composites Science and Technology , 31 (1988) 121–141.* 1988. p. 163-163.

53.   Futaba, D.N., et al., *Shape-engineerable and highly densely packed single-walled carbon nanotubes and their application as super-capacitor electrodes.* Nature materials, 2006. **5**(12): p. 987-994

54.   Niu, C., et al., *High power electrochemical capacitors based on carbon nanotube electrodes.* Applied Physics Letters, 1997. **70**(11): p. 1480-1482.

55.   Kim, B., H. Chung, and W. Kim, *Supergrowth of aligned carbon nanotubes directly on carbon papers and their properties as supercapacitors.* The Journal of Physical Chemistry C, 2010. **114**(35): p. 15223-15227.

56.   Zhao, X.S., et al., *Templating methods for preparation of porous structures.* Journal of Materials Chemistry, 2006. **16**(7): p. 637-648.

57.   Wang, J., et al., *Morphological effects on the electrical and electrochemical properties of carbon aerogels.* Journal of the Electrochemical Society, 2001. **148**(6): p. D75-D77.

58.   Portet, C., et al., *High power density electrodes for Carbon supercapacitor applications.* Electrochimica Acta, 2005. **50**(20): p. 4174-4181.

59.   Yang, X., et al., *Mesopore-dominant wormhole-like carbon with high supercapacitive performance in organic electrolyte.* RSC Adv., 2017. **7**(25): p. 15096-15101.

60.   Balducci, A., et al., *High temperature carbon–carbon supercapacitor using ionic liquid as electrolyte.* Journal of Power Sources, 2007. **165**(2): p. 922-927.

61.   Lewandowski, A., et al., *Performance of carbon–carbon supercapacitors based on organic, aqueous and ionic liquid electrolytes.* Journal of Power Sources, 2010. **195**(17): p. 5814-5819.

62.   Shim, Y. and H.J. Kim, *Nanoporous carbon supercapacitors in an ionic liquid: a computer simulation study.* ACS nano, 2010. **4**(4): p. 2345-2355.

63.   Dsoke, S., et al., *Strategies to reduce the resistance sources on Electrochemical Double Layer Capacitor electrodes.* Journal of Power Sources, 2013. **238**: p. 422-429.

64.   Vangari, M., T. Pryor, and L. Jiang, *Supercapacitors: Review of Materials and Fabrication Methods.* Journal of Energy Engineering, 2013. **139**(2): p. 72-79.

65.   Jiang, H., P.S. Lee, and C. Li, *3D carbon based nanostructures for advanced supercapacitors.* Energy Environ. Sci., 2013. **6**(1): p. 41-53.

66.   Zhang, H., et al., *Tube-covering-tube nanostructured polyaniline/carbon nanotube array composite electrode with high capacitance and superior rate performance as well as good cycling stability.* Electrochemistry Communications, 2008. **10**(7): p. 1056-1059.

67.   Benhaddad, L., et al., *Improvement of capacitive performances of symmetric carbon/carbon supercapacitors by addition of nanostructured polypyrrole powder.* Journal of Power Sources, 2016. **307**: p. 297-307.

68.   Jiang, H., et al., *Hierarchical self-assembly of ultrathin nickel hydroxide nanoflakes for high-performance supercapacitors.* Journal of Materials Chemistry, 2011. **21**(11): p. 3818.

69.   Lokhande, C.D., D.P. Dubal, and O.S. Joo, *Metal oxide thin film based supercapacitors.* Current Applied Physics, 2011. **11**(3): p. 255-270.

70.   Naoi, K. and P. Simon, *New materials and new configurations for advanced electrochemical capacitors.* Journal of The Electrochemical Society (JES), 2008. **17**(1): p. 34-37

71.   Yan, J., et al., *Advanced asymmetric supercapacitors based on Ni (OH)$_2$/graphene and porous graphene electrodes with high energy density.* Advanced Functional Materials, 2012. **22**(12): p. 2632-2641.

72.   Zhu, D., et al., *Nitrogen-containing carbon microspheres for supercapacitor electrodes.* Electrochimica Acta, 2015. **158**: p. 166-174.

73.   Cai, T., et al., *Highly ordered mesoporous phenol–formaldehyde carbon as supercapacitor electrode material.* Journal of Power Sources, 2013. **231**: p. 197-202.

74.   BIROL, F., *IEA World Energy Outlook 2006; International Energy Agency–Economic Analysis Division; París.* Francia, 2006: p. 37.

75.   Wei, L., et al., *Hydrothermal carbonization of abundant renewable natural organic chemicals for high-performance supercapacitor electrodes.* Advanced Energy Materials, 2011. **1**(3): p. 356-361.

76.   Li, X., et al., *Preparation and performance of straw based activated carbon for supercapacitor in non-aqueous electrolytes.* Microporous and Mesoporous Materials, 2010. **131**(1): p. 303-309

77.   Li, X., et al., *Preparation of capacitor's electrode from sunflower seed shell.* Bioresource Technology, 2011. **102**(2): p. 1118-1123

78.   Subramanian, V., et al., *Supercapacitors from activated carbon derived from banana fibers.* The Journal of Physical Chemistry C, 2007. **111**(20): p. 7527-7531.

79.   Kalpana, D., et al., *Recycled waste paper—A new source of raw material for electric double-layer capacitors.* Journal of Power Sources, 2009. **190**(2): p. 587-591.

80.   Huang, W., et al., *Hierarchical porous carbon obtained from animal bone and evaluation in electric double-layer capacitors.* Carbon, 2011. **49**(3): p. 838-843.

81.   Chen, W., et al., *A fish scale based hierarchical lamellar porous carbon material obtained using a natural template for high performance electrochemical capacitors.* Journal of Materials Chemistry, 2010. **20**(23): p. 4773-4775.

82.   Olivares-Marín, M., et al., *Cherry stones as precursor of activated carbons for supercapacitors.* Materials Chemistry and Physics, 2009. **114**(1): p. 323-327

83.   Wang, J. and S. Kaskel, *KOH activation of carbon-based materials for energy storage.* Journal of Materials Chemistry, 2012. **22**(45).

84.   Olivares-Marín, M., et al., *Cherry stones as precursor of activated carbons for supercapacitors.* Materials Chemistry and Physics, 2009. **114**(1): p. 323-327.

85.   Wang, H., et al., *Interconnected carbon nanosheets derived from hemp for ultrafast supercapacitors with high energy.* ACS nano, 2013. **7**(6): p. 5131-5141.

86.   Sun, W., et al., *Hemp-derived activated carbons for supercapacitors.* Carbon, 2016. **103**: p. 181-192.

87.   Kishore, B., et al., *Coconut kernel-derived activated carbon as electrode material for electrical double-layer capacitors.* Journal of Applied Electrochemistry, 2014. **44**(8): p. 903-916.

88.   Wu, F.-C., et al., *Effects of pore structure and electrolyte on the capacitive characteristics of steam- and KOH-activated carbons for supercapacitors.* Journal of Power Sources, 2005. **144**(1): p. 302-309.

89.   Qu, W.-H., et al., *Converting biowaste corncob residue into high value added porous carbon for supercapacitor electrodes.* Bioresource technology, 2015. **189**: p. 285-291.

90.   Nabais, J.M., J.G. Teixeira, and I. Almeida, *Development of easy made low cost bindless monolithic electrodes from biomass with controlled properties to be used as electrochemical capacitors.* Bioresour Technol, 2011. **102**(3): p. 2781-7.

91.   Ro, K.S., K.B. Cantrell, and P.G. Hunt, *High-temperature pyrolysis of blended animal manures for producing renewable energy and value-added biochar.* Industrial & Engineering Chemistry Research, 2010. **49**(20): p. 10125-10131

92.   Lehmann, J., *A handful of carbon.* Nature, 2007. **447**(7141): p. 143-144.

93.   Vaccari, F.P., et al., *Biochar as a strategy to sequester carbon and increase yield in durum wheat.* European Journal of Agronomy, 2011. **34**(4): p. 231-238

94.   Galinato, S.P., J.K. Yoder, and D. Granatstein, *The economic value of biochar in crop production and carbon sequestration.* Energy Policy, 2011. **39**(10): p. 6344-6350.

95.   Wang, L., et al., *High surface area porous carbons prepared from hydrochars by phosphoric acid activation.* Bioresource Technology, 2011. **102**(2): p. 1947-1950

96.   Chun, S.-E., Y.N. Picard, and J.F. Whitacre, *Relating precursor pyrolysis conditions and aqueous electrolyte capacitive energy storage properties for activated carbons derived from anhydrous glucose-d.* Journal of The Electrochemical Society, 2011. **158**(2): p. A83-A92.

97.   Wang, L., et al., *Preparation of carbon black from rice husk by hydrolysis, carbonization and pyrolysis.* Bioresource technology, 2011. **102**(17): p. 8220-8224

98.   Liu, Z. and F.-S. Zhang, *Removal of copper (II) and phenol from aqueous solution using porous carbons derived from hydrothermal chars.* Desalination, 2011. **267**(1): p. 101-106.

99.   Li, M., W. Li, and S. Liu, *Hydrothermal synthesis, characterization, and KOH activation of carbon spheres from glucose.* Carbohydrate research, 2011. **346**(8): p. 999-1004.

100.   Sevilla, M., J.A. Macia-Agullo, and A.B. Fuertes, *Hydrothermal carbonization of biomass as a route for the sequestration of CO$_2$: chemical and structural properties of the carbonized products.* Biomass and Bioenergy, 2011. **35**(7): p. 3152-3159.

101.   Mumme, J., et al., *Hydrothermal carbonization of anaerobically digested maize silage.* Bioresource Technology, 2011. **102**(19): p. 9255-9260.

102.   Hu, B., et al., *Engineering carbon materials from the hydrothermal carbonization process of biomass.* Advanced Materials, 2010. **22**(7): p. 813-828.

103.   Kang, S., et al., *Characterization of Hydrochars Produced by Hydrothermal Carbonization of Lignin, Cellulose,d-Xylose, and Wood Meal.* Industrial & Engineering Chemistry Research, 2012. **51**(26): p. 9023-9031.

104.   Wei, L., et al., *Hydrothermal Carbonization of Abundant Renewable Natural Organic Chemicals for High-Performance Supercapacitor Electrodes.* Advanced Energy Materials, 2011. **1**(3): p. 356-361.

105.   Zhao, L., et al., *Nitrogen-containing hydrothermal carbons with superior performance in supercapacitors.* Adv Mater, 2010. **22**(45): p. 5202-5206.

106.   Redondo, E., et al., *Effect of pore texture on performance of activated carbon supercapacitor electrodes derived from olive pits.* Electrochimica Acta, 2015. **160**: p. 178-184.

107.   Ramirez-Castro, C., et al., *Microporous carbonaceous materials prepared from biowaste for supercapacitor application.* Electrochimica Acta, 2016. **206**: p. 452-457.

108.   Gao, Z., et al., *Cotton-Textile-Enabled, Flexible Lithium-Ion Batteries with Enhanced Capacity and Extended Lifespan.* Nano Lett, 2015. **15**(12): p. 8194-203.

109.   Gao, Z., et al., *Towards flexible lithium-sulfur battery from natural cotton textile.* Electrochimica Acta, 2017. **246**: p. 507-516.

110.   Gao, Z., et al., *Biomass-derived renewable carbon materials for electrochemical energy storage.* Materials Research Letters, 2016. **5**(2): p. 69-88.

111.   White, J.S., *Straight talk about high-fructose corn syrup: what it is and what it ain't.* The American journal of clinical nutrition, 2008. **88**(6): p. 1716S-1721S.

112.   Lin, X.-X., et al., *Ionothermal synthesis of microporous and mesoporous carbon aerogels from fructose as electrode materials for supercapacitors.* Journal of Materials Chemistry A, 2016. **4**(12): p. 4497-4505.

113.   Esposito, D. and M. Antonietti, *Redefining biorefinery: the search for unconventional building blocks for materials.* Chem Soc Rev, 2015. **44**(16): p. 5821-35.

114.   Brunauer, S., P.H. Emmett, and E. Teller, *Adsorption of gases in multimolecular layers.* Journal of the American chemical society, 1938. **60**(2): p. 309-319.

115.   Evans, R., *The nature of the liquid-vapour interface and other topics in the statistical mechanics of non-uniform, classical fluids.* Advances in Physics, 1979. **28**(2): p. 143-200.

116.   Seaton, N.A. and J. Walton, *A new analysis method for the determination of the pore size distribution of porous carbons from nitrogen adsorption measurements.* Carbon, 1989. **27**(6): p. 853-861.

117.   Yang, X., et al., *Mesopore-dominant wormhole-like carbon with high supercapacitive performance in organic electrolyte.* RSC Advances, 2017. **7**(25): p. 15096-15101.

118.   Lei, C., et al., *Reduction of porous carbon/Al contact resistance for an electric double-layer capacitor (EDLC).* Electrochimica Acta, 2013. **92**: p. 183-187.

119.   Conway, B.E., *Electrochemical supercapacitors: scientific fundamentals and technological applications.* 2013: Springer Science & Business Media.

120.   Taberna, P., P. Simon, and J.-F. Fauvarque, *Electrochemical characteristics and impedance spectroscopy studies of carbon-carbon supercapacitors.* Journal of The Electrochemical Society, 2003. **150**(3): p. A292-A300.

121.   Anothumakkool, B., et al., *1-Dimensional confinement of porous polyethylenedioxythiophene using carbon nanofibers as a solid template: an efficient charge storage material with improved capacitance retention and cycle stability.* RSC Advances, 2013. **3**(29): p. 11877-11887.

122.   Chmiola, J., et al., *Effect of pore size and surface area of carbide derived carbons on specific capacitance.* Journal of Power Sources, 2006. **158**(1): p. 765-772.

123.   Li, S., et al., *Soybean Curd Residue: Composition, Utilization, and Related Limiting Factors.* ISRN Industrial Engineering, 2013. **2013**: p. 1-8.

124.   Muroyama, K., T. Mochizuki, and T. Wakamura, *Methane fermentation of bean curd refuse.* Journal of bioscience and bioengineering, 2001. **91**(2): p. 208-212.

125.   Rashad, M.M., et al., *Improvement of nutritional quality and antioxidant activities of yeast fermented soybean curd residue.* African Journal of Biotechnology, 2011. **10**(28): p. 5504-5513.

126.   Turhan, S., H. Temiz, and I. Sagir, *UTILIZATION OF WET OKARA IN LOW-FAT BEEF PATTIES.* Journal of Muscle Foods, 2007. **18**(2): p. 226-235.

127.   Ferrero, G.A., A.B. Fuertes, and M. Sevilla, *From Soybean residue to advanced supercapacitors.* Sci Rep, 2015. **5**: p. 16618.

128.   Guo, N., et al., *Soybean Root-Derived Hierarchical Porous Carbon as Electrode Material for High-Performance Supercapacitors in Ionic Liquids.* ACS Appl Mater Interfaces, 2016. **8**(49): p. 33626-33634.

129.   Ma, G., et al., *Nitrogen-doped Porous Carbon Obtained via One-step Carbonizing Biowaste Soybean Curd Residue for Supercapacitor Application.* Rsc Advances, 2015. **5**(101): p. 83129-83138.

130.   Xu, M., et al., *Simultaneously obtaining fluorescent carbon dots and porous active carbon for supercapacitors from biomass.* RSC Advances, 2016. **6**(91): p. 88674-88682.

131.   Harmer, M.A., et al., *A new route to high yield sugars from biomass: phosphoric-sulfuric acid.* Chem Commun (Camb), 2009(43): p. 6610-2.

132.   Chmiola, J., et al., *Anomalous increase in carbon capacitance at pore sizes less than 1 nanometer.* Science (New York, N.Y.), 2006. **313**(5794): p. 1760.

133.   Eliad, L., et al., *Assessing optimal pore-to-ion size relations in the design of porous poly(vinylidene chloride) carbons for EDL capacitors.* Applied Physics A, 2005. **82**(4): p. 607-613.

134.   Barbieri, O., et al., *Capacitance limits of high surface area activated carbons for double layer capacitors.* Carbon, 2005. **43**(6): p. 1303-1310.

135.   Awitdrus, M., et al., *Effect of compression pressure on the physical and electrochemical properties of activated carbon monoliths electrodes for supercapacitor application.* 2012. p. 13-18.

136.   Shi, K., et al., *Efficient Lightweight Supercapacitor with Compression Stability.* Advanced Functional Materials, 2016. **26**(35): p. 6437-6445.

137.   Lv, P., et al., *Graphene/Polyaniline Aerogel with Superelasticity and High Capacitance as Highly Compression-Tolerant Supercapacitor Electrode.* Nanoscale Res Lett, 2017. **12**(1): p. 630.

138.   Zhao, Y., et al., *Highly compression-tolerant supercapacitor based on polypyrrole-mediated graphene foam electrodes.* Adv Mater, 2013. **25**(4): p. 591-5.

139.   Zhang, X., et al., *Mechanically robust and highly compressible electrochemical supercapacitors from nitrogen-doped carbon aerogels.* Carbon, 2018. **127**: p. 236-244.

140.   Lv, P., X. Tang, and W. Wei, *Graphene/MnO2 aerogel with both high compression-tolerance ability and high capacitance, for compressible all-solid-state supercapacitors.* RSC Adv., 2017. **7**(74): p. 47116-47124.

141.   Westover, A.S., et al., *A multifunctional load-bearing solid-state supercapacitor.* Nano Lett, 2014. **14**(6): p. 3197-202.

142.   Song, Y., et al., *Highly compression-tolerant folded carbon nanotube/paper as solid-state supercapacitor electrode.* Micro & Nano Letters, 2016. **11**(10): p. 586-590.

143.   Gibson, L.J. and M.F. Ashby, *Cellular solids: structure and properties.* 1999: Cambridge university press.

144.   Mura, T., *Micromechanics of defects in solids.* 2013: Springer Science & Business Media.

145.   Tanaka, K. and T. Mori, *The hardening of crystals by non-deforming particles and fibres.* Acta Metallurgica, 1970. **18**(8): p. 931-941.

146.   Prehal, C., et al., *Tracking the structural arrangement of ions in carbon supercapacitor nanopores using in situ small-angle X-ray scattering.* Energy & Environmental Science, 2015. **8**(6): p. 1725-1735.

147.   Yang, F., *Analysis of charging-induced structural damage in electrochemical systems.* Phys Chem Chem Phys, 2017. **19**(10): p. 7072-7077.

148.   *<Current-induced strength degradation of activated carbon spheres in.pdf>.*

149.   Li, K.-B., et al., *Studies on the equivalent serial resistance of carbon supercapacitor.* Electrochimica Acta, 2015. **174**: p. 596-600.

150.   Gourdin, G., et al., *Investigation of the impact of stacking pressure on a double-layer supercapacitor.* Journal of Power Sources, 2011. **196**(1): p. 523-529.

151.   *<Electrochemical Characteristics and Impedance Spectroscopy Studies of Carbon-Carbon Supercapacitors.pdf>.*

152.   *EC-lab   software   users   manual.* Available   from: https://www.egr.msu.edu/~scb-group-web/blog/wp-content/uploads/2012/07/EC-Lab-software-users-manual.pdf.

153.   Orazem, M.E., *Electrochemical impedance spectroscopy*, ed. B. Tribollet. 2008, Hoboken, N.J.: Hoboken, N.J. : Wiley.

154.   Kang, J., et al., *Characterization of thermal behaviors of electrochemical double layer capacitors (EDLCs) with aqueous and organic electrolytes.* Electrochimica Acta, 2014. **144**: p. 200-210.

VITA

Wenxin Cao was born in Chenzhou, Hunan, China. She attended Central South University (CSU) in Changsha, P. R. China, where she received her Bachelor degree of Engineering in School of Metallurgical Science and Engineering in July, 2012 and her Master degree of Engineering in Metallurgical Science and Engineering in July, 2015. After her graduation in China, she began her Ph.D. study in the Materials Science and Engineering program at the University of Kentucky in January, 2016.

Publications:

Wenxin Cao and Fuqian Yang, Supercapacitors from high fructose corn syrup-derived activated carbons, *Materials Today Energy (2018) 9*

Wenxin Cao, Wangang Zhang, Meiqing Guo and Fuqian Yang, Hollow activated carbons from soybean residue for electrical double layer capacitors, *Carbon (Submitted)*

Je-Chuan Hsu, **Wenxin Cao**, Fuqian Yang, and Sanboh Lee, Absorption behavior of poly(methyl methacrylate)-multiwalled carbon nanotubes composites: effects of UV irradiation and multiwalled carbon nanotubes, *Physical Chemistry Chemical Physics*, 19 (2017) 7359-7369

Han-Ren Hsu, **Wenxin Cao**, Fuqian Yang, and Sanboh Lee, Methanol-assisted crack healing in UV-irradiated poly(methyl methacrylate), *Journal of Polymer Research (Accepted)*

Yi-Wei Huang, Wen-Shin Lee, Yu-Fan Chuang, **Wenxin Cao**, Fuqian Yang, Sanboh Lee, Time-dependent deformation of artificial muscles based on nylon 6, *Materials and Science & Engineering C (Submitted)*

Chuanfu Zhang, **Wenxin Cao** and Jing Zhan, Extraction equilibrium of Mn, Ca and Mg from chloride solutions by di (2-ethylhexyl) phosphoric acid dissolved in kerosene, *The Member Journal of The Minerals, Metals &Materials Society,* 67(5) (2015), 1110-1113